Alma Mater Studiorum · Università di Bologna

Scuola di Scienze
Dipartimento di Fisica e Astronomia
Corso di Laurea Magistrale in Fisica

Search for scalar and vector doubly charged bosons with Run 2 data collected by the ATLAS experiment at LHC

Relatore:
Prof. Maximiliano Sioli

Presentata da:
Silvia De Luca

Correlatori:
Dott. Antonio Sidoti
Dott. Giuseppe Carratta

Sessione III
Anno Accademico 2019/2020

Contents

Sommario

Il lavoro riportato in questa tesi si svolge nell'ambito delle teorie oltre il Modello Standard e riguarda la ricerca di bosoni scalari e vettoriali doppiamente carichi predetti nel Bilepton Model e nel Left-Right Symmetric Model (LRSM). Lo studio impiega i dati delle collisioni protone-protone raccolti dal rivelatore ATLAS durante il Run 2 del Large Hadron Collider a un'energia del centro di massa di 13 TeV, corrispondente a 139 fb^{-1} di luminosità integrata. L'analisi condotta sfrutta il canale multileptonico $pp \to H^{\pm\pm}H^{\mp\mp}(\Delta^{\pm\pm}\Delta^{\mp\mp}, Y^{\pm\pm}Y^{\mp\mp}) \to \ell^{\pm}\ell^{\pm}\ell'^{\mp}\ell'^{\mp}$ caratterizzato da uno stato finale formato da leptoni leggeri ($\ell, \ell' = e, \mu$), di alta energia, isolati e prodotti direttamente dai bosoni provenienti dal vertice primario. Lo scopo è quello di estendere una precedente analisi includendo per la prima volta la presenza di bosoni vettoriali doppiamente carichi. Non osservando un eccesso rispetto alle predizioni del Modello Standard, è stato calcolato un limite di esclusione al 95% di CL per le masse dei bosoni interessati.

Abstract

The work presented in this thesis concerns the search for scalar and vector doubly charged bosons predicted by two theories Beyond the Standard Model: the Bilepton Model and the Left-Right Symmetric Model (LRSM). The search uses proton-proton collision data at centre-of-mass energy of 13 TeV, corresponding to 139 fb^{-1} of integrated luminosity collected by the ATLAS detector in the Run 2 of the Large Hadron Collider. The analysis focuses on the multi-leptonic channel $pp \to H^{\pm\pm}H^{\mp\mp}(\Delta^{\pm\pm}\Delta^{\mp\mp}, Y^{\pm\pm}Y^{\mp\mp}) \to \ell^{\pm}\ell^{\pm}\ell'^{\mp}\ell'^{\mp}$ characterized by a final state with prompt, isolated, highly energetic leptons in same-charge same-flavour pairs where $\ell, \ell' = e, \mu$. The aim is to discriminate the signals of the doubly charged vector $Y^{\pm\pm}$ and scalar $\Delta^{\pm\pm}$ bosons from the Dilepton model and the signal of the doubly charged Higgs boson $H^{\pm\pm}$ predicted by the LRSM, this latter is already part of a ongoing analysis in ATLAS. Since no significant excess over the Standard Model expectation is observed, an exclusion limit at 95% of CL for the bosons mass is performed.

Introduction

The Standard Model (SM) of particle physics, finalized in the 1970s after years marked by startling discoveries, managed to describe the behaviour of fundamental constituents of matter and their interactions thanks to an advanced and predictive theory. The SM predictions were proved right throughout the years establishing it as *the* theory of particle physics. The common believe is, in fact, that at worst the SM is an approximation at low energy of a more extended theory, but not wrong.
More recent experimental observations seem to give credit to this belief, paving the way for Beyond Standard Model (BSM) theories. Within this work two of these BSM theories are considered: the *Bilepton Model* and the *Left-Right Symmetric Model (LRSM)*. The former, also referred to as *331 Model*, shares with the latter the fact that both predict the existence of doubly charged bosons but with different phenomenology. The 331 Model is interesting since naturally accounts for the three fermion families experimentally observed. It is also the only SM extension that adds to the theory both a doubly charged scalar boson ($H^{\pm\pm}$) and a doubly charged *vector* boson ($Y^{\pm\pm}$) called *bileptons*. The decaying bileptons produce a signature (1) rarely seen according to the prediction of SM increasing interest toward it. The LRSM, on the other hand, enlarge the SM symmetry group to restore the parity symmetry in weak interactions at higher energy scales and, in addition, explain light neutrino masses through a seesaw mechanism. In this case the model introduces, among the other particles, a doubly charged Higgs boson both in left- and right-handed states $\Delta^{\pm\pm}_{L,R}$.
At the LHC hints for new physics predicted by these models are searched for in multi-leptonic channels like

$$pp \to Y^{++}Y^{--}\left(H^{++}H^{--}, \Delta^{++}\Delta^{--}\right) \to \ell^+\ell^+\ell'^-\ell'^- \tag{1}$$

where the final state consists of same-charge same-flavour leptons pairs since the flavour violation is not allowed within the Bilepton Model, excluding in this way most of the SM processes such as ZZ production, $t\bar{t}$ production or Higgs boson decay into a pair of Z bosons.
Both the ATLAS and CMS Collaborations [26, 27] are involved in the search for doubly charged Higgs bosons from the LRSM produced in multi-lepton final states. The study here proposed aims at searching for the first time scalar and vector doubly charged

bosons with Run 2 data at $\sqrt{s} = 13$ TeV collected by the ATLAS experiment. This work exploits the results of a previous master thesis [28], consisting in a study of the 331 model to evaluate the feasibility of a discriminant analysis at the reconstructed level using the ATLAS detector.
The Analysis here presented extend a previous ATLAS search of scalar LRSM doubly charged bosons with the inclusion - for the first time - of vectorial doubly charged bosons from the 331 model.

- **Chapter 1**: introductory discussion on the Standard Model comprehensive of an overview on physical foundations is provided. Here also the Bilepton Model and the Left-Right Symmetric Model are introduced.
- **Chapter 2**: introduction to the LHC collider and the ATLAS experiment, followed by a more detailed description of the ATLAS detector and its components.
- **Chapter 3**: description of how particles detected by ATLAS are reconstructed.
- **Chapter 4**: this chapter presents the analysis performed and the results obtained.

Chapter 1

The Standard Model of particle physics and beyond

Our ever growing understanding of the laws of nature finds in particle physics a fertile ground. The theories and discoveries since 1930s, which offered a remarkable insight into the fundamental structure of matter, have been implemented in the Standard Model (SM) of particle physics. Developed in the early 1970s, this theory proved to be a successful explanation of particle physics phenomena, confirmed also by precisely predicting a broad number of phenomena.
However, as one will point out later, the technological enhancement of experimental tools allowed to better constrain the SM predictions but also gave the chance to observe that some aspects of particle physics need a deeper understanding which could be found in Beyond the Standard Model (BSM) theories.

1.1 The Standard Model of particle physics

The theoretical framework of the Standard Model (SM) provides a powerful description of the fundamental forces through *Relativistic Quantum Field Theories* ($RQFT$) and local gauge invariance [1]. The electromagnetic, strong and weak interactions are described respectively by *Quantum ElectroDynamics* (QED), *Quantum ChromoDynamic* (QCD) and *Quantum FlavourDynamics* (QFD). At high energy electromagnetic and weak interactions are unified and described by the *Electroweak Theory* (EW). The SM is based on the following gauge symmetry group:

$$SU(3)_C \otimes SU(2)_L \otimes U(1)_Y \tag{1.1}$$

where $SU(3)_C$ is the gauge group for the strong interaction and $SU(2)_L \otimes U(1)_Y$ for the electroweak interaction.
The gravitational interaction is not included in the SM theory since its effect is so weak

(at a distance of 1 fm = 10^{-15} m its strength is $\sim 10^{-37}$ [2]) to be negligible compared to the intensity of other interactions between elementary particles. Only when matter is in bulk the effect of gravity dominates. In this way its exclusion does not affect the SM predictions.

1.1.1 Particles classification

The building blocks of the SM are the so called *elementary* or *fundamental particles* such as leptons and quarks. All particles carry several properties, such as mass, electric charge and *spin*, which represents a particle intrinsic angular momentum.

	Leptons			Quarks		
	Particle	Q	mass/GeV	Particle	Q	mass/GeV
I gen.	e^-	-1	0.0005	d	$-1/3$	0.003
	ν_e	0	$< 10^{-9}$	u	$+2/3$	0.005
II gen.	μ^-	-1	0.106	s	-1/3	0.1
	ν_μ	0	$< 10^{-9}$	c	$+2/3$	1.3
III gen.	τ^-	-1	1.78	b	-1/3	4.5
	ν_τ	0	$< 10^{-9}$	t	$+2/3$	174

Table 1.1: Table of Standard Model elementary particles [2].

Particles are divided into *fermions* and *bosons* according to their spin values: fermions are 1/2 spin particles obeying Fermi-Dirac statistics while bosons have integer spin and follow Bose-Einstein statistics. Fermions are further divided into three families of *leptons* and three families of *quarks*, Table 1.1 .
Leptons and quarks properties are described in terms of the following quantum numbers:

electric charge carried by all particles except neutrinos. Leptons have electric charge $Q = -1$. Quarks' charge is a fraction of the electron charge: *u, c* and *t* have $Q = +2/3$ while *d, s* and *b* have $Q = -1/3$. Hadrons always carry integer charge.

leptonic number associated to each lepton $L = +1$ and globally conserved by all interactions.

colour charge conventionally named: red, blue and green, is carried only by quarks. It is responsible for strong interaction and *confinement*, which makes impossible to observe free quarks. They strongly interact among themselves in order to constitute *hadrons*. Depending on the number of interacting quarks one has *barions* in the combination of three quarks qqq and *mesons* with two $q\bar{q}$ combined.

flavour number associated both to leptons and quarks. In the quark sector it is not conserved by weak interactions.

baryonic number $B = +1/3$ is associated to each quark.

Anti-fermions have opposite-sign quantum numbers with respect to fermions. As shown in Table 1.1, fermions are divided into three families each composed by two leptons

$$\begin{pmatrix} \nu_e \\ e \end{pmatrix}, \quad \begin{pmatrix} \nu_\mu \\ \mu \end{pmatrix}, \quad \begin{pmatrix} \nu_\tau \\ \tau \end{pmatrix} \tag{1.2}$$

and two quarks

$$\begin{pmatrix} u \\ d \end{pmatrix}, \quad \begin{pmatrix} c \\ s \end{pmatrix}, \quad \begin{pmatrix} t \\ b \end{pmatrix} \tag{1.3}$$

the total number of fundamental constituents consists of 12 fermions and 12 antifermions. Interaction between fermions are mediated through the exchange of gauge vector bosons, with *spin* 1:

- the **photon** γ is the electromagnetic gauge boson. It interacts only with charged particles and it is neutral, colourless and massless.
- eight **gluons g** are the QCD interaction quanta. They have colour, can interact among themselves, are massless and neutral.
- three gauge bosons (W^+, W^-, Z) associated to weak interactions. Are all colourless, but unlike gluons and photons they have masses, $m_{W^\pm} = 80.378 \pm 0.012$ GeV and $m_Z = 91.1876 \pm 0.0021$ GeV [3].

From a theoretical point of view, these particles find a description in the SM gauge symmetry group (1.1): the eight gluons correspond to the $SU(3)_C$ group generators; the photon together with the $W^\pm$ and Z are the four bosons responsible for the electroweak interaction. The physical states associated to $W^\pm$ and Z are expressed through linear combinations of the generators associated to $SU(2)_L$ and $U(1)_Y$.
The latest particle of the Standard Model is the *Higgs boson H* a spin 0 neutral particle. Experimentally observed for the first time by the ATLAS [4] and CMS [5] Collaborations in 2012, the Higgs boson represents a fundamental milestone in particle physics since it is responsible for the mass of SM particles through the *Spontaneous Symmetry Breaking (SSB)* of the electroweak symmetry down to the electromagnetism (associated to the $U(1)_{em}$ gauge group), according to the Brout-Englert-Higgs-Guralnik-Hagen-Kibble mechanism.

1.1.2 Quantum Electrodynamics

The electromagnetic interaction between electrically charged particles is classically described by the Maxwell equations while at a fundamental level it is expressed by the Quantum Electrodynamics. This quantum field theory is based on the $U(1)_{em}$ gauge group. The QED is an abelian gauge theory, which implies that one cannot have an interaction vertex in absence of fermionic sources, neither bosons self-interactions.
To obtain the QED Lagrangian [1], one takes the Dirac Lagrangian that describes free fermions and requires it to be invariant under local gauge transformation:

$$\mathcal{L}_{free} = \bar{\psi}(i\gamma^\mu \partial_\mu - m)\psi \tag{1.4}$$

where ψ is a four component Dirac spinor for a matter field, $\bar{\psi}$ is the adjoint spinor defined as $\bar{\psi} = \psi^+\gamma^0$ and $\gamma^\mu(\mu = 0, 1, 2, 3)$ are the Dirac matrices. Now, the Lagrangian (1.4) is invariant under global gauge transformations

$$\psi(x) \to \psi'(x) = \psi(x)e^{i\alpha} \tag{1.5}$$

with α a fixed phase, for it to be invariant under local gauge transformation

$$\psi(x) \to \psi'(x) = \psi(x)e^{i\alpha(x)} \tag{1.6}$$

we need to introduce a gauge field A_μ that transforms under local gauge as

$$A_\mu(x) \to A'_\mu(x) = A_\mu(x) - \frac{1}{q}\partial_\mu \alpha(x) \tag{1.7}$$

where q is the charge associated to the fermion described by the spinor $\psi(x)$. Substituting the gradient ∂_μ in (1.4) with the *gauge-covariant derivative* $\mathcal{D}_\mu$ defined as

$$\mathcal{D}_\mu \equiv \partial_\mu + iqA_\mu \tag{1.8}$$

one obtains the following gauge-invariant Lagrangian:

$$\mathcal{L} = \bar{\psi}(i\gamma^\mu \mathcal{D}_\mu - m)\psi = \mathcal{L}_{free} - qA_\mu \bar{\psi}\gamma^\mu \psi. \tag{1.9}$$

The required local gauge invariance is thus achieved through a gauge field that interacts with fermions. The final QED Lagrangian has to include also a kinetic term associated to the free propagation of the gauge boson

$$-\frac{1}{4}F_{\mu\nu}F^{\mu\nu} \quad \text{with} \quad F_{\mu\nu} = \partial_\mu A_\nu - \partial_\nu A_\mu \tag{1.10}$$

where $F_{\mu\nu}$ is the electromagnetic field-strength tensor.
The total QED Lagrangian is:

$$\mathcal{L}_{QED} = \mathcal{L}_{free} - qA_\mu \bar{\psi}\gamma^\mu \psi - \frac{1}{4}F_{\mu\nu}F^{\mu\nu}. \tag{1.11}$$

1.1.3 Quantum Chromodynamics

The strong interaction involves only quarks and it is generated by the colour quantum number. Each colour charge presents three possible states so quarks are represented as three component spinors ψ transforming under the $SU(3)$ symmetry group upon with the Quantum Chromodynamics (QCD) is based. Likewise the QED case, to construct the QCD Lagrangian [1, 6] one has to start from the free quark Lagrangian:

$$\mathcal{L}_{free} = \bar{\psi}(i\gamma^\mu \partial_\mu - m)\psi \tag{1.12}$$

where the Dirac spinor components are associated to the three colours $\psi = (\psi_{red}, \psi_{green}, \psi_{blue})$. Now one requires the local gauge invariance in this case under the $SU(3)_C$ symmetry

$$\psi(x) \to (\psi')(x) = \psi(x) e^{\frac{i}{2}\vec{\lambda}\cdot\vec{\alpha}(x)} \tag{1.13}$$

where $\lambda = (\lambda_1, ..., \lambda_8)$ are the 3×3 Gell-Mann matrices.
In order to allow for local gauge invariance, eight fields ${b^1}_\mu, ..., {b^8}_\mu$ are added to the theory and the gradient ∂_μ is substituted by the gauge-covariant derivative $\mathcal{D}_\mu$,

$$\mathcal{D}_\mu \equiv \partial_\mu + i g_s B_\mu \tag{1.14}$$

where g_s is the strong coupling constant and B_μ is defined through the gauge fields as

$$B_\mu = \frac{1}{2}\vec{\lambda}\cdot\vec{b}_\mu \tag{1.15}$$

The eight gauge fields ${b^i}_\mu$ transform under the local gauge as

$$b^l_\mu \to b'^l_\mu = b^l_\mu = f_{jkl}\alpha^j b^k_\mu - \frac{1}{g_s}\partial_\mu \alpha^l \tag{1.16}$$

where f_{jkl} are real numbers called structure constants of the group with $j, k, l = 1, ..., 8$. Substituting the gauge-covariant derivative, the Lagrangian becomes

$$\mathcal{L} = \bar{\psi}(i\gamma^\mu \partial_\mu - m)\psi - \frac{g_s}{2}\vec{b}_\mu \cdot \bar{\psi}\gamma^\mu \vec{\lambda}\psi \tag{1.17}$$

where the last term expresses the strong interaction between quarks, described by ψ and gluons, described by b^i_μ.
As already done for the total QED Lagrangian, one adds the kinetic term for the free gluon as well as their self-interaction which shows the non-abelian structure of the $SU(3)_C$ group. The QCD Lagrangian is

$$\mathcal{L}_{QCD} = \bar{\psi}(i\gamma^\mu \partial_\mu - m)\psi - \frac{g_s}{2}\vec{b}_\mu \cdot \bar{\psi}\gamma^\mu \vec{\lambda}\psi - \frac{1}{4}F^i_{\mu\nu}F^{\mu\nu i} \tag{1.18}$$

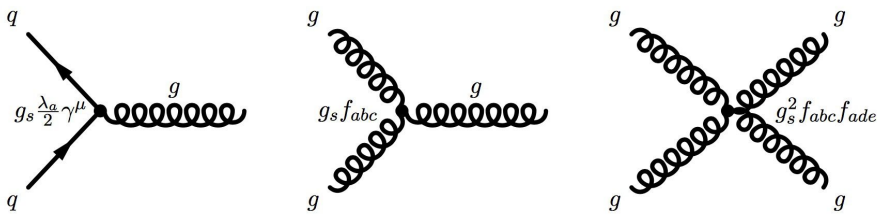

Figure 1.1: QCD boson self-interaction vertices.

where the field-strength tensor components $F^i_{\mu\nu}$ are

$$F^i_{\mu\nu} = \partial_\nu b^i_\mu - \partial_\mu b^i_\nu + g_s f_{ijk} b^j_\mu b^k_\nu \tag{1.19}$$

The interaction of gluons among themselves, Figure 1.1, is expressed through the last term. The strong coupling constant g_s depends on the energy scale of given QCD process, therefore is a *running coupling*. Specifically at low energy the strong coupling exhibits a high value, thus at high distances quarks are confined into hadrons since the strong interaction between them prevents their separation. This quark behaviour is called *confinement*. On the other hand, at high energy the strong coupling constant has a very small value, hence within the hadronic structure quarks behave as free particle. This phenomenon is called *asymptotic freedom*.

1.1.4 Quantum Flavourdynamics

The theory of weak interaction was first developed in 1934 thanks to Fermi's studies on nuclear β-decay: $n \to pe^-\bar{\nu}_e$. In this scenario, Fermi followed the example given by QED and described the weak interaction as a (point-like at low energy) vectorial current interaction of four fermions. The need for spin-1 bosons as mediators is due to divergences arising in the processes [7]:

$$(a) \quad \nu_e + e^- \to \nu_e + e^-, \quad (b) \quad \nu_e + \bar{\nu}_e \to W^+ + W^- \tag{1.20}$$

the cross section for the process (a) at $p^* > 300$ GeV/c (where p^* is the neutrino's or electron's momentum in the center of mass frame) violates the unitary limit. The solution was the introduction of massive bosons $W^\pm$, for the charged current interaction (CC), that lead to a propagator term $1/(q^2 + m^2_W)$ in the matrix element. Likewise the cross section for the process (b) has a quadratic divergence that is exactly cancelled thanks to the presence of a neutral current (NC) process mediated by Z^0.

The weak interaction behaves differently from QED and QCD, since (one of) its striking characteristic is the *parity* violation. First hinted in 1955 through the K meson decaying into two opposite parity states, it was experimentally discovered in 1957 by Madame

Wu [8] pointing out a correlation between electron spin and momentum. Driven by this observation the weak interaction vertex required to have a different form with respect to the QED or QCD. In order to satisfy Lorentz invariance as well as to allow parity violation, the weak interaction needs to be linear combination of vector (V) and axial (A) currents. Nowadays it is experimentally proven that weak interactions have a V-A structure [2]. The β-decay is thus described by the Hamiltonian of the QFD

$$H_{V-A} = \frac{G_F}{\sqrt{2}}[\bar{\psi}_p \gamma^\mu (1-\gamma^5)\psi_n][\bar{\psi}_e \gamma^\mu (1-\gamma^5)\psi_\nu] \tag{1.21}$$

where G_F is the Fermi coupling constant and γ^5 is defined as $\gamma^5 = i\gamma^0\gamma^1\gamma^2\gamma^3$.
Expressing particles fields ψ through their chiral components ψ_L and ψ_R obtained using the projectors P_L and P_R

$$\psi_L = P_L\psi = \frac{1-\gamma^5}{2}\psi \qquad \psi_R = P_R\psi = \frac{1+\gamma^5}{2}\psi \tag{1.22}$$

the weak interactions involve only left-handed particles or right-handed anti-particles, (later was discovered that also the CP symmetry was violated by some weak interactions). The strength of the weak interaction is expressed by: $\frac{G_F}{\sqrt{2}} = \frac{g_W^2}{8m_W^2}$

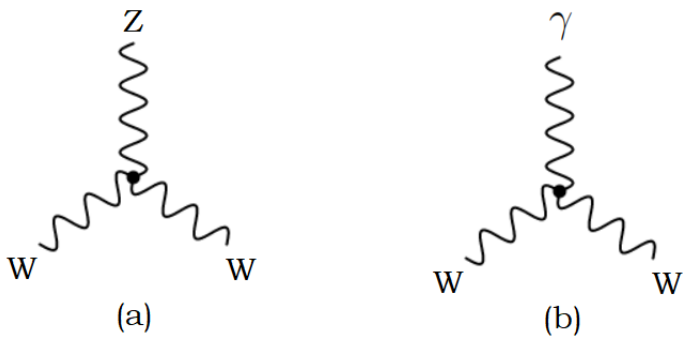

Figure 1.2: Self-interaction vertices in QFD.

where g_W is the (running) coupling constant with which one determines the fine structure constant of the QFD:

$$\alpha_W = \frac{g_W^2}{4\pi} \sim 1/30 > \alpha_{EM} \tag{1.23}$$

where $\alpha_{EM} = 1/137.1$ is the QED fine structure constant. As final note one can recall that the QFD is a non-Abelian gauge theory thus the vertices in Figure 1.2 are allowed.

1.1.5 The Electroweak theory and the Spontaneous Symmetry Breaking

A unified theory of the electromagnetic and weak interactions was developed during the 60's thanks to the individual work of Glashow [9], who first pointed out that weak interactions could also be mediated by vector gauge bosons, and Weinberg in 1967 [10] and Salam in 1968 [11] reached the same result.

The first step in the formulation of the theory is to identify a suitable symmetry group. Knowing that QED is invariant for local gauge transformation of the $U(1)$ symmetry group, one can extend this concept through the introduction of a new quantum number. The latter refers to the *weak isospin* T, generating an $SU(2)$ algebra, and the *weak hypercharge* Y, generating a $U(1)$ algebra. Hypercharge and the third component of the weak isospin T^3 are connected to the electric charge by the Gell-Mann-Nishijima formula:

$$Q = T^3 + \frac{Y}{2}. \tag{1.24}$$

The electroweak symmetry group, $SU(2)_L \otimes U(1)_Y$, with three generators $T_i = \frac{\tau_i}{2}$ (where τ_i are Pauli matrices) for $SU(2)$ and a single generator Y for $U(1)_Y$. Under the $SU(2)_L$ symmetry group, fermion fields are divided into left-hand isospin doublets and right-handed isospin singlets

$$\psi_1(x) = \begin{pmatrix} u_L \\ d_L \end{pmatrix}, \quad \psi_2(x) = u_R, \quad \psi_3(x) = d_R \tag{1.25}$$

the same for leptons, except for the neutrino whose right-handed component ν_R is not experimentally observed.
Considering now the local gauge transformation for the $U(1)_Y$ group

$$\psi(x) \to e^{i\frac{Y}{2}\alpha(x)}\psi(x) \tag{1.26}$$

where α is the space-time dependent phase, while the $SU(2)_L$ transformations only act on left-handed fermion fields

$$U_L = e^{i\frac{\tau_a}{2}\beta_a(x)} \tag{1.27}$$

where U_L are 2×2 unitary matrices and β_a free parameters. To satisfy local gauge invariance, four gauge fields are introduced: the $B_\mu(x)$ for the $U(1)_Y$ and $W^1_\mu, W^2_\mu, W^3_\mu$ for $SU(2)_L$. Then one can construct the covariant derivative as:

$$\mathcal{D}_\mu = \partial_\mu + ig'\frac{Y}{2}B_\mu(x) + ig\frac{\tau_a}{2}W^a_\mu(x), \tag{1.28}$$

where g' and g are the coupling constants for $U(1)_Y$ and $SU(2)_L$ respectively. The electroweak Lagrangian is

$$\mathcal{L}_{EW} = \sum_{j=1}^{3} i\bar{\psi}_j \gamma^\mu \mathcal{D}_\mu \psi_j(x) - \frac{1}{4} B_{\mu\nu} B^{\mu\nu} - \frac{1}{4} W^a_{\mu\nu} W^{\mu\nu}_a \tag{1.29}$$

where the first term describes lepton propagation and also contains the interaction term, while the last two terms describe EW free field propagation.
The physical states for the EW gauge bosons (γ, W^+, W^-, Z) are given by linear combination of the gauge fields

$$W^\pm_\mu = \frac{1}{\sqrt{2}} (W^1_\mu \mp i W^2_\mu) \tag{1.30}$$

representing the two charged $W^\pm_\mu$ bosons involved in the charged weak currents, while the neutral components combine in

$$A_\mu = B_\mu \cos\theta_W + W^3_\mu \sin\theta_W \tag{1.31}$$

$$Z_\mu = -B_\mu \sin\theta_W + W^3_\mu \cos\theta_W \tag{1.32}$$

where A_μ is the electromagnetic field, Z_μ the mediator of neutral weak interactions and θ_W the Weinberg angle. The latter sets the relation between the couplings g and g' as:

$$g' \equiv g \tan\theta_W, \tag{1.33}$$

motivated by the requirement

$$g \sin\theta_W = g' \cos\theta_W = e \tag{1.34}$$

needed if one wants to obtain back the term of the pure electromagnetic interaction.

An important remark concerning the Lagrangian (1.29) is that the SM gauge bosons appear to be massless, in fact only kinematic terms for free boson fieds propagation appear. The mass terms cannot be included *by hand* in $\mathcal{L}_{EW}$ because this would spoil the local gauge invariance of the theory. On the other hand these bosons should be massive due to the short-range nature of the weak interaction.

Electroweak spontaneous symmetry breaking (EWSSB)

Within the Standard Model, particles masses are generated by the *Brout-Englert-Higgs-Guralnik-Hagen-Kibble mechanism* as a consequence of the electroweak spontaneous symmetry breaking that requires the introduction of a scalar boson, the Higgs boson [12, 13]. It involves the dynamically generated mass of particles through their interaction with a scalar field which permeates the space-time.

One says that a symmetry is spontaneously broken when a stable state of a system is not symmetric under a symmetry of its Hamiltonian, Lagrangian or action [1]. Let us start by considering the breaking of a local $U(1)$ symmetry. Defining the covariant derivative as

$$\mathcal{D}_\mu \equiv \partial_\mu - ieA_\mu \tag{1.35}$$

and the scalar potential

$$V(\phi^*\phi) = \mu^2\phi^*\phi + \lambda(\phi^*\phi)^2 \tag{1.36}$$

one can write the Lagrangian for the scalar complex field ϕ

$$\mathcal{L} = (\partial_\mu + ieA^\mu)\phi^*(\partial_\mu - ieA_\mu)\phi - \mu^2\phi^*\phi - \lambda(\phi^*\phi)^2 - \frac{1}{4}F_{\mu\nu}F^{\mu\nu} \tag{1.37}$$

where λ and μ are parameters, Figure 1.3. The vacuum states of the potential are

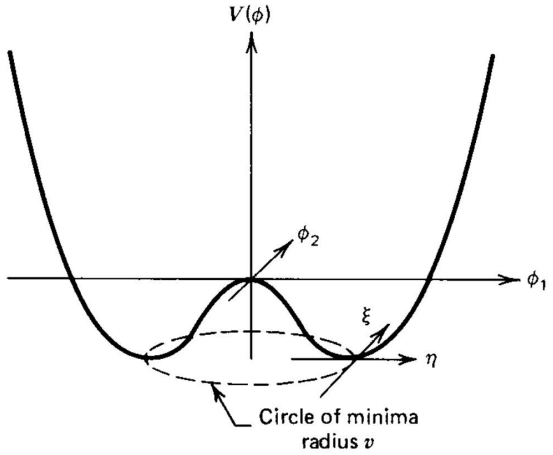

Figure 1.3: Functional behaviour of the $V(\phi)$ for a complex scalar field where $\mu^2 < 0$ and $\lambda > 0$ [6].

$$\phi_1^2 + \phi_2^2 = v^2 \quad \text{with} \quad v^2 = -\frac{\mu^2}{\lambda}. \tag{1.38}$$

Now, choosing the minimum energy state to be $\phi_1 = v$, $\phi_2 = 0$ and performing the vacuum perturbation:

$$\phi(x) = \frac{1}{\sqrt{2}}(v + \eta(x) + i\xi(x)) \tag{1.39}$$

we obtain the Lagrangian

$$\mathcal{L} = \frac{1}{2}(\partial_\mu \xi)^2 + \frac{1}{2}(\partial_\mu \eta)^2 \tag{1.40}$$

$$+ v^2 \lambda \eta^2 + \frac{1}{2} e^2 v^2 A_\mu A^\mu - ev A_\mu \partial^\mu \xi \tag{1.41}$$

$$- \frac{1}{4} F_{\mu\nu} F^{\mu\nu} + \text{interaction terms.} \tag{1.42}$$

As stated by the Goldstone theorem whenever a continuous symmetry is broken a massless scalar ξ has to appear. There are also a scalar field η and a massive vector A_μ:

$$m_\xi = 0, \tag{1.43}$$

$$m_\eta = \sqrt{2\lambda v^2}, \tag{1.44}$$

$$m_A = ev. \tag{1.45}$$

In a local gauge theory the unphysical ξ state can be eliminated through a rotation

$$\phi \to \frac{1}{\sqrt{2}}(v + h(x)) e^{i\theta(x)/v}, \tag{1.46}$$

$$A_\mu \to A_\mu + \frac{1}{ev}\partial_\mu \theta \tag{1.47}$$

where one chooses $\theta(x)$ so that $h(x)$ is real. Now, substituting the newly defined field into (1.40) one obtains

$$\mathcal{L} = \frac{1}{2}(\partial_\mu h)^2 - v^2 \lambda h^2 + \frac{1}{2} e^2 v^2 A_\mu^2 - \lambda v h^3 - \frac{1}{4}\lambda h^4 \tag{1.48}$$

$$+ \frac{1}{2} e^2 A_\mu^2 h^2 + v e^2 A_\mu^2 h - \frac{1}{4} F_{\mu\nu} F^{\mu\nu}. \tag{1.49}$$

The $U(1)$ case can be generalized to a non-abelian gauge theory. Consider a complex scalar $SU(2)_L$ Higgs doublet, with hypercharge $Y = +1$

$$\Phi \equiv \begin{pmatrix} \Phi^+ \\ \Phi^0 \end{pmatrix}, \tag{1.50}$$

its introduction leads to two new terms in $\mathcal{L}_{EW}$ (1.29): one for the scalar field Φ and another for the interactions between fermions and the scalar. The first term is

$$\mathcal{L}_\Phi = (\mathcal{D}_\mu \Phi)^\dagger - V(\Phi^\dagger \Phi) \tag{1.51}$$

where the covariant derivarive is

$$\mathcal{D}_\mu = \mathcal{I}\partial_\mu + \mathcal{I}\frac{ig'}{2}\mathcal{A}_\mu Y + \frac{ig}{2}\vec{\tau}\cdot\vec{b}_\mu \tag{1.52}$$

and the Higgs potential

$$V(\Phi^\dagger\Phi) = \mu^2(\Phi^\dagger\Phi) + |\lambda|(\Phi^\dagger\Phi)^2 \tag{1.53}$$

the scalar field develops a non-zero *vacuum expectation value* (v.e.v) for $\mu^2 > 0$, which spontaneously breaks the symmetry. After the SSB, through a $SU(2)_L$ U-gauge transformation the Lagrangian (1.51) shows the electroweak gauge bosons mass terms except for the photon

$$\mathcal{L}_\Phi = \frac{1}{2}\partial_\mu h\partial^\mu h + (v+h)^2\left(\frac{g^2}{4}W_\mu^\dagger W^\mu + \frac{g^2}{8cos^2\theta_W}Z_\mu Z^\mu\right) - \lambda v^2h^2 - \lambda vh^3 - \frac{\lambda}{4}h^4. \tag{1.54}$$

The EW symmetry breaking generates gauge boson masses leaving SM fermions massless. The mass terms for fermions can be added through the *Yukawa couplings* to the Higgs boson that one can find using the following Lagrangian for leptons

$$\mathcal{L}_{Yukawa}^{Leptons} = -G_\ell\left[(\bar{\nu}_\ell,\bar{\ell})_L\begin{pmatrix}\Phi^+\\ \Phi^0\end{pmatrix}\ell_R + \bar{\ell}_R(\Phi^-,\bar{\Phi}^0)\begin{pmatrix}\nu_\ell\\ \ell\end{pmatrix}_L\right] \tag{1.55}$$

after the SSB and substitution of $\Phi = \frac{1}{\sqrt{2}}\begin{pmatrix}0\\ v+h(x)\end{pmatrix}$ in (1.55) one gets

$$\mathcal{L}_{Yukawa}^{Leptons} = -\frac{G_\ell}{\sqrt{2}}v(\bar{\ell}_L\ell_R + \bar{\ell}_R\ell_L) - \frac{G_\ell}{\sqrt{2}}(\bar{\ell}_L\ell_R + \bar{\ell}_R\ell_L)h \tag{1.56}$$

choosing G_l so that

$$m_\ell = \frac{G_\ell v}{\sqrt{2}} \tag{1.57}$$

and hence generate the required lepton mass,

$$\mathcal{L}_{Yukawa}^{Leptons} = -m_\ell\bar{\ell}\ell - \frac{m_\ell}{v}\bar{\ell}\ell h. \tag{1.58}$$

Following the same path the quark masses can be generated. In this case to generate the mass for the upper member of a quark doublet, one must build a new Higgs doublet starting from Φ:

$$\Phi_c = -i\tau_2\Phi^* = \begin{pmatrix}-\bar{\Phi}^0\\ \Phi^-\end{pmatrix} \xrightarrow[\text{SSB}]{} \frac{1}{\sqrt{2}}\begin{pmatrix}v+h(x)\\ 0\end{pmatrix}. \tag{1.59}$$

Now, the gauge invariant term for the quarks (here the $(u,d)_L$ quark doublet), using the Higgs doublet (1.59), is given by:

$$\begin{aligned}\mathcal{L}_{Yukawa}^{Quarks} &= -G_d(\bar{u},\bar{d})_L\begin{pmatrix}\Phi^+\\ \Phi^0\end{pmatrix}d_R - G_u(\bar{u},\bar{d})_L\begin{pmatrix}-\bar{\Phi}^0\\ \Phi^-\end{pmatrix}u_R + \text{h.c.}\\ &= m_d\bar{d}d - m_u\bar{u}u - \frac{m_d}{v}\bar{d}dh - \frac{m_u}{v}\bar{u}u.\end{aligned} \tag{1.60}$$

1.1.6 Motivations for BSM Physics

Although the astonishing agreement between the predictions of Standard Model and the experimental measurement, there are still some unsolved questions. Several physics phenomena could find an explanation within theories Beyond the Standard Model (BSM). Below, one gives a brief introduction to some of the most puzzling questions:

- **The Grand Unification Theory (GUT)**: within the SM there are 18 free parameters: 3 coupling constants, 6 mass parameters for quarks, 3 mixing angles, 1 CP-violating phase, 2 parameters for the Higgs potential and other 3 mass parameters for leptons. The structure of the symmetry group $SU(3)_C \otimes SU(2)_L \otimes U(1)_Y$ reflects in different coupling constants and raises the question weather it is possible to reduce the couplings to a single one. The observation that the strength of the electromagnetic and weak interactions becomes comparable at energies $\gg M_W^2$ and the strong coupling approaches α_{QED} at very high energy seems to point to a higher level symmetry which, in the GUT framework ($E \sim 10^{16}$ TeV), might be identified with only one group of symmetry.

- **Dark Matter (DM)**: astrophysical experimental observations [14] of the rotation velocity curves of spiral galaxies, Cosmic Microwave Backgroung patterns and gravitational lensing suggest that approximately the 23% of the energy content of the Universe is composed by Dark Matter (so called since it does not interact electromagnetically). What the Dark Matter is made of can be explained, for example, by the WIMP (weakly interacting massive particles) paradigm. These are massive particle predicted by, for instance, supersymmetry (SUSY) or extra dimensions. SUSY theories are particularly appealing because they solve other SM issues such as the hierarchy problem.

- **CP-violation**: in the Standard Model the CP violation was first observed in weak interactions in K^0 oscillations [15] and more recently confirmed by B-mesons experiments [3]. The problem associated with CP-violation in the SM is that it fails to accommodate the baryon asymmetry observed in nature by several orders of magnitude, i.e. large asymmetry between the amount of matter and antimatter in our Universe. Another possible source of CP-violation in the SM could be found in the QCD Lagrangian [16]:

$$\mathcal{L}_{strongCP} = \theta \frac{\alpha_s}{8\pi} F_{a\mu\nu} F_a^{\mu\nu} \tag{1.61}$$

  which leads to an enormous neutron electric dipole moment, unless θ is tiny ($\theta < 10^{-9}$). Since CP violation is not observed in strong interactions, the CP phase is set to zero. The *strong CP problem* need to be solved starting from an extensions of the SM gauge groups which would set to zero the strong CP phase.

- **The hierarchy and naturalness problem**: this issue happens when in order to describe the macroscopic behaviour of a physical system one has to *fine tune* the parameters of the underlying microscopic theory. 't Hooft gave this definition of *naturalness* [17]: *"at any energy scale μ, a physical parameter or a set of parameters $\alpha_i(\mu)$ is allowed to be very small only if the replacement $\alpha_i(\mu) = 0$ would increase the symmetry of the system"*.
  As already seen, within the SM the values of the lepton masses are of the type $m_l = G_l v/\sqrt{2}$. This expression is only valid at the *tree-level*. To go to higher orders one needs to include some corrections for the fermion masses (i.e. one-loop contributions to the fermion propagator). These radiative corrections can have high values. Unless the mass of the particle and its correction are at most of the same order, the theory is said to have a naturalness problem. Therefore a fine-tuning on the fermion and Higgs masses should be used to erase these corrections, that otherwise would push their values to the Planck scale.

- **Neutrino masses**: within the Standard Model one needs both a lef-handed and a right-handed fermion field to couple with the Higgs boson in order to generate the mass. In the neutrino case its right-handed component has not been observed yet, implying the impossibility for the neutrino to acquire mass through the Higgs mechanism. However the SM call for a massless neutrino does not fit the experimental observation. We now know that neutrinos oscillate [18], i.e. convert from one flavour to another, thus they must have a non-zero mass. Moreover, even if one introduces the neutrino mass term into the Lagrangian, the mass difference between neutrinos and charged leptons masses would spoil the naturalness of the theory. The neutrino mass problem calls for a SM extension.

1.2 BSM: Bilepton Model and Left Right Symetric Models

As anticipated in the previous section, certain experimental evidences seem to find no match within current Standard Model formulation - typically call for larger gauge structures and a wider particle content. Moreover, there are some theoretical problems that suggest that the SM should be thought of as a low-energy theory, embedded in a larger model at scales higher than the electroweak one. In this section we will discuss two Beyond Standard Model theories upon which our research for doubly charged vector and scalar bosons is based: Bilepton Model and Left Right Symmetric Models (LRSM).

1.2.1 The Bilepton Model

Also known as 331 Model [20], is a renormalizable gauge field model based on the local gauge symmetry

$$SU(3)_C \otimes SU(3)_L \otimes U(1)_X. \tag{1.62}$$

Although conceptually identical to the SM, the 331 Model consists of a larger symmetry group obtained by extending the electroweak sector: $SU(3)_L \otimes U(1)_X$.
The gauge group associated to the strong interaction, $SU(3)_C$, remains unaltered with respect to its SM formulation. The consequence is a broadening of the particle spectrum. In fact, the model is characterised by five additional gauge bosons (four charged and one neutral) beyond those of the SM, plus three exotic quarks and extra scalars.

In the $SU(3)_L \otimes U(1)_X$ gauge symmetry also the hypercharge Y and the electric charge Q_{em} are included

$$Y = \beta^{em} T_8 + X, \tag{1.63}$$

$$Q_{em} = Y + T_3. \tag{1.64}$$

as linear combination of $T_i = \lambda_i/2$ i= 1,...,8 (with λ_i being the Gell-Mann matrices of dimension three) and X, generators of $SU(3)_L$ and $U(1)_X$ groups respectively. The 331 model is actually a class of models, parametrized by the possible values of β^{em}. In our discussion we deal with the parameterization for $\beta^{em} = \sqrt{3}$, which allows doubly-charged bileptons in the spectrum and it is chosen in the original model.

The gauge bosons associated to this model come from the combination of the gauge fields $W^a_\mu (a = 1, ..., 8)$ and B_μ of $SU(3)_L$ and $U(1)_X$ respectively [22]:

- the *charged vector bosons* are defined as

$$W^\pm_\mu = \frac{W^1_\mu \mp i W^2_\mu}{\sqrt{2}}, \qquad Y^\pm_\mu = \frac{W^4_\mu \mp i W^5_\mu}{\sqrt{2}}, \qquad Y^{\pm\pm}_\mu = \frac{W^6_\mu \mp i W^7_\mu}{\sqrt{2}} \tag{1.65}$$

  where $W^\pm$ are the weak SM bosons while $Y^\pm$ and $Y^{\pm\pm}$ are new bosons called bileptons since they have lepton number $L = \pm 2$ (hence the name).

- the *neutral vector bosons*: the SM γ, Z^0 and the new 331 neutral boson Z' are defined as linear combinations

$$A_\mu = \sin\theta_W W^3_\mu - \sqrt{3}\sin\theta_W W^8_\mu + \sqrt{1 - 4\sin^2\theta_W} B_\mu, \tag{1.66}$$

$$Z_\mu = \cos\theta_W W_\mu^3 + \sqrt{3}\sin\theta_W \tan\theta_W W_\mu^8 - \tan\theta_W \sqrt{1-4\sin^2\theta_W} B_\mu, \tag{1.67}$$

$$Z'_\mu = \frac{1}{\cos\theta_W}\sqrt{1-4\sin^2\theta_W} W_\mu^8 + \sqrt{3}\tan\theta_W B_\mu. \tag{1.68}$$

Leptons and quarks

The theoretical framework of the Bilepton model sees the fermions in the fundamental representation of $SU(3)_C$ arranged into triplets of $SU(3)_L$.

- The 331 model treats the *leptons* democratically with regard to the family. Leptons are colour singlets organized in anti-triplets of $SU(3)_L$ each with X = 0 and electric charges equal to the SM ones:

$$\ell = \begin{pmatrix} e_L \\ \nu_{eL} \\ e_R^c \end{pmatrix}, \quad \begin{pmatrix} \mu_L \\ \nu_{\mu L} \\ \mu_R^c \end{pmatrix}, \quad \begin{pmatrix} \tau_L \\ \nu_{\tau L} \\ \tau_R^c \end{pmatrix} \qquad \ell \in (\mathbf{1}, \overline{\mathbf{3}}, 0) \tag{1.69}$$

  with $\ell_R^c = i\tau_2 \ell_R^*$ ($\ell = e, \mu, \tau$ and τ_2 Pauli matrix).

- All *quarks* are colour triplets. Both the first and second quark families transform as left-handed triplets ($X = -1/3$) plus three singlets ($X = -2/3, +1/3, +4/3$) under $SU(3)_L$:

$$Q_{1,2} = \begin{pmatrix} u_L \\ d_L \\ D_L \end{pmatrix}, \quad \begin{pmatrix} c_L \\ s_L \\ S_L \end{pmatrix} \qquad Q_{1,2} \in (\mathbf{3}, \mathbf{3}, -1/3) \tag{1.70}$$

$$u_R, c_R \in (\mathbf{3}, 1, -2/3), \qquad d_R, s_R \in (\mathbf{3}, 1, +1/3), \qquad D_R, S_R \in (\mathbf{3}, 1, +4/3) \tag{1.71}$$

  while the quarks of the third family are treated differently, in this case the quarks are in a left-handed anti-triplet ($X = +2/3$) and three singlets ($X = +1/3, -2/3, -5/3$) under $SU(3)_L$:

$$Q_3 = \begin{pmatrix} b_L \\ t_L \\ T_L \end{pmatrix} \quad Q_3 \in (\mathbf{3}, \overline{\mathbf{3}}, +2/3) \tag{1.72}$$

$$b_R \in (\mathbf{3}, 1, +1/3), \qquad t_R \in (\mathbf{1}, 1, -2/3), \qquad T_R \in (\mathbf{3}, 1, -5/3) \tag{1.73}$$

  The exotic quarks D, S and T have electric charges $Q_{em} = -4/3, -4/3, +5/3$ and lepton number $L = +2, +2, -2$, while u, d, c, s, b and t have the SM electric charges.

From a phenomenological point of view, the high value of the top quark mass might suggest a special role for the third family. Although coincident at low energy with the SM, the extended theory (331) is formulated in such way to accommodate the aim of a different third family. Following this construction, the number of families $N_f = 3$ [19] may be explicable by anomaly cancellation.

Cancellation of Triangle Anomaly

One striking characteristic of the Bilepton Model is its non-trivial anomaly cancellation *among* fermion families (differently from the SM where anomaly cancellations is within the families). The arrangement of quarks and leptons is such that the triangle anomalies cancel between them neither of which separately cancels. We are interested in five fermion triangle contributions, Figure 1.4, which might be troublesome: $(3_C)^3$, $(3_C)^2X$, $(3_L)^3$, $(3_L)^2X$ and X^3, where 3_C and 3_L are $SU(3)_C$ and $SU(3)_L$ triplets respectively.

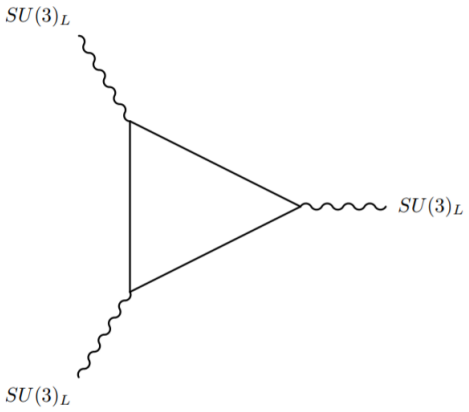

Figure 1.4: Schematic representation of the loop diagram involved in the $(3_L)^3$ anomaly.

The purely colour anomaly $(3_C)^3$ cancels because QCD is vector-like. The $(3_C)^2X$ anomaly is cancelled because quarks are in nine colour triplets with net $X = 0$ and in nine antitriplets also with net $X = 0$. The pure $SU(3)_L$ anomaly $(3_L)^3$ anomaly is non-trivial. We find this cancels only if fermions are organized in an equal number of $SU(3)_L$ triplets and antitriplets, taking into account the colour multiplicity of the quarks triplets as stated within the 331 model. $(3_L)^2X$ anomaly vanishes due to the fact that quarks are in six $SU(3)_L$ triplets with $X = -1/3$ and three antitriplets with $X = +2/3$ while all leptons have $X = 0$. Finally the X^3 anomaly vanishes because the three quark families contribute, respectively, $+6 + 6 - 12 = 0$.
Only with a matching of the number of families with the number of quark colours does the overall anomaly vanish.

Scalars of the model

For the Bilepton Model to match with the SM at low energy one needs a spontaneous symmetry breaking which is achieved through the two steps chain:

$$SU(3)_L \otimes U(1)_X \to SU(2)_L \otimes U(1)_Y \to U(1)_{em} \tag{1.74}$$

The minimum Higgs structure is given by the scalar sector of the model which consists of three $SU(3)_L$ triplets and one sextet:

$$\rho = \begin{pmatrix} \rho^{++} \\ \rho^{+} \\ \rho^{0} \end{pmatrix} \in (1,3,1), \qquad \eta = \begin{pmatrix} \eta^{+} \\ \eta^{0} \\ \eta^{-} \end{pmatrix} \in (1,3,0), \qquad \chi = \begin{pmatrix} \chi^{0} \\ \chi^{-} \\ \chi^{--} \end{pmatrix} \in (1,3,-1) \tag{1.75}$$

$$\sigma = \begin{pmatrix} \sigma_1^{++} & \sigma_1^{+}/\sqrt{2} & \sigma^{0} \\ \sigma^{+}/\sqrt{2} & \sigma_1^{0} & \sigma_2^{-}/\sqrt{2} \\ \sigma^{0}/\sqrt{2} & \sigma^{-}/\sqrt{2} & \sigma_2^{--} \end{pmatrix} \qquad \sigma \in (1,6,0) \tag{1.76}$$

The breaking of the $SU(3)_L \otimes U(1)_X$ symmetry to $SU(2)_L \otimes U(1)_Y$ is accomplished by the v.e.v. v_ρ acquired by the neutral component of the ρ scalar triplet. The next step is basically the Standard Model EWSSB of $SU(2)_L \otimes U(1)_Y$ through the v.e.v's v_η, v_χ of the neutral scalars η^0 and χ^0 of η and χ scalar triplets.
Taking in consideration the gauge and Lorentz invariant term in the Lagrangian

$$\mathcal{L}_\phi = \left((\mathcal{D}_\mu \phi)^\dagger (\mathcal{D}_\mu \phi)\right) + V(\phi) \tag{1.77}$$

where $\phi = \rho, \eta, \chi$ and the covariant derivative takes two different forms, one for the triplets

$$\mathcal{D}_\mu \phi = \partial_\mu \phi - i\frac{g}{2}\mathcal{M}_\mu \phi - i g_X X_\phi B_\mu \phi \qquad \text{with} \qquad \phi = \rho, \eta, \chi \tag{1.78}$$

and one for the sextet

$$\mathcal{D}_\mu \sigma = \partial_\mu \sigma - i\frac{g}{2}\left[\mathcal{M}_\mu \sigma - \sigma^T \mathcal{M}_\mu^T\right] - i g_X X_\sigma B_\mu \sigma. \tag{1.79}$$

In (1.78) and (1.79) X_ϕ and X_σ are the triplet and sextet $U(1)_X$ charge respectively, while g and g_X are the coupling constants of $SU(3)_L$ and $U(1)_X$ which are related trough the electroweak mixing angle θ_W as follow:

$$\frac{g_X^2}{g^2} = \frac{\sin^2\theta_W}{1 - 4\sin^2\theta_W}. \tag{1.80}$$

Then we have the matrix $\mathcal{M}_\mu$ defined as:

$$\mathcal{M}_\mu = \begin{pmatrix} W_\mu^3 + \frac{1}{\sqrt{3}}W_\mu^8 & \sqrt{2}W_\mu^{+} & \sqrt{2}Y_\mu^{-} \\ \sqrt{2}W_\mu^{-} & W_\mu^3 - \frac{1}{\sqrt{3}}W_\mu^8 & \sqrt{2}Y_\mu^{--} \\ \sqrt{2}Y_\mu^{+} & \sqrt{2}Y_\mu^{++} & -\frac{2}{\sqrt{3}}W_\mu^8 \end{pmatrix} \tag{1.81}$$

The spontaneous symmetry breaking of (1.77) leads to the physical states associated to the scalar bosons as well as to the gauge vector bosons:

- 5 neutral scalars h_i (the SM Higgs boson is among them)
- 3 neutral pseudoscalars A_i
- 4 single charged Higgses $H_i^{\pm}$
- 3 doubly charged Higgses $H_i^{\pm\pm}$
- 2 neutral vector bosons Z^0, Z' (where Z^0 is the SM weak boson)
- 2 charged vector bosons $W^{\pm}, Y^{\pm}$ (where $W^{\pm}$ is the SM weak boson)
- 1 doubly charged vector boson $Y^{\pm\pm}$

where the gauge vector bosons $Z^0, Z', W^{\pm}, Y^{\pm}, Y^{\pm\pm}$ have acquired mass through the Goldstone bosons generated in the SSB.
The Yukawa term of interaction for SM and exotic quarks are obtained by mean of the scalar triplets:

$$\begin{aligned}\mathcal{L}_{q,triplet}^{Yukawa} = y_d^1 Q_1 \eta^* d_R + y_d^2 Q_2 \eta^* s_R + y_d^3 Q_3 \chi b_R^* + y_u^1 Q_1 \chi^* u_R^* + y_u^2 Q_2 \chi^* c_R^* \\ + y_u^3 Q_3 \eta t_R^* + y_E^1 Q_1 \rho^* D_R^* + y_E^2 Q_2 \rho^* S_R^* + y_E^3 Q_3 \rho T_R^* + h.c.\end{aligned} \tag{1.82}$$

where y_d^i, y_u^i and y_E^i are the Yukawa couplings for down-, up-type and exotic quarks.
The SM quarks acquire mass through the Yukawa couplings right after the scalar triples assume the v.e.v value. One can notice that the masses of the exotic quarks are related to the v.e.v of ρ^0: since $v_\rho \gg v_{\eta,\chi}$, the exotic quarks have larger mass values ($\mathcal{O}(TeV)$) with respect to SM quarks whenever the relation $y_E^i \sim 1$ is satisfied.

The lepton mass generation is obtained differently with respect to the SM. Within the SM the mass term for leptons is associated with the operator $\bar{\ell}_L H e_R$ with $\ell_L = (\nu_{eL}, e_L)$. In the 331 model, both the chiral left and right components of the leptons are embedded in the same $SU(3)_L$ triplet. To solve this, the presence of a scalar sextet σ is needed. The Yukawa term for leptons in the 331 model is:

$$\mathcal{L}_{\ell}^{Yukawa} = \mathcal{L}_{\ell,triplet}^{Yukawa} + \mathcal{L}_{\ell,sextet}^{Yukawa} \tag{1.83}$$

The triplet contribution depends on η since it is the only scalar multiplet with $X = 0$, and it is expressed by:

$$\mathcal{L}_{\ell,triplet}^{Yukawa} = G_{ab}^{\eta} \ell_a^i \ell_b^j \eta^{*k} \psi^{ijk} + h.c. \tag{1.84}$$

where $a, b = e, \mu, \tau$ while $i, j, k = 1, 2, 3$ are $SU(3)_L$ indexes. G^{η}_{ab} is an antisymmetric matrix which has to be diagonalized in order to get the lepton mass terms.
The Yukawa term associated to the coupling between the sextet and leptons is:

$$\mathcal{L}^{Yukawa}_{\ell,sextet} = G^{\sigma}_{ab}\ell^{i}_{a}\ell^{j}_{b}\sigma^{*}_{i,j} + h.c. \tag{1.85}$$

where G^{σ}_{ab} is a matrix symmetric in flavour space.
Through the SSB η^0 acquired v.e.v. as well as the neutral components σ^0, σ^0_1 of the scalar sextet. The resulting Yukawa term associated to the leptons is:

$$\mathcal{L}^{Yukawa}_{\ell} = \left(\sqrt{2}\sigma^{0}G^{\sigma}_{ab} + 2v_{\eta}G^{\eta}_{ab}\right)(e_{aL}e^{c}_{bR}) + \sigma^{0}_{1}G^{\sigma}_{ab}\left(\nu^{T}_{L}i\tau_{2}\nu_{L}\right) \tag{1.86}$$

where τ_2 is the Pauli matrix. This expression contains the mass terms associated to the charged leptons as well as the Majorana mass terms for the neutrinos.

Phenomenological aspects at LHC

The Bilepton Model predicts doubly charged particles, moreover this is the only BSM theory to predict a vector doubly charged boson $Y^{\pm\pm}$. This is a really interesting signal to search thanks to its peculiar signature rarely seen in Standard Model processes. The main processes leading to $H^{\pm\pm}$ and $Y^{\pm\pm}$ production are Drell-Yan scattering mediated by a neutral vector ($V^0 = \gamma, Z^0, Z'$) or scalar ($h_1, ..., h_5$) boson. Also the exchange of an exotic quark ($Q = D, S, T$) in the *t-channel* contributes to their production as show in Figure1.5. By lepton number conservation bileptons must be produced in pairs or in association with a heavy quark. Speaking of the 331 Model and bileptons decays, one has to say that the flavour violation is not allowed within this model. This fact, combined with $Y^{\pm\pm}$ and $H^{\pm\pm}$ having $L,\ Q = \pm 2$ leaves the only possible decay the one to same-charge same-flavour lepton pairs with a branching ratio $BR(Y^{\pm\pm}/H^{\pm\pm} \to \ell^{\pm}\ell^{\pm}) \simeq 1/3$ with $\ell = e, \mu, \tau$.

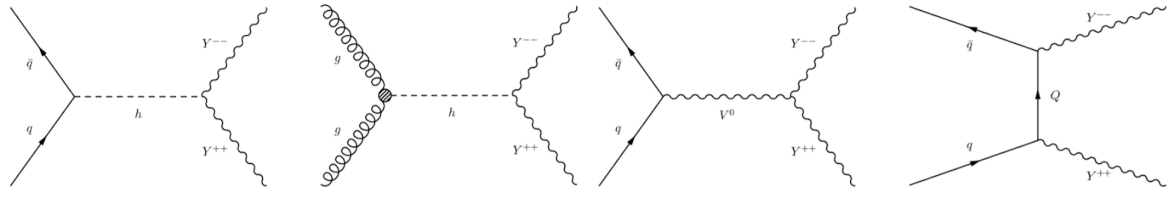

Figure 1.5: Typical contributions to events with two dileptons in the final state: (a) and (c) are Drell-Yan like processes, where h is the SM-like Higgs boson and V^0 is a photon or a Z^0 boson; (b) dilepton-pair production by gluon fusion, mediated by a h; (d) dilepton production via the exchange of an exotic quark Q in the t-channel [21].

At LHC the potential for discovering bileptons in $pp \to Y^{++}Y^{--} \to \mu^+\mu^+\mu^-\mu^-$, with jetless Y-pair production mediated by a neutral vector boson or a leptoquark Q, reported in this paper [23], was extended to $\sqrt{s} = 13$ TeV and $\mathcal{L} = 50$ fb^{-1} [24] resulting in the exclusion for $m_{Y^{\pm\pm}} > 850$ GeV, Figure 1.6.

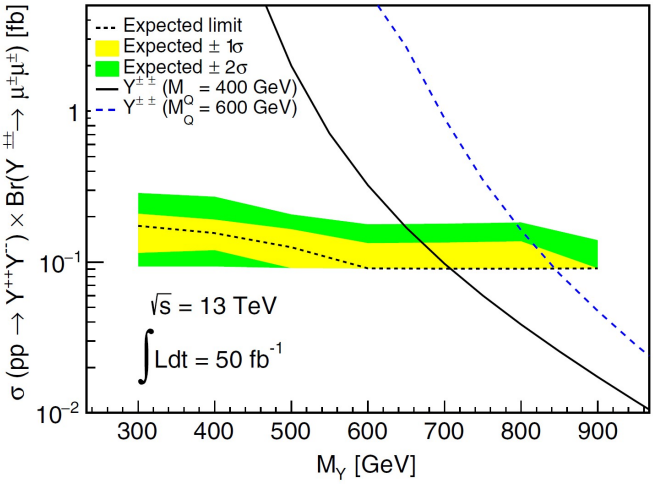

Figure 1.6: Upper limits on $\sigma \times BR$ assuming 50 fb^{-1} of data at $\sqrt{s} = 13$ TeV [23].

Another analysis on same-charge same-flavour lepton pairs produced at the LHC through dileptons ($H^{\pm\pm}$ or $Y^{\pm\pm}$) from 331 model is presented here [25]. The main purpose of this study is to compare the signature associated to the vector or scalar boson in jetless events:

$$pp \to Y^{++}Y^{--}(H^{++}H^{--}) \to \ell^+\ell^+\ell'^-\ell'^- \tag{1.87}$$

with $\ell, \ell' = e, \mu$ at $\sqrt{s} = 13$ TeV. Here some selection criteria on the final state leptons kinematic variables are also applied:

$$p_{T,\ell} > \ 20 \text{ GeV}, \qquad |\eta_\ell| < 2.5, \qquad \Delta R_{\ell\ell} > 0.1. \tag{1.88}$$

In this case the authors chose a common benchmark point for both vector and scalar boson masses $m_{Y^{\pm\pm}} = m_{h^{\pm\pm}} = 878.3$ GeV since it is above the exclusion limits resulting from both ATLAS [26] and CMS [27] researches on doubly charged Higgs.
The following cross sections have been evaluated:

$$\sigma(pp \to Y^{++}Y^{--} \to 4\ell) \simeq 4.3 \text{ fb}, \tag{1.89}$$

$$\sigma(pp \to H^{++}H^{--} \to 4\ell) \simeq 0.3 \text{ fb}, \tag{1.90}$$

$$\sigma(pp \to ZZ \to 4\ell) \simeq 6.1 \text{ fb}. \tag{1.91}$$

as one can see the main background is the ZZ pair production while the contribution from $pp \to hh \to 4l$ is negligible ($\sigma(pp \to hh) \sim 40$ fb at $\sqrt{s} = 13$ TeV) where h is the SM Higgs. The computed cross sections (1.89) and (1.90) show a larger value for vector-bilepton production with respect to the scalars, the reason should be found in the different spin values of the intermediate bileptons: $H^{++}H^{--}$ pair production is observed when the intermediate vector neutral boson state has zero helicity, while for $Y^{++}Y^{--}$ production one has to consider also the ± 1 helicity values. The exciting result from this study is that LHC is sensitive to $Y^{\pm\pm}$ searched, already at 13 TeV and 300 fb^{-1}. It has been found that the signal from $Y^{++}Y^{--}$ can be separated from the ZZ background with significance $s \sim 6.9$, while $H^{++}H^{--}$ production is overwhelmed by both Standard Model background ($s = 0.6$) and possible vector-bilepton pairs ($s = 0.9$).
A successive study was carried out in [28]. Here the analysis focuses as well on the process (1.87) and it is conducted at truth level with MC generated samples for a centre of mass energy $\sqrt{s} = 13$ TeV where a common benchmark mass point $m_{Y^{\pm\pm}} = m_{H^{\pm\pm}} = 1$TeV is set. New variables to discriminate the $H^{\pm\pm}$ from $Y^{\pm\pm}$ were considered following a multivariate analysis approach. The results showed that, although signals from two bileptons are similar, it is possible to discriminate the vector boson from the scalar one with a maximum rejection power for the scalar hypothesis at 80% CL.

1.2.2 The Left-Right Symmetric Models

We now introduce an alternative extension of the Standard Model known as LRSM [29, 30, 31].
Left-Right Symmetric Models' qualitative argumentation is based on the weak interaction parity violation due to the selective coupling of the weak gauge bosons only to left-handed fermions. The idea is that this violation happens at low energy scales but the symmetry can be restored at high energies by extending the SM gauge group. The model is based on the larger gauge symmetry group

$$SU(3)_C \otimes SU(2)_L \otimes SU(2)_R \otimes U(1)_{B-L}. \tag{1.92}$$

One can see that this model is characterized by the addition of right-handed counterparts for the W and Z weak bosons since the gauge group associated to the electroweak sector is $SU(2)_L \otimes SU(2)_R \otimes U(1)_{B-L}$ where B and L are the barionic and leptonic number. Seven generators are present: three for each $SU(2)_{L,R}$ group ($T_{iL.R}$) and one for the $U(1)_{B-L}$ group (X). These correspond to seven gauge bosons $W^{\mu}_{iL,R}$ and B^{μ}. It is important to notice that the effect of the LRSM is to duplicate the weak gauge bosons linear combination of the physical states. The B and L charges are fixed using the Gell-Mannlike formula:

$$Q = T_{3L} + T_{3R} + \frac{B-L}{2} \tag{1.93}$$

In this model leptons and quarks are associated with the irreducible representation of (1.92):

$$\psi_{L,i} = \begin{pmatrix} \nu_l \\ l \end{pmatrix}_{L,i} : (\mathbf{1}, \mathbf{2}, \mathbf{1}, -1) \qquad \psi_{R,i} = \begin{pmatrix} \nu_l \\ l \end{pmatrix}_{R,i} : (\mathbf{1}, \mathbf{1}, \mathbf{2}, -1) \tag{1.94}$$

$$Q_{L,i} = \begin{pmatrix} u \\ d \end{pmatrix}_{L,i} : (\mathbf{3}, \mathbf{2}, \mathbf{1}, 1/3) \qquad Q_{R,i} = \begin{pmatrix} u \\ d \end{pmatrix}_{R,i} : (\mathbf{3}, \mathbf{1}, \mathbf{2}, 1/3) \tag{1.95}$$

where $i = 1, 2, 3$ represents the family index and the subscripts L, R refers to the left- and right-handed chiral component. Under parity transformation $\psi_L \leftrightarrow \psi_R$ and $Q_L \leftrightarrow Q_R$. One defines the covariant derivative for the group as

$$\mathcal{D}_\mu = \partial_\mu - ig \sum_{j=1}^{3} (W_{Lj\mu} T_{Lj\mu} + W_{Rj\mu} T_{Rj\mu}) - ig' B_\mu Y \tag{1.96}$$

where $Y = (B-L)/2$, g' is the $U(1)_{B-L}$ coupling constant and g is the common value set for the couplings for left (g_L) and right (g_R) weak interaction to make the lagrangian invariant under parity transformations. One can define an analogous of the Weinberg angle starting from the strength of g and g':

$$\sin\theta_W = -\frac{g'}{\sqrt{g^2 + 2g'^2}}. \tag{1.97}$$

The total LRSM Lagrangian is invariant for $SU(2)_L \to SU(2)_R$:

$$\mathcal{L}_{gauge} = i\left[\bar{\psi}_L \gamma \mathcal{D}^\mu \psi_L + \bar{\psi}_R \gamma \mathcal{D}^\mu \psi_R\right] - \frac{1}{4} F_{\mu\nu} F^{\mu\nu} - \frac{1}{4} G^i_{L\mu\nu} G^{i\mu\nu}_L - \frac{1}{4} G^i_{R\mu\nu} G^{i\mu\nu}_R, \quad (1.98)$$

where

$$F_{\mu\nu} = \partial_\mu B_\nu - \partial_\nu B_\mu \quad (1.99)$$

$$G^i_{L,R\mu\nu} = \partial_\mu W^i_{L,R\nu} - \partial_\nu W^i_{L,R\mu} + g\epsilon^{i,j,k} W^j_{L,R\mu} W^k_{L,R\nu} \quad (1.100)$$

are the field propagation terms, $W_{iL,R}$ and B are the unphysical gauge bosons. The physical charged gauge boson states are given as a combination

$$W^+_{L,R} = \frac{W_{1L,R} - iW_{2L,R}}{\sqrt{2}} \quad (1.101)$$

$$W^-_{L,R} = \frac{W_{1L,R} + iW_{2L,R}}{\sqrt{2}} \quad (1.102)$$

where $W^\pm_L$ can be identified with the SM W bosons. Similarly, the rotation relating the fields $W_{3L,R}$ and B with A and $Z^0_{L,R}$ through the angles $\cos\theta_W$ and $\sin\theta_W$ returns the SM Z^0 (Z^0_L) and a right-handed Z^0_R boson.

Now we describe the breaking of the new group of symmetry to the SM group. To do so the Higgs scalar sector of the LRSM is enlarged by the following multiplets:

$$\mathbf{\Phi} = \begin{pmatrix} \phi^0_1 & \phi^+_2 \\ \phi^-_1 & \phi^0_2 \end{pmatrix}, \qquad \Delta_{L,R} = \begin{pmatrix} \Delta^+/\sqrt{2} & \Delta^{++} \\ \Delta^0 & -\Delta^+\sqrt{2} \end{pmatrix}. \quad (1.103)$$

The SSB in this case consists of two steps. All the neutral components of the Higgs fields acquire a v.e.v of the type:

$$\langle \Phi \rangle = \begin{pmatrix} v_1 & 0 \\ 0 & v_2 e^{i\alpha} \end{pmatrix}, \quad \langle \Delta_L \rangle = \begin{pmatrix} 0 & 0 \\ v_L e^{i\theta_L} & 0 \end{pmatrix}, \quad \langle \Delta_R \rangle = \begin{pmatrix} 0 & 0 \\ v_R & 0 \end{pmatrix}. \quad (1.104)$$

Firstly the symmetry $SU(2)_R \times U(1)_{B-L} \to U(1)_Y$ is broken at high energy scales through the vacuum expectation values $\langle \Delta_R \rangle \equiv v_R$ and $\langle \Delta_L \rangle \equiv v_L = 0$ which is responsible responsible for the masses of new gauge bosons W_R and Z_R

$$M^2_{W_R} \simeq g^2_R v^2_R, \quad M^2_{Z_R} \simeq (2g^2_R + g'^2) v^2_R \quad (1.105)$$

Then, at the electroweak energy scale, the usual SM spontaneous symmetry breaking $SU(2)_L \otimes U(1)_Y \to U(1)_{em}$ takes place through the v.e.v acquired by Φ: $\langle \Phi \rangle = diag(v_1, v_2 e^{i\alpha})$ which gives the mass to the left-handed charged gauge boson

$$M^2_W = \frac{g^2_L}{2v^2}. \quad (1.106)$$

These v.e.vs are connected by the relation:

$$v_L \propto \frac{v^2}{v_R}. \tag{1.107}$$

The result is the introduction into the model of a neutral scalar Higgs boson as well as singly and doubly charged Higgs bosons. This model predicts the existence of two doubly charged Higgs bosons, $\Delta_L^{\pm\pm}$ and $\Delta_R^{\pm\pm}$ that differ in their couplings with SM particles. In this paper [32] an estimate of the potential for observation at LHC of a doubly charged Higgs boson was proposed. The doubly charged Higgs bosons at the LHC can be produced both by vector boson fusion, $W^+W^+ \to \Delta_{L,R}^{++}$ and pair production by the Drell-Yan processes $q\bar{q} \to \Delta_{L,R}^{++}\Delta_{L,R}^{--}$. The single production, that also can happen via the fusion of a singly-charged Higgs with either a W or another singly-charged Higgs, is not considered in our study. We are interested in the pair production with γ, Z^0 or $Z_{L,R}^0$ exchanged in the $s-$channel, which in the case of Δ_L^{++} may be the only possibility if v_L is very small. The decay in two leptons provides a clean signature (two prompt isolated leptons), but the branching ratios depend on the Yukawa couplings that are consistent with $O(1$ TeV) if the mass scale of the triplet is large, then decay signature $q\bar{q} \to \gamma^*/Z^{0*}/Z'^* \to \Delta_L^{++}\Delta_L^{--} \to 4l$ would be the dominant $\Delta_L^{\pm\pm}$ decay mode for small v_L. Another possible decay is $\Delta_{L,R}^{\pm\pm} \to W_{L,R}^{\pm}W_{L,R}^{\pm}$ which is kinematically suppressed for $\Delta_R^{\pm\pm}$ and also for $\Delta_L^{\pm\pm}$ due to the small coupling v_L. The pair production cross-section for $\Delta_L^{++}\Delta_L^{--}$ is about 2.3 times larger than for $\Delta_R^{++}\Delta_R^{--}$, in Figure 1.7 the obtained contours of discovery are shown.

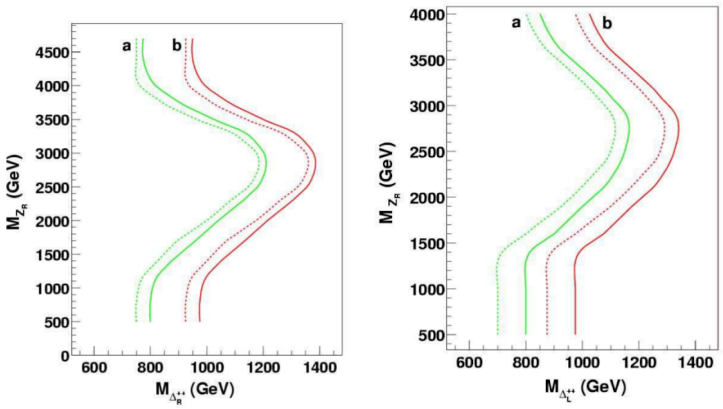

Figure 1.7: Contour of discovery in the plane $m_{Z'}$ vs $m_{\Delta_R^{++}}$ (left) and in the plane $m_{Z'}$ vs $m_{\Delta_L^{++}}$ (right). Results refer to LHC integrated luminosities of 100 fb^{-1} (a) and 300 fb^{-1} (b). All four leptons observed (dashed lines), only three leptons observed (full lines) [32].

More recently a research for doubly charged Higgs bosons was conducted by the ATLAS Collaboration [26, 33]. The proton-proton collisions data at $\sqrt{s} = 13$ TeV

corresponding to 36.1 fb^{-1} of integrated luminosity have been used. The analysis aimed to fit the dilepton mass spectra in several exclusive signal regions exploring the decays: $\Delta^{\pm\pm} \to e^{\pm}e^{\pm}$, $\Delta^{\pm\pm} \to \mu^{\pm}\mu^{\pm}$ and the lepton flavour violating decay $\Delta^{\pm\pm} \to e^{\pm}\mu^{\pm}$. Considering only pair production by Drell-Yan process, the coupling to W has been assumed to be negligible. The total assumed branching ratio is

$$BR(\Delta^{\pm\pm} \to \ell^{\pm}\ell^{\pm}) + BR(\Delta^{\pm\pm} \to X) = 100\% \tag{1.108}$$

where $\ell = e, \mu$ and the X are states which include τ leptons. No significant evidence of a signal has been observed but some exclusion limits on $m_{\Delta^{\pm\pm}}$ have been determined, Figure 1.8.

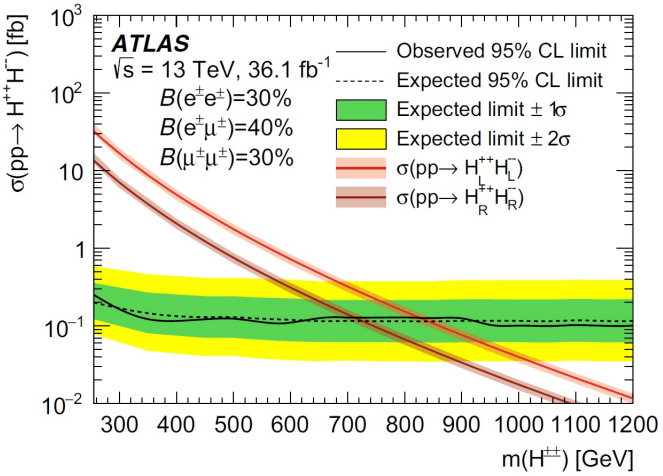

Figure 1.8: Upper limit on the cross-section $pp \to H^{++}H^{--}$ for branching ratio values $BR(e^{\pm}e^{\pm}) = 30\%$, $BR(e^{\pm}\mu^{\pm}) = 40\%$, $BR(\mu^{\pm}\mu^{\pm}) = 30\%$ ($H^{\pm\pm}$ corresponds to $\Delta^{\pm\pm}$ in this section) [26].

Chapter 2

The ATLAS experiment at the LHC

The European Organization for Nuclear Research [34] was founded in 1954. The idea of creating a European atomic physics laboratory was first proposed by the french physicist Louis de Broglie right after the end of World War II and accepted during an intergovernmental meeting of UNESCO in 1951. Nowadays it counts 23 member states and its primary mission is fundamental research in nuclear and high energy physics, but also plays a major role in developing new technologies from materials science to computing.
Inside the tunnels underneath the CERN facility, the world's largest proton accelerator, the Large Hadron Collider (LHC) is hosted. It was designed as the next step, after the Large Electron-Positron Collider (LEP), to reach the highest energy ever explored in particle physics and to discover the SM last missing piece: the Higgs boson. Along the LHC tunnel four main experiments are located in underground facilities: ATLAS, CMS, LHCb and ALICE.
Among the successes collected thanks to LHC, stands out the discovery of the Higgs boson made by the ATLAS and CMS Collaborations in 2012 [4, 5]. Moreover, if new particles exist around the TeV scale, the LHC should be able to find them. Here after we illustrate the LHC machine and the technology beyond particle acceleration, focusing on the ATLAS experiment.

2.1 The Large Hadron Collider

The LHC [35] is a circular accelerator consisting of a 27 km ring installed between 50 and 175 m underground in the tunnel previously hosting the LEP at CERN in Geneva. The LHC is designed to accelerate both protons and heavy ions (mainly lead) up to a center of mass energy of $\sqrt{s} = 14$ TeV and $\sqrt{s} = 2.76$ TeV/nucleon respectively. The collider consists of two adjacent parallel beam pipes where two particle beams circulate in opposite direction, see Figure 2.1. Exploiting the magnetic field generated through superconducting magnets and accelerating structures (radio-frequencies cavities) placed

along the ring, charged particles are deflected and accelerated. After increasing the particle energy, they are made to collide in correspondence of the four main detectors (ATLAS, CMS, LHCb and ALICE). The particles in each beam are packed into bunches produced through pulsed fields. Each bunch contains $\sim 10^{11}$ protons and collide every 25 ns.

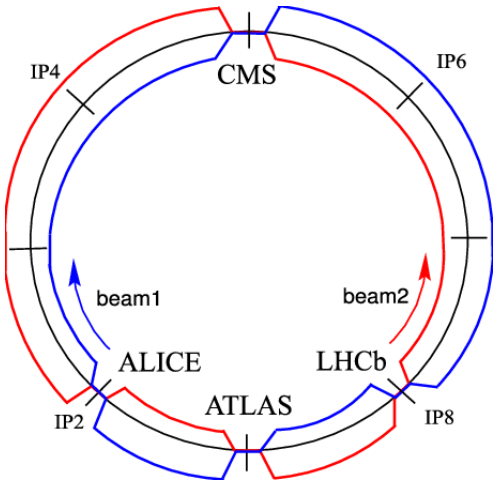

Figure 2.1: LHC minimal layout: there are 8 interaction points (IPs), only 4 of them correspond to the detectors locations.

An impressive number of different magnets is employed to properly focus and direct the particles beams along the ring path: 1232 15-meters long superconductive dipole magnets generate a 8.4 T magnetic field in order to make the proton beams' trajectories circular; for this purpose an electric current of 12 kA is needed as well as a temperature of 1.9 K, reached through the world's largest cryogenic system which employs superfluid helium at atmospheric pressure. In addition to magnetic dipoles, 392 3-meters long quadrupoles are employed to focus the beams; finally sextupole, octupole and decapole magnets are used to correct small imperfections of the magnetic field produced by the dipoles.
LHC became operative in 2008 starting the Run1 lasted until 2012. After the 2013-2014 Long Shutdown I, the LHC was upgraded: an energy of 6.5 TeV per beam has been reached, producing proton-proton collisions of 13 TeV. In 2015 LHC resumed its operations starting Run 2 ended in 2018. In Table 2.1 [36] is shown the machine performance in Run 2. Currently we are approaching the end of the Long Shoutdown II since the start of operations for Run 3 are scheduled for 2021 with a center of mass energy increased to 14 TeV.

Parameter	2015	2016	2017	2018
Number of colliding bunches n_B	2232	2208	2544/1909	2544
Bunch spacing (ns)	25	25	25/8b4e	25
Protons per bunch (10^11)	1.1	1.1	1.1/1.2	1.1
Peak luminosity ($10^{33} cm^{-2} s^{-1}$)	5	13	16	19
Pile-up (μ)	~ 16	~ 41	$\sim 45/60$	~ 55
Mean inelastic interaction per bunch crossing	13	25	38	36
Total delivered integrated luminosity fb^{-1}	4.0	38.5	50.2	63.4

Table 2.1: LHC parameters for pp collisions at $\sqrt{s} = 13$ TeV during Run 2. In 2017 LHC worked also using a different bunch configuration "8b4e" meaning eigh bunches separated by 25 ns followed by four bunches slot gap.

The *Luminosity* is among the parameters that most characterises a collider. It is defined depending on the machine properties and the physics processes that occur within the machine. The *instantaneous luminosity* $\mathcal{L}$, measured in $\text{cm}^{-2}\text{s}^{-1}$ is defined as the ratio

$$\mathcal{L} = \frac{R}{\sigma} \tag{2.1}$$

where R is the rate of produced events and σ is the process cross section. At the LHC, this quantity depends on beam properties

$$\mathcal{L} = \frac{N_p^2 n_b f \gamma}{4\pi \epsilon_n \beta^*} F \tag{2.2}$$

where N_p is the number of protons, n_b the number of bunches per beam, f is the revolution frequency, $\gamma = E/m$ is the relativistic factor, ϵ_n is the normalize beam emittance, β^* is the focal length at the collision point and F is the luminosity reduction factor. It is important to notice that the luminosity gradually decreases throughout a Run due to the degradation of the beams' intensity, according to the following expression:

$$\mathcal{L}(t) = \mathcal{L}_0 \cdot e^{\frac{t}{\tau}} \quad \text{with} \quad \tau \sim 15\text{h}. \tag{2.3}$$

Another important parameter is the *luminosity integrated in time (T)*, measured in fb^{-1}, defined as the ratio of the number of events N produced at a rate R with a certain cross section σ:

$$L = \int_T^0 \mathcal{L}\, dt = \frac{N}{R} \tag{2.4}$$

during the Run 2 period, ATLAS collected a total integrated luminosity of 139fb^{-1} [36].

2.1.1 The acceleration and detectors systems

The protons used to form the bunches circulating in LHC are produced starting from a bottle containing Hydrogen gas connected to a *duoplasmatron source*. The principle is to create plasma from Hydrogen gas separating protons from electrons applying an electric field. Protons are not directly injected into the LHC ring, their energy needs first to be progressively increased by different machines composing the *acceleration chain* [37] as shown in Figure 2.2:

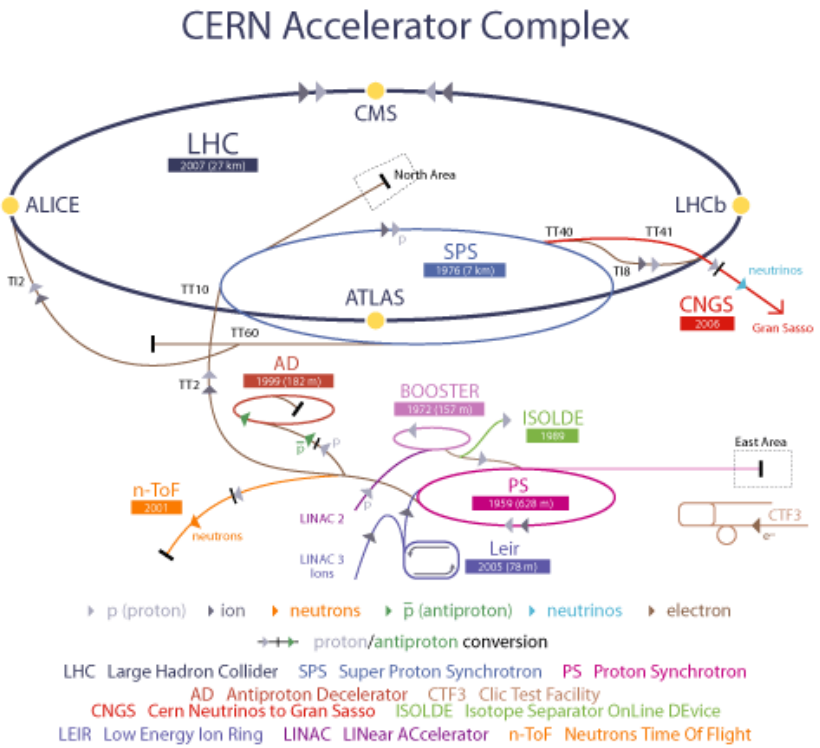

Figure 2.2: CERN accelerator complex, a schematic view of acceleration chain and location of the main LHC experiments.

- **LINAC2**: is the stating point for the protons used in experiments at CERN. It is a radiofrequency cavity linear accelerator used to bring protons energy up to 50 MeV while small quadrupole magnets ensure that the protons remain in a tight beam.
- **Proton Synchrotron Booster (PBS)**: composed by four superimposed synchrotrons rings, accelerating protons coming from LINAC2 up to 1.4 GeV for the injection to the protron synchrotron (PS).

- **Proton Synchrotron (PS)**: accelerates either protons from PBS or heavy ions from the Low Energy Ion Ring (LEIR), Figure 2.2. The PS was CERN's first synchrotron. It is a circular accelerator with a circumference of 628 m and operates at up to 25 GeV. 277 room-temeperature electromagnets, including 100 dipoles are employed to bend the beams round the ring. Also, the PS produces a 25 ns-separated bunch beam.

- **Super Proton Synchrotron (SPS)**: with a circumference of 7 km, it is the second-largest machine in the CERN's accelerator complex and accelerates protons coming from PS up to 450 GeV. It provides beams for the LHC (and other experiments). The SPS uses 1317 room-temperature electromagnets, including 744 dipoles to bend the beams round the ring.

- **Large Hadron Collider (LHC)**: at the end of this chain, particles are eventually ready to enter into the two beam pipes of the LHC, one circulating clockwise and the other one anticlockwise. The injection is done in the *injection insertions* corresponding to the IP2 and IP8 in Figure 2.1 where the beam approaches the LHC from outside and below the machine plane. Protons are then accelerated up to 6.5 TeV in 20 minutes.

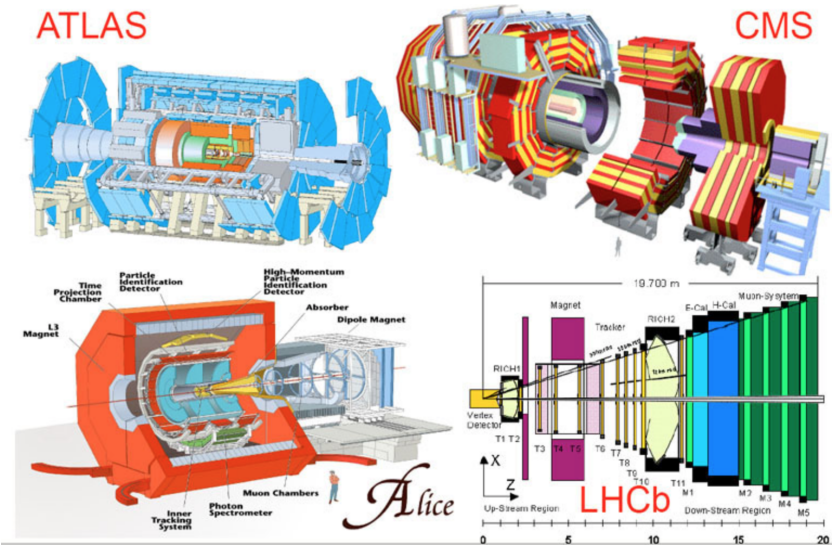

Figure 2.3: Layouts for the main LHC experiments: ATLAS, CMS, ALICE and LHCb.

Once the two proton beams have reached the maximum energy, they collide in four different sites along the ring, where the four main experiments, Figure 2.3, are situated:

- **A Toroidal LHC ApparatuS (ATLAS)**: a general-multipurpose detector, which investigates a wide range of physics from the Higgs boson to extra dimensions and dark matter.
- **Compact Muon Solenoid (CMS)**: a general-multipurpose detector. It has the same scientific goals as the ATLAS experiment, but uses different technical solutions and a different magnet-system design.
- **A Large Ion Collider Experiment (ALICE)**: a detector built to study the physics of strongly interacting matter at extreme energy densities, quark-gluon plasma state, produced by heavy ion collisions.
- **Large Hadron Collider beauty (LHCb)**: the only detector that detects mainly forward particles produced by pp-collisions. It is focused in investigating the differences between matter and antimatter studying the quark beauty physics. It aims to perform precision measurements about the flavour physics and CP violation, especially involving B mesons.

All the LHC detectors must uniform to very challenging experimental requirements due to the complexity of the data taking and analysis associated to events produced, in order to perform event reconstruction and measurement with high accuracy.
On average every 25 ns, 36 interactions per bunch crossing take place, called *pile-up events*. In addition, for each pp-collision there is a non-null probability of multiple interactions due to multiple inelastic scatterings of proton constituents (i.e *partons*). These latter events are referred to as *underlying events*(UE). Furthermore we have to consider also the initial (ISR) and final state (FSR) gluon radiation.
The whole set of particles populating the detector material can overwhelm the signature of processes with very low cross-sections, or the ones of NP phenomena. Hence, to efficiently reconstruct the event of interest and to discriminate it from ISR, FSR, underlying and pile-up events, detectors are built to satisfy the following requirements:

- high granularity to cope with the particle fluxes and to separate overlapping events;
- fast, radiation hard electronics and sensor elements;
- large spatial coverage, ideally 4π coverage;
- good charged particles momentum resolution and reconstruction efficiency in the inner detector. Vertex detectors placed near the interaction point are also required to observe secondary vertex;
- very good calorimetry to identify electrons and photons (in the electromagnetic calorimeter) as well as to measure jets and missing energy (int the hadronic calorimeter);

- good muon identification and momentum resolution in a wide range of momentum values;
- high low transverse momentum objects rejection;
- high trigger efficiency.

2.2 The ATLAS Experiment

ATLAS [38] is a multi-purpose detector located ad Point 1 of the CERN LHC facility. It is designed to exploit the full discovery potential of the LHC from the Higgs sector to physics beyond Standard Model. ATLAS also contributes to high precision measurements of the Standard Model (QCD and electroweak interactions). Therefore, ATLAS has to cope well with a broad variety of possible physics processes and signatures.

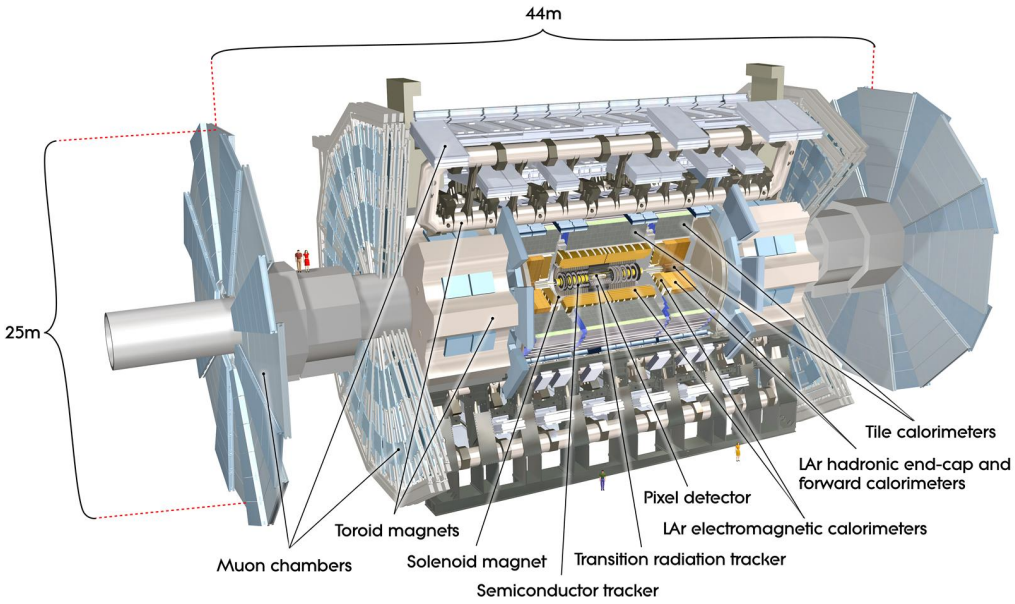

Figure 2.4: Schematic representation of the ATLAS detector at LHC.

ATLAS has a cylindrical symmetry, it is 44 meters long with a diameter of 25 meters and a weight of 7000 tons. The ATLAS detector layout is depicted in Figure 2.4. It is composed of different sub-detectors placed concentrically around the interaction point (IP) to identify particles as well as performing precise measurement of energy, momentum and trajectories of the multiple objects produced in pp-collisions. Starting from the IP the sub-detectors are:

- Tracking system (pixel, strips and transition radiation detectors).
- Electromagnetic (ECAL) and Hadronic (HCAL) calorimeters.
- Muon spectrometer.
- Magnetic system.

The structure contains also an inner solenoid, an outer toroidal magnetic field and trigger, readout, DAQ. An important addition to the list of sub-detectors above should be done concerning the *Forward Detectors* used to provide a good coverage in the forward region.

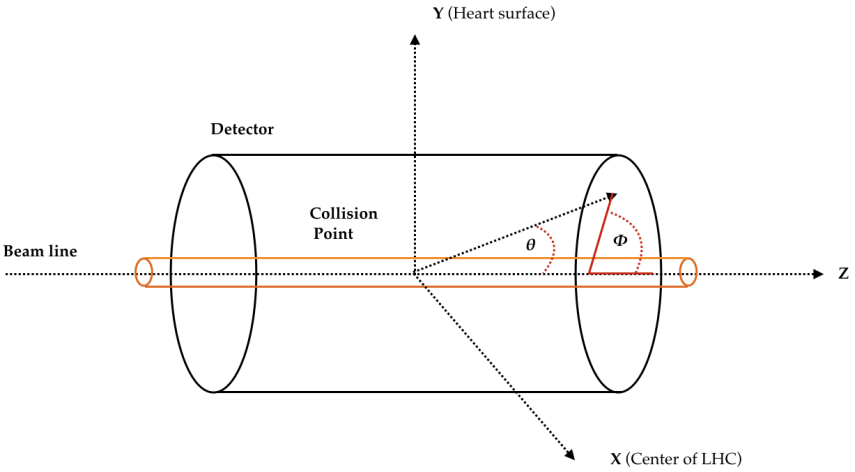

Figure 2.5: ATLAS detector coordinate system.

ATLAS uses a right-handed coordinate system, where the IP is defined as the origin, and the z-axis is tangent to the beam line. The $x-y$ plane is *transverse* to the beam direction: the x-axis points twoards the center of the LHC ring, the y-axis points upwards. Due to the cylindrical symmetry, polar coordinates (r, ϕ) are used in the transverse plane (Figure 2.5), the azimuthal angle $\phi \in [-\pi, +\pi]$ is measured around the beam axis and the polar angle $\theta \in [0, +\pi]$ is measured from the beam axis.
Most used variables are:

- The **transverse momentum** $p_T = \vec{p}sin\theta$. Particles with $p_T \approx 0$ are out of acceptance and escape along the beam pipe and are said "invisible". The "visible p_T is conserved: $\sum_i p_{t,i} \approx 0$. One has to notice that both $\vec{p}$ and θ are not Lorentz invariant along z.

- The **rapidity** y, defined as:

$$\vec{y} = \frac{1}{2} ln \left(\frac{E + p_z}{E - p_z} \right) = \frac{1}{2} ln \left(\frac{1 + \beta cos\theta}{1 - \beta cos\theta} \right). \tag{2.5}$$

- The **pseudo-rapidity** η, defined for $\beta \to 1 (m \ll p_t)$:

$$\eta = -ln \left(tan \frac{\theta}{2} \right). \tag{2.6}$$

  used to express the relative angle between a particle and the beam axis and to indicate the detector coverage. Its value is zero for particle trajectories perpendicular to the beam ($\theta = 90°$), and when the polar angle approached zero, pseudo-rapidity approaches infinity. Hard interactions with high momentum transfer produce particles at small η far off the beam pipe direction.

- The **angular distance** ΔR between two particles

$$\Delta R = \sqrt{\Delta\eta^2 + \Delta\phi^2} \tag{2.7}$$

  where $\Delta\eta$ and $\Delta\phi$ are differences in pseudo-rapidity and azimuthal angle, and are invariant for Lorentz boosts along z-axis.

In Table 2.2 the general performance goals for the ATLAS detector are shown.

Detector component	**Required resolution**	η coverage	
		Measurement	Trigger
Tracking	$\sigma_{p_T}/p_T = 0.05\% p_T \oplus 1\%$	± 2.5	
EM calorimetry	$\sigma_E/E = 10\%/\sqrt{E} \oplus 0.7\%$	± 3.2	± 2.5
HAD calorimetry			
barrel and end-cap	$\sigma_E/E = 50\%/\sqrt{E} \oplus 3\%$	± 3.2	± 3.2
forward	$\sigma_E/E = 100\%/\sqrt{E} \oplus 10\%$	$3.1 < \lvert\eta\rvert < 4.9$	$3.1 < \lvert\eta\rvert < 4.9$
Muon spectrometer	$\sigma_{p_T}/p_T = 10\% \text{at} p_T = 1\text{TeV}$	± 2.7	± 2.4

Table 2.2: General performance goals [38] of the ATLAS detector: the required resolution and the η coverage for measurement and trigger.

2.2.1 The ATLAS Magnetic System

This system [39] is necessary to bend the charged particles where the minimum detectable bending is constrained by the precision of the tracking system also its value is limited by the perturbation of the particle trajectory following the interaction with the detector

material. Thanks to its effect on particles trajectories it is possible to perform momentum measurements in the Inner Detector and in the Muon Spectrometer as well. The ATLAS Magnetic System consists of four superconducting magnets: one solenoid an three toroids. The dimensions of the system are 22m in diameter and 26m in length:

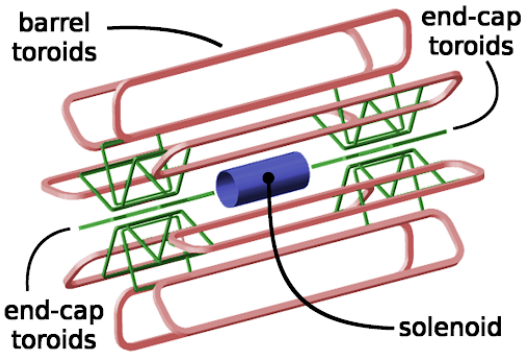

Figure 2.6: Schematic view of the ATLAS detector magnetic system: the central solenoid (blue), 8 barrel toroid coils (red) and 2×8 coils (green) of the end-cap toroids.

- the **Central Solenoid (CS)** is a cylinder aligned on the beam axis around the IP placed behind the Inner Detector providing a 2T axial magnetic field for the inner tracking system and is build to minimize the radiative thickness in front of the barrel electromagnetic calorimeter. The Central Solenoid consists of a single layer Al-stabilised NbTi conductor coil placed inside a 12 mm thick support cylinder. It is 5.8 m long and has a inner and outer radius of 2.46 m and 2.56 m respectively.
- the **Barrel Toroid (BT)** and two **End-Cap Toroids (ECT)** provide a 0.5 T and 1 T magnetic fields respectively for the outer muon spectrometer system. All the toroids are made of Al-stabilised Nb/Ti/Cu conductor coils. The barrel toroid is 25.3 m long and has an inner and outer radius of 9.4 m and 20.1 m respectively. It consists of eight coils enclosed in separated vacuum vessels, while each one of the two end-cap toroids is made of eight square coils glued together with eight wedges into a rigid structure.

All the magnets operate at a temperature of 4.8 K obtained through a liquid helium cryogenic system.

2.2.2 The Inner Detector

It is the innermost part of the ATLAS detector. The main goal of the Inner Detector (ID) [40] is to provide reliable and accurate tracking of charged particles as well as primary and secondary vertex reconstruction, and momentum measurement near the IP.

The ID has cylindrical symmetry, and outer radius of 1.05 m with a overall momentum resolution in the rapidity interval $|\eta| < 2.5$ of $\sigma_{pT}/p_T = 0.05\% p_T \oplus 1\%$.
The detector is composed of three complementary sub-systems, Figure **??**: the **Pixel Detector** (PD), providing 3-dimensional space points, the **Semi-Conductor Tracker** (SCT) and the **Transition Radiation Tracker** (TRT). All the sub-detectors are contained in a cylidrical envelope of radius $r = 1150$mm and length $l = \pm 3512$mm in the barrel region, surrounded by a solenoid generating a 2 T magnetic field.

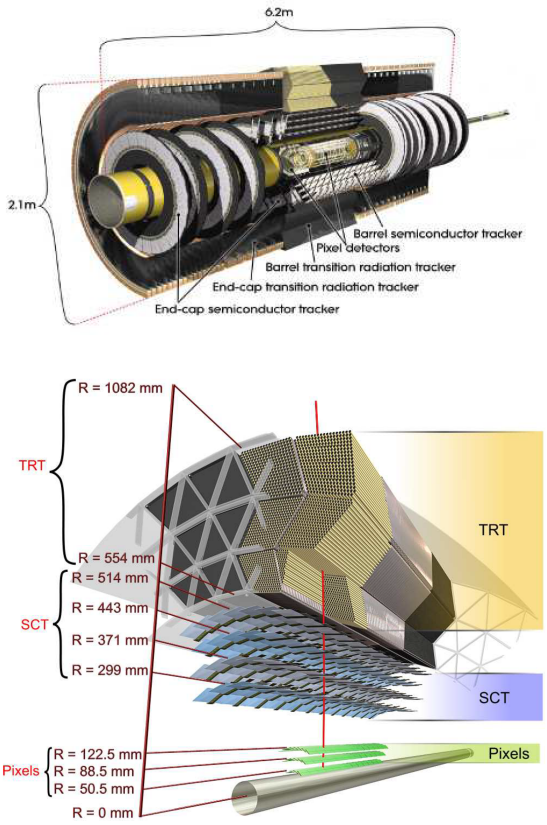

Figure 2.7: Illustration of the ATLAS barrel Inner Detector: Pixels, SCT and TRT components are shown.

- The *Pixel Detector* forms the innermost part of the ID. It has 1744 identical modules, arranged in three barrel layers and two end-caps each with three disk layers. Every module contains more silicon pixels, that have a size of 50×400 μm^2 each in the $r\phi$ plane and z-axis respectively. The PD has more than 80 millions of readout channels. Pixels modules are tilted by 20° with respect to the barrel tangent, its intrinsic spatial resolution is 10 μm in $r\phi$ plane and 115 μm in z and operate at

a temperature of -10° C. It improves the impact parameter reconstruction and vertexing.

- The *Semi-Conductor Tracker* is essential for the precise momentum measurement. The SCT is located outside the PD and consists of 4088 modules of silicon-strip detectors organized in four coaxial cylinders in the barrel and in two end-caps with nine disk layers each. Strips modules are tilted by $\sim 11^{\circ}$ with respect to the barrel tangent in the opposite direction to the pixel modules. The SCT has more than 6.3 millions of readout channels and provides 8 measurements per track with resolution of 16μm in $r\phi$ plane and 580 μm in z.

- The *Transition Radiation Tracker* forms the outermost part of the ID and extends track reconstruction radially up to a radius of 1082 mm providing more than 30 hits per track. It also uses the emission of transition radiation photons caused mainly by electrons and positrons to perform particle identification as well as to discriminate $e^{\pm}$ from π mesons. The TRT is built with 4 mm diameter straw tubes contained in modules placed in three coaxial cylinders in the barrel. Each TRT cylinder counts 32 modules. The straw tubes are proportional counters filled with 70% Xe, 27% CO_2, 3%O_2 gas mixture with a 5 to 10 mbar over-pressure, long 144 cm in the barrel and placed parallel with respect to the z axis. The TRT has 3.5 million readout channels and a spatial accuracy of 1301 μm. Tracks above a given p_T threshold are reconstructed offline within the full acceptance range $|\eta| < 2.5$ of the whole Inner Detector, using multi-stage track identification algorithms.

2.2.3 The ATLAS Calorimeters

After particles travel through the Inner Detector, they arrive to the ATLAS calorimeters where precise measurements of electrons, photons and jets (reconstruction and missing transverse energy E_T^{miss}) are performed. The electromagnetic calorimeter is divided into a barrel part and two end-cap components while the hadronic calorimeter is composed by tile, end-cap and forward calorimeters regions, Figure 2.8. The whole calorimetric system has a coverage of $|\eta| < 4.9$ in order to measure transverse energy accurately and to minimize the presence of uninstrumented regions. One of the challenging aspects of calorimetry concerns the containment of electromagnetic and hadronic showers, here the parameter of interest is the calorimeter *depth*. The calorimetric system is constructed as follows:

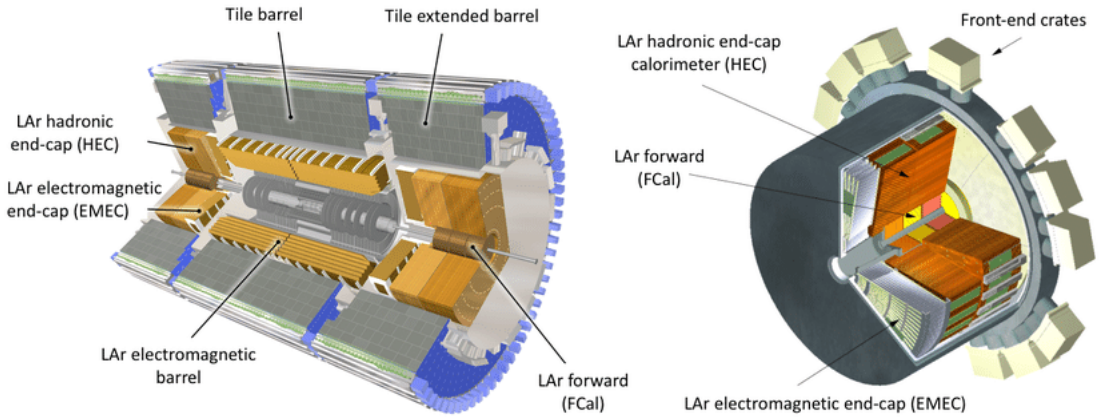

Figure 2.8: Schematic view of the ATLAS calorimeter subsystems (left) and an enlarged view of the end-cap calorimeters (right). EM calorimeter is divided into a barrel part and two end-caps components. HAD calorimeter is composed by tile, end-cap and forward calorimeter regions.

- The sampling Electromagnetic Calorimeter is made of lead absorbing plates as passive medium (due to their large electromagnetic cross-section) and liquid-argon (LAr) as active material. Lead-LAr layers are organized in an accordion-shape which allows a complete azimuthal symmetry of the detector without any crack. The fine-granularity EM calorimeter is divided into a barrel ($|\eta| < 1.475$) and two endcaps ($1.375 < |\eta| < 3.2$), matching the η region of the Inner Detector. The total thickness of the EM calorimeter is more than 22 X_0 (radiation lengths) in the barrel and larger than 26 X_0 in the end-caps.
  The barrel EM calorimeter is composed by two independent coaxial wheels separated by a 4 mm gap at $z = 0$. The outer wheel covers the region $1.375 < |\eta| < 2.5$ and the inner one $2.5 < |\eta| < 3.2$. Since the region devoted to precision physics requires the objects (electrons, muons, jets) to be within the $|\eta| < 2.5$ of the ATLAS detector, the EM calorimeter is further segmented into three longitudinal sections to provide a higher granularity: the first is called *pre-shower* section providing particle identification and high precision angular measurement; the section in the middle measures the released energy while the last one measures the energy of particles which escaped from the central section.

- The Hadronic Calorimeter is also a sampling calorimeter. Among its tasks (containment for hadronic showers, measuring of hadron energy and missin transverse energy) plays an important role avoiding the strong-interacting particles to reach the muon system. In this case the *interaction length* $\lambda \sim 35A^{1/3}$g cm^{-}2 (the mean free path between interactions) describes the hadronic calorimeter. The ATLAS

hadronic calorimeter cover the range $|\eta| < 4.9$ with a total thickness of 11 λ at $\eta = 0$ and is composed by:

1. the **Hadronic Tile Calorimeter (HTC)** is installed right outside the electromagnetic calorimeter envelope and consists of a barrel that covers the $|\eta| < 1.0$ region and two extended barrels covering the range $0.8 < |\eta| < 1.7$ azimuthally divided in 64 wedge-shaped modules each. It is a sampling calorimeter using steel as absorber and scintillating tiles as active material. The tile calorimeter is contained in a radius range of 2.28 m $< r_{tile} <$ 4.25 m and it is segmented into three layers in depth of about 1.5, 4.1 and 1.8 λ for the barrel and 1.5, 2.6 and is 9.7 λ at $\eta = 0$.
2. the **Hadronic End-cap Calorimeter (HEC)** covers the range $1.5 < |\eta| < 3.2$ and consists of two wheels per end-cap located behing the EM calorimeter. It uses both steel and LAr and its purpose is to reduce the transition between the end-cap and the forward calorimeter by overlapping the pseudo-rapidity region $|\eta| = 3.1$ covered by the latter. It also overlaps the tile calorimeter $|\eta| < 1.7$ by extending to $|\eta| = 1.5$. The two wheel are composed by 32 azimuthal wedges and 2 segments in depth each.
3. the **Forward Calorimeter (FCal)** is the nearest component to the beam pipe composed by three modules per end-cap with a coverage of $3.1 < |\eta| < 4.9$ and total depth of ~ 10 λ. The first module, in copper, is for electromagnetic measurements, while the other two in tungsten in order to contain hadronic showers.

2.2.4 The Muon Spectrometer

Particles that travel through the full depth of calorimeters are either non- or weakly-interacting particles such as neutrinos, or minimum ionizing particles (MIP) as muons losing only few MeV/mm through their electromagnetic interactions with the calorimeters. For this reason the Muon Spectrometer (MS) [41] constitutes the outer part of the ATLAS detector with the purpose to measure muon momentum with high resolution ($2-3\%$ at $10-100$ GeV/c and 10% at 1 TeV muon tracks) as well as to work as trigger for muons. The momentum measurement is made possible thanks to magnetic field, generated by the superconductive air-core toroid magnets in both barrel and end-cap regions, perpendicular to the beam. The magnetic field bends the muons trajectory allowing an independent measurement of their momentum with respect to the one provided by the ID. The muon spectrometer, with an outer diameter of 24 m and 44 m length, is composed by four complementary sub-systems: two *trigger chambers* in the barrel and two *precision chambers* in the end-caps as shown in Figure 2.9.

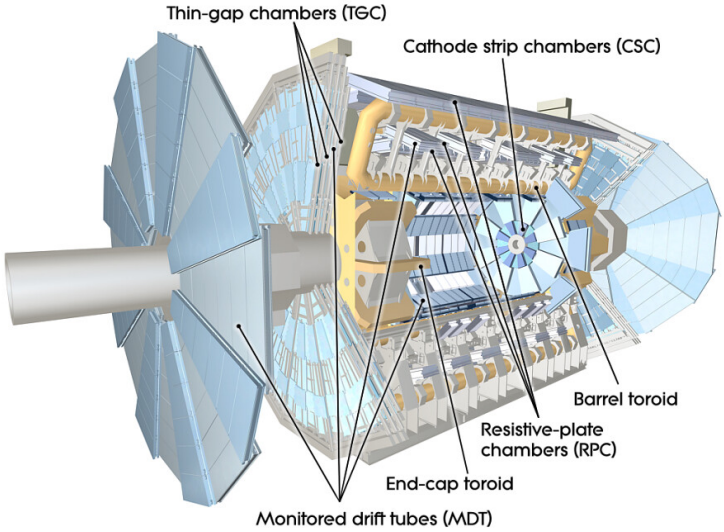

Figure 2.9: View of the ATLAS muon spectrometer and its components: monitored drift tubes (MDTs), cathode strip chambers (CBS), resistive plate chambers (RPCs) and thin gap chambers (TGCs).

- In the barrel region the chambers are arranged in three cylindrical (concentric) layers around the beam axis. The **Trigger Chambers** are fast detectors for muon measurement consisting of *Resistive Plate Chambers (RPC)*, covering the range $|\eta| < 1.05$, and *Thin Gap Chambers (TGC)* covering $1.05 < |\eta| < 2.4$. The Resistive Plate Chambers are employed as the trigger system in the barrel. The parallel elctrode-plate chambers are filled with a gas mixture of 97% tetrafloroethane ($C_2H_2F_4$) and 3% isobutane (C_4H_{10}). Muons traversing the chamber produce primary ionization electrons which are multiplied into avalanches by a 4.5 kV/mm electric field, this allows really fast signals with result in a time resolution of $\sim$ 2ns. The detecting units are three rectangular layers, two placed in the middle and one in the outer barrel stations, read out by two orthogonal series of pick-up strips, providing information on both the η and ϕ coordinates. The Thin Gap Chambers are the trigger system in the end-cap regions and also used for the track coordinate measurements in the transverse plane to complement the Monitored Drift Tubes measurements. The TGC are multiwire chambers filled with highly quenching gas mixture of 55% CO_2 and 45% n-pentane ($n-C_5H_{12}$) operating in saturation mode. The anode-cathode spacing is smaller than the anode-anode spacing allowing very short drift time, less than 20 ns. The spatial resolution of th TGC is 4 mm in the radial direction and 5 mm in the ϕ coordinate.

- In the transition and end-cap regions the chambers are installed in planes per-

pendicular to the beam, always in three layers. The **Precision Chambers** are composed by the *Monitored Drift Tubes (MDT)* covering the $|\eta| < 2.7$ region, and *Cathode Strip Chambers (CSC)* covering the $2 < |\eta| < 2.7$ range. Precision Chambers perform the muons trajectory reconstruction. The MDTs are drift chambers of two multilayer drift tubes, with diameter of 30 mm and aluminum walls filled with Ar/CO_2 gas at 3 bar. The electrons produced by ionization are collected on a 50μm diameter anode wire at a potential of 3080 V. The MDTs have a long drift time (700 ns) but a track resolution of 35μm per chamber allowing to return precise measurements of the z coordinate in the barrel region and in the end-cap region. The CSC substitute the MDT in the innermost end-cap layer to cope with the higher particle rate due to proximity to the IP. The CSC are multi-wire proportional chambers with strip cathodes and filled with Ar/CO_2 measuring muon momentum. The cathode planes are segmented, one plane in strips parallel to the wires in radial direction, while the strips on the other plane are orthogonal to the wires. This configuration allows CSC to measure both the coordinates with track resolutions, per chamber, of 40μm in the bending plane and 5 mm in the transverse plane.

2.2.5 Trigger and Data Acquisition System

The amount of data produced at LHC over $\sim 10^9$ proton-proton collisions in ATLAS is impressive. For each event around 1 MB of data are collected:

$$10^9 \text{ collisions/s} \times 1 \text{ Mbyte/collision} = 10^{15} \text{ bytes/s} = 1 \text{ PB/s}$$

this represent a challenge being several orders of magnitude greater than what any detector DAQ can handle. The ATLAS **TDAQ** (*Trigger and Data Acquisition*) system [42] manages the online event selection and storage for the data to be then analyzed offline, in this way the information rate is reduced from 40 MHz to 100 Hz. This process is done in two steps consisting of a hardware Level-1 (L1) and a software-based high-level trigger (HLT). In Figure 2.10 one can see a block diagram of the ATLAS TDAQ where the L1 and HLT are shown together with the detector read-out and data flow.

- **L1 Trigger**, an hardware-based system, collects the reduced-granularity information from the calorimeter and muon detectors, providing information about transverse energy, missing energy and particle transverse momentum. The *L1 Calo* has as input the signal from the calorimeter detectors and gives the information about clusters with energy above a given threshold, transverse energy, missing transverse energy and τ-like objects; the *L1 Muon* works on information from RPCs in the barrel and TGCs in the end-caps, such as p_T.
  The topological processor, *L1 Topo* added in Run 2, determines variables such as angular distances between objects or the invariant mass of pairs of objects.

All these information are eventually transmitted to the *Central Trigger Processor (CTP)*. Once the input signals have been elaborated by the CTP, the L1 trigger decision is delivered. This way the event rate is reduced by the L1 trigger from 40 MHz to 100 kHz.

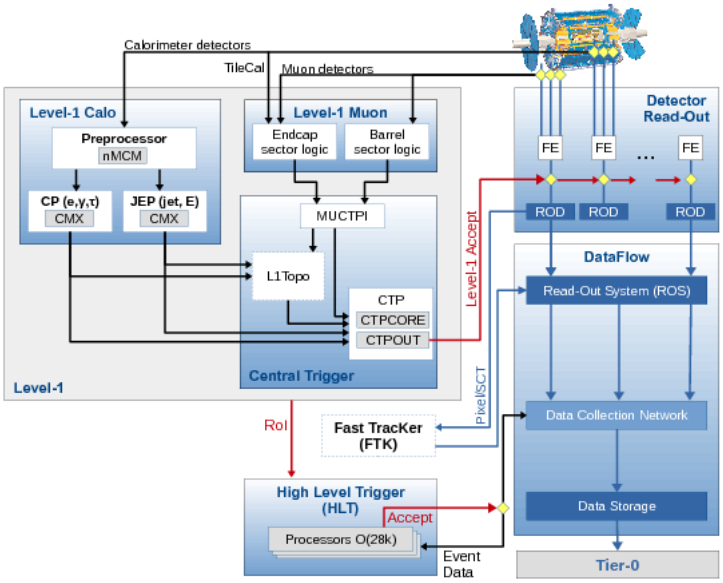

Figure 2.10: The ATLAS TDAQ system in Run 2.

- The **HLT** is software-based (for the most part on the offline software *Athena*) and it is composed by several sub-systems. For each event that passed the L1 trigger selection, the *Front-End (FE)* detector electronics reads out the event data for all detectors: now the information is sent to the *ReadOut Drivers (RODs)* to be processed and then to the *ReadOut System (ROS)* for the data buffering. After that the information is selected and combined by the *Region of Interest Builder (RoIB)*. Finally to the *HLT Supervisor* that organizes events into clusters. refines the decisions of the L1 trigger and it is composed by several sub-systems. Information from L1 trigger is read and combined by the Region of Interest Builder (RoIB) and then passed to the HLT Supervisor, that organizes events into clusers. The input/output data are scheduled by the *Data Collection Manager* and set to the HLT nodes. The output rate of the HLT during an ATLAS data-taking run is on average 12 kHz with an average physics throughput to permanent storage of 1.2 GB/s. The events that manage to pass the L1 and HLT selection are sent to the *Sub-Farm Output (SFO)* from where they are distributed to the permanent for offline reconstruction and exports the data to the *Tier-0* facility at CERN computing center.

Chapter 3

Objects reconstruction

In this chapter the process of objects reconstruction in ATLAS is presented. As first step in the analysis procedure, it covers the reconstruction and identification of particles produced after the proton-proton collision in the detector. Typically, the objects of interest defined by a physics analysis are electrons, muons, tau leptons, jets and missing transverse energy. Their definition is further optimized in the analysis context using selections that maximize the sensitivity. The particle selection efficiencies are determined using both simulated Monte Carlo (MC) samples and data collected by the detector. The computed efficiencies are then applied to the data samples used in the analysis. The total efficiency for the charged leptons reconstruction is:

$$\epsilon_{tot} = \epsilon_{reco} \cdot \epsilon_{ID} \cdot \epsilon_{iso} \cdot \epsilon_{trig} \tag{3.1}$$

where ϵ_{reco} is the *reconstruction efficiency*, ϵ_{ID} the *identification efficiency*, ϵ_{iso} the *isolation efficiency* and ϵ_{trig} the *trigger efficiency*. Another quantity to consider is the *Scale Factor* (SF). This is a correction factor applied to the simulated samples since the efficiencies in the MC events must be corrected to match those measured from the data:

$$\text{SF} = \frac{\epsilon_{data}}{\epsilon_{MC}} \tag{3.2}$$

where ϵ_{data} is the efficiency measured from the data while ϵ_{MC} the one obtained from the MC events.

3.1 Electron reconstruction

Along their path inside the detector, Figure 3.1, the electrons leave tracks in the ID and are absorbed, for the most part, within the electromagnetic calorimeter. The electron candidates are reconstructed [43], in the precision region of the ATLAS detector ($|\eta| < 2.7$), considering three features: the presence of localised clusters of energy deposit in the

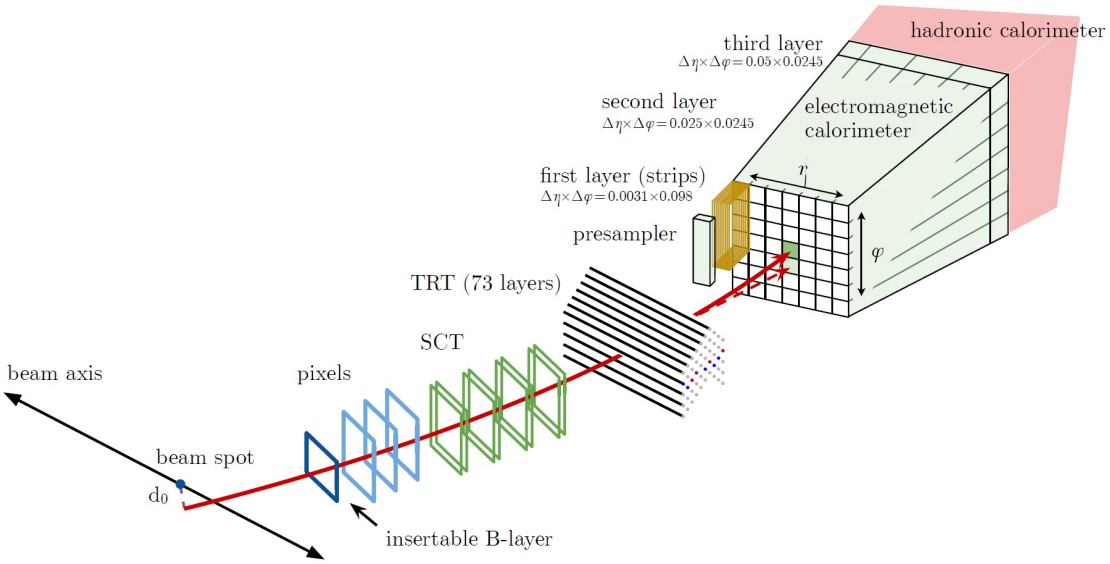

Figure 3.1: Illustration of the electron path (red solid line) inside the ATLAS detector. It is also shown (red dashed line) a photon produced by the interaction of the electron with the material in the tracking system.

electromagnetic calorimeter, the identification of tracks associated to a charged particle (ID), and the matching in space between tracks and energy deposits. The reconstruction for electrons does not consider the transition region $1.37 < |\eta| < 1.52$ between the barrel and endcap calorimeters, since the relatively poor background rejection. The EM calorimeter is subdivided, in the (η, ϕ) space, in 200×256 elements with granularity $\Delta\eta^{tower} \times \Delta\phi^{tower} \cong 0.025 \times 0.025$. The energy correspondent to each element, called *tower*, is the sum of the energy deposited in the first, second and third calorimeter element layers. To reconstruct the energy a *seed-cluster* algorithm [44] searches for electron cluster "seeds" as longitudinal towers with total cluster transverse energy above 2.5 GeV. Electromagnetic energy cluster candidates are then formed around the seeds using a clustering algorithm which removes duplicates and allows their reconstruction with an efficiency that depends both on $|\eta|$ and transverse energy E_T (see the red triangles distribution in Figure 3.2 on the left). The reconstruction efficiency is evaluated from the simulation of $Z \to ee$, $J/\psi \to ee$ events and ranges from 65% at $E_T = 4.5$ GeV to 96% at $E_T = 7$ GeV, to more than 99% at $E_T > 15$ GeV.
The track information form the Inner Detector is extracted using pattern recognition and ambiguity resolution [45]. The energy loss, due to particles interacting with the detector, is modelled by the pattern recognition algorithm using the pion hypothesis. Track candidates with $p_T > 400$ MeV are fitted using the ATLAS Global χ^2 Track Fitter [46] resolving the ambiguities associated to tracks. This track fitting procedure

has a reconstruction efficiency ranging from 80% at $E_T = 1$ GeV to more than 98% at $E_T > 10$ GeV (see the blue open circles distribution in Figure 3.2 on the left) . Finally, the electron is reconstructed if both the track and calorimeter cluster candidates match together. The total reconstruction efficiency, above $E_T = 15$ GeV, varies from 97% to 99% (graph on the right of Figure 3.2) for an electron with at least one hit in the pixel detector and at least seven silicon hits.

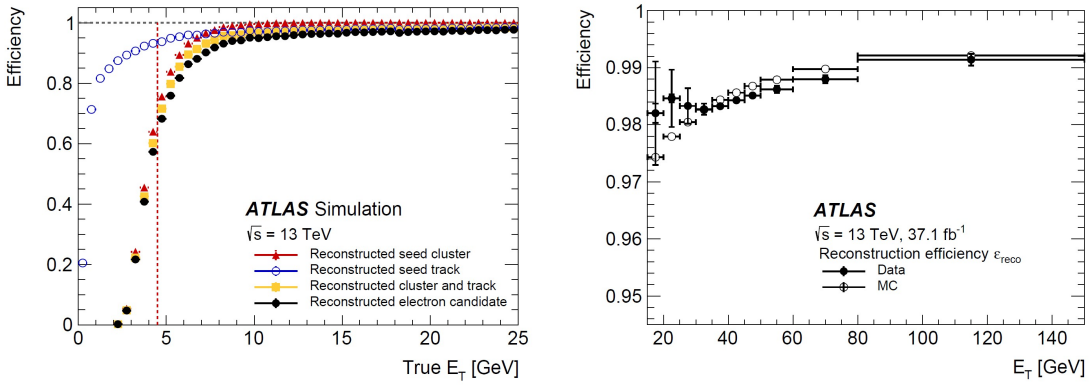

Figure 3.2: On the left: the total reconstruction efficiency for simulated electrons at $\sqrt{s} = 13$ TeV is shown as function of the transverse energy E_T; signal produced in the calorimeter is used. On the right: the reconstruction efficiency at $\sqrt{s} = 13$ TeV is plotted as function of the transverse energy. In the graph, data (black circles) are compared with MC simulation (open circles). Signal produced in the tracking system is used [43].

3.1.1 Electron identification

To identify electrons within the $|\eta| < 2.47$ region a *likelihood-based identification* (LH) is used. Several observables (track properties, calorimeter shower shapes, variables measuring bremmsstrahlung effects, etc.) are relevant in the electron identification process. The LH is defined as the product of n probability density functions (pdfs) which are based on simulated events both for signal and background:

$$L_{S(B)}(\vec{x}) = \prod_{i=1}^{n} P_{S(B),i}(x_i) \tag{3.3}$$

where $\vec{x}$ are n-component input vectors (i.e. the set of discriminating variables), $P_{S,i}(x_i)$ is the value of the signal pdf of the i^{th} variable evaluated at x_i, likewise for the background pdf $P_{B,i}(x_i)$, $L_{S(B)}(\vec{x})$ are the likelihood function for signal electrons (prompt, coming from the IP) and background mainly from photon conversions and heavy flavour

hadron decays. For each electron candidate these probabilities (3.3) are combined into a discriminant:

$$d_L = \frac{L_S}{L_S + L_B}. \tag{3.4}$$

This discriminant shows a sharp peak at unity for signal electrons and at zero for background.

Four fixed values of the LH discriminant are used, in order to define four *working points* corresponding to increasing thresholds for the LH discriminant, that are: *VeryLoose, Loose, Medium* and *Tight*. The electron candidate in order to be classified as Loose, Medium or Tight, it is required to have at least two hits in the pixel detector and seven hits total in the pixel and silicon strip detectors combined. For Medium and Tight at least one of the hits must be in the innermost pixel detector layer. The VeryLoose provides identification requirements for background studies and calls for only one hit in the pixel detector with no further constrain on the innermost pixel layer.

The identification efficiencies for a $E_T = 40$ GeV prompt electron are 93%, 88% and 80% for Loose, Medium and Tight operating points, respectively. The efficiencies depend on both $|\eta|$ and E_T, in Figure 3.3 the efficiencies for data and data-to-simulation ratios are shown. A large statistical sample of $Z \to ee$ and $J/\psi \to ee$ decays is employed to measure the identification efficiencies for electrons using a tag and probe technique.

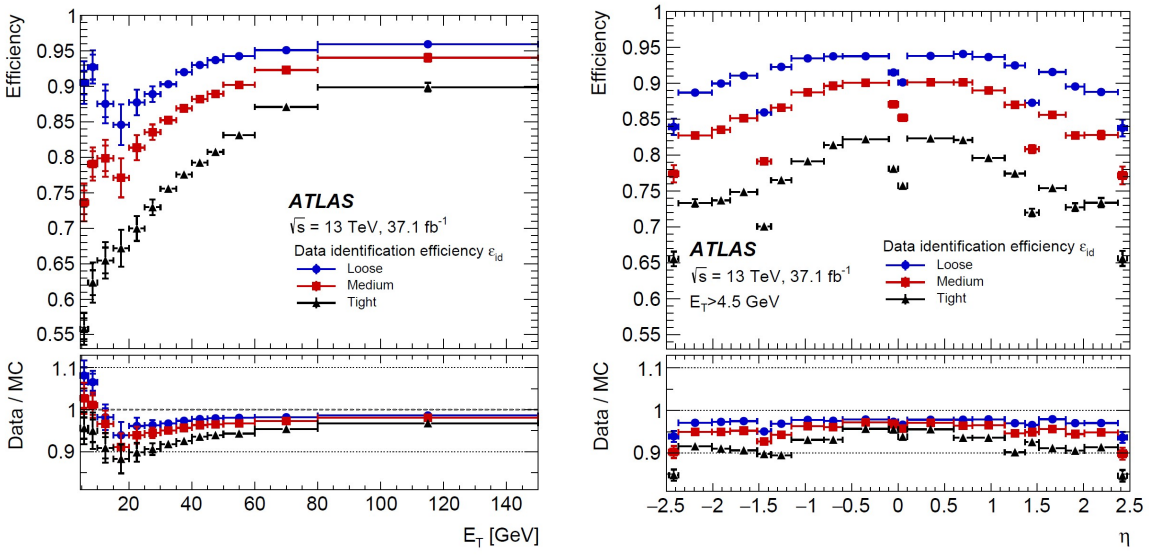

Figure 3.3: Both plots show the measured electron identification efficiencies [43] for Loose (blue circles), Medium (red squares) and Tight (black triangles) operating points as functions of the transverse energy E_T on the left and of the pseudorapidity η in the right. In the bottom part of both graphs the data to simulation ratio is shown.

3.1.2 Electron isolation

The isolation process aims to clean up the reconstructed object (prompt electrons) in signal processes from background ones. The signal is characterised by little activity in a $(\Delta\eta, \Delta\phi)$ area surrounding the candidate, both in the tracker and in the calorimeter. On the other hand, the activity around the background electrons is higher due to the larger energy deposit in tracker and calorimeter. The activity close to the candidate object is quantified by the isolation variable defined from the sum of the energy deposits in the calorimeter or the sum of the transverse momenta of tracks in the inner detector in a cone of radius ΔR around the direction of the electron candidate:

$$\Delta R = \min\left(\frac{10\text{ GeV}}{p_T}, R_{\text{max}}\right) \tag{3.5}$$

where R_{max} varies from 0.2 or 0.4. Isolation variables are of two types:

- **Calorimeter-based isolation**: uses the sum of the E_T of topological clusters (from EMCAL and HADCAL) within a cone aligned with the electron direction, Figure 3.4. A disadvantage of this method is that the candidate object may deposit energy outside of this fixed rectangular area which may be incorrectly assigned as additional activity.

- **Track-based isolation**: here the isolation variables are derived from tracks with $p_T > 1$ GeV reconstructed within $|\eta| < 2.5$ inside the ID also satisfying track-quality requirements. This track selection includes a minimum number of hits identified in the silicon detectors and a maximum number of inoperable detector regions crossed by the track. The pile-up contribution is reduced requiring a cut $|z_0 \sin\theta| < 3$ mm on the longitudinal impact parameter z_0. In this way one aims to select tracks that originate form the vertex. Some track-based isolation variables are computed by defining a cone of radius ΔR, aligned with the electron track, and summing the transverse momenta of the tracks found within it, excluding the candidate's own contribution. Then the track-p_T contribution of the candidate electron to the track-isolation variable must be subtracted from the cone. The resulting track-isolation variable is called p_T^{isol}.

3.1.3 Electron triggers

At the HLT stage, the electron reconstruction employs each Region of Interest (RoI) defined in the EM calorimeter, at the L1 stage, which satisfy E_T and isolation requirements as specified by the trigger menu [47]. The HLT fast algorithms are executed first allowing the precision algorithm to run at a reduced rate later in the trigger sequence. Both the calorimeter and ID information within the RoI are used to perform the initial

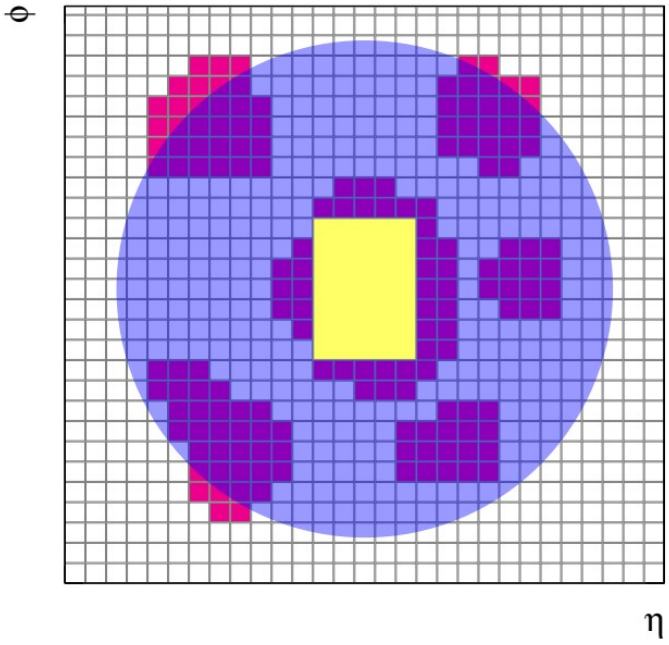

Figure 3.4: Graphic representation of the calorimeter isolation method. The grid represents the second-layer calorimeter cells in the η and ϕ directions. The purple circle is the isolation cone and in its center the electron candidate can be found. In red are shown all the topological clusters. The yellow rectangle corresponds to the subtracted cells in the core subtraction method.

selection and identification of the electron candidates, making possible an early background rejection.
HLT precision algorithm are executed only if the fast selection criteria are fulfilled in order to access, if it is possible, detector information outside the RoI. Then, the two main trigger selections are defined:

- **The L1 trigger** for electron builds the EM RoI starting from the calorimeter information in the central region $|\eta| < 2.5$. The algorithm chooses, within $|\eta| < 2.5$, the maximum E_T value from the four possible pairs of the nearest-neighbour EM towers in a 2×2 central region. Also a nominal E_T threshold and optionally a selection to reject hadronic activity below 50 GeV can be applied. Finally an EM isolation requirement is applied: the candidate electrons are rejected if the sum of E_T in the 12 towers surrounding the 2×2 central region in the EM layer is at least 2 GeV and exceeds the value $E_T/8.0 - 1.8$ GeV.

- **The HLT electron reconstruction** consists of two successive steps, the fast and the precision one. The former step (fast calorimeter reconstruction and selec-

tion) has two implementations: a cut-based algorithm and a neural network based *Ringer* algorithm. Electrons with $E_T < 15$ GeV are selected with the cut-based algorithm while the latter is used for triggering electrons with $E_T > 15$ GeV. Electron candidates are required to have tracks from the fast track reconstruction step, performed inside the RoI only, matching the corresponding cluster. In the precision calorimeter reconstruction step, precision tracks with the RoI are extrapolated to the second layer of the EM calorimeter and are required to match the clusters within $|\Delta\eta(track, cluser)| < 0.05$ and $|\Delta\phi(track, cluster)| < 0.05$ rad.

3.2 Muon reconstruction

The reconstruction process for muons [48] consists of two separate steps performed in the Inner Detector and in the Muon Spectrometer (MS). The resulting information is then combined to form the final muon track candidate, used for the analysis. The reconstruction algorithm, used in the MS, starts with a search for hit patterns inside different chambers aiming to form segments. MDT segments results from a straight-line fit with the hits found in each layer (a Hough transform [49]) while RPC and TGC hits are used to measure the coordinate of the muon track orthogonal to the bending plane. Differently, to build the segments in the CSC detectors a separate combinatorial search in the η and ϕ detector planes. The tracks are then built by fitting together hits from segments in the MS layers, at least two matching segments are required. Then a global χ^2 fit on the hits associated with each track candidate is performed. Finally, the information from both ID and MS tracks are joint to carry out a ID-MS combined reconstruction. To build the final reconstructed candidates there are four muon types, depending which subdetectors are used in the reconstruction:

- **Combined muons (CB)**: the track reconstruction is realised independently in the ID and MS, then a global fit is performed in order to built a combined track. The fit result can be improved by adding or removing MS hits from the final track. The extrapolation flow follows an inward direction starting from the MS (the outer part of the detector) to the ID. This measurement is complemented by the same procedure but starting from the ID proceeding outward.

- **Segment-tagged muons (ST)**: here the ID track is classified as muon if it is associated with at least one track segment in the MDT or CSC chambers. This definition in employed when muons cross only one layer of the MS, either because of low p_T or because they outreach the MS acceptance region.

- **Calorimeter-tagged muons (CT)**: a track in the ID is associated to a muon if it can be matched to an energy deposit in the calorimeter, consistent with a minimum-ionizing particle. The criteria for identification of this muons are optimised for

the region where the MS is only partially instrumented ($|\eta| < 0.1$) and in the momentum range 1.5 GeV $< p_t <$ 100 GeV.

- **Extrapolated muons (ME)**: the tracks are reconstructed using only the MS information additionally requiring to be compatible with originating from the IP. The muons have to traverse at least two layers of the MS and three layers in the forward region. ME muons are used to recover muon reconstruction in the η region ($2.5 < |\eta| < 2.7$) that is not covered by the ID.

These reconstructed muon candidates are schematically shown in Figure 3.5. The possi-

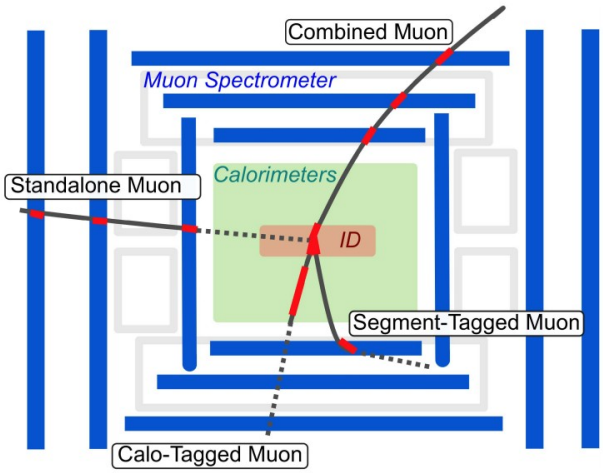

Figure 3.5: Schematic representation of all the reconstructed muon candidates [50].

bility for some overlap between the reconstructed muons is not zero. These ambiguities, i.e when two muon types share the same track, can be resolved assigning to each muon type a different level of priority: the CB muons possess the highest priority level, followed by ST muons and CT muons. For the ME muons, the track with the larger number of hits which results in the best fit outcome is selected.

3.2.1 Muon identification

The main background for muon identification is due to pion and kaon decays, in order to suppress these events specific requirements on the number of hits in the ID and MS are applied. Four muon identification selections are provided, namely:

- **Loose muons**: here all the muon types are considered and it is designed to maximise the reconstruction efficiency while providing good-quality muon tracks. All the CB and ME muons satisfying the Medium requirements are included in the

Loose selection. CT and ST muons are restricted to the $|\eta| < 0.1$ region. In the $|\eta| < 2.5$ region almost all muons are CB. This identification working point is designed for analyses with high lepton multiplicity.

- **Medium muons**: this is ATLAS default selection criteria for muons. It selects only CB and ME tracks. The former are required to have at least 3 hits in no less than two MDT layers, except for tracks in the $|\eta| < 0.1$ region, where tracks with at least one MDT layer are allowed. The latter are required to have signal from at least MDT or CSC layers in the $2.5 < |\eta| < 2.7$ region, to extend the acceptance outside the ID geometrical coverage. Systematic uncertainties associated to muon reconstruction and calibration are minimized through this selection criteria.

- **Tight muons**: this identification criteria is meant to maximise the purity of muons but with a little efficiency loss. Only CB muons that have hits in at least two stations of the MS and satisfy the Medium selection are considered.

- **High-p_T muons**: using this selection one wants to maximise the momentum resolution of tracks with $p_T > 100$ GeV. Here CB muons that satisfy the Medium selection and have three hits in the three MS stations are employed. Also, the alignment of the regions of the spectrometer is significant for the moment resolution. Therefore, the regions where the alignment is not optimal are vetoed.

The reconstruction efficiency for the four identification categories depends on η and on the muon transverse momentum as shown in Figure 3.6, it is close to 99% for $p_T > 5$ GeV almost over all the $|\eta| < 2.5$ range.

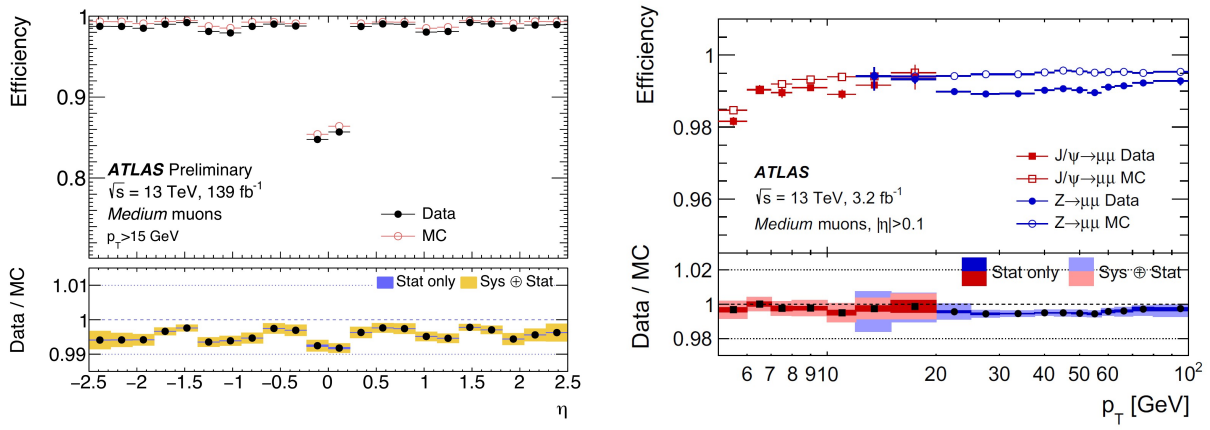

(a) (b)

Figure 3.6: On the left [51]: the reconstruction efficiency is plotted as function of η measured in $Z \to \mu\mu$ events at $\sqrt{s} = 13$ TeV for muons with $p_T > 10$ GeV. On the right [48]: the graph shows the reconstruction efficiency of Medium muons in the $0.1 < |\eta| < 2.5$ region as function of the muon p_T. The plotted values are obtained using $Z \to \mu\mu$ and $J/\psi \to \mu\mu$ events at $\sqrt{s} = 13$ TeV. Below both plot the measured to precdicted ratio is shown.

3.2.2 Muon isolation

The isolation conditions are used to discriminate prompt muons, the one originating from Z, W or Higgs boson decay which are already produced isolated from other objects, from muons produced in semileptonic decays, embedded in *jet* instead. To define muon isolation, two variables are used: a *track isolation variable*, $p_T^{varcone30}$, and a *calorimeter-based isolation variable*, $E_T^{topcone20}$. The first one is defined as the sum of the transverse momenta associated to tracks with $p_T > 1$ GeV in a cone with size

$$\Delta R = \min\,(0.3, 10\ \text{GeV}/p_T^{\mu}) \tag{3.6}$$

centered on the muon p_T, excluding the muon track itself.
The calorimeter-based variable is defined as the sum of the E_T of topological clusters in a cone of size $\Delta R = 0.2$ around the muon, after subtracting the contribution from the energy deposit of the muon itself and correcting for pile-up effects. Isolation is defined as a *relative variable* corresponding to the ratio of the track or calorimeter based isolation variables to the transverse momentum of the muon. The isolation efficiency varies from 90% to 100% depending on the transverse momentum of the muon as well as on the choice of the selection criteria.

3.2.3 Muon triggers

The L1 muon trigger [50] uses hits from the TGCs in the forward region and from RPCs in the barrel, it defines the RoIs in terms of pseudorapidity η and azimuthal angle ϕ too. The HLT uses information from the precision trackers, MDTs, CSCs and ID to reconstruct muons in the RoI. In addition isolation criteria are also applied to reject non-prompt muons. A tag-and-probe method is used to evaluate the muon trigger performances. In Figure 3.7 the absolute efficiencies for muons with respect to the offline muon p_T in the barrel ($|\eta| < 1.05$) and endcap ($1.05 < |\eta| < 2.4$) regions are shown. Relative efficiency of the HLT with respect to L1 is superimposed in the plots with blue line. The trigger efficiencies in the barrel region are lower than in the endcap. Such efficiency loss is mostly due to uncovered detector regions. The ATLAS muon trigger performances has been stable during Run 2. The L1 trigger decision in the barrel region is based on the coincidence of hits from three concentric RPC stations for the three high-p_T thresholds. To reach optimal performance for the ATLAS trigger, an effective rejection of fake muon triggers in region $1.05 < |\phi| < 1.3$ has been possible by exploiting a coincidence between the TGC chambers and the tile HADCAL. To verify the performance of the muon trigger in different pile-up conditions, the efficiency has been tested as function of the number of reconstructed vertices, Figure 3.8.

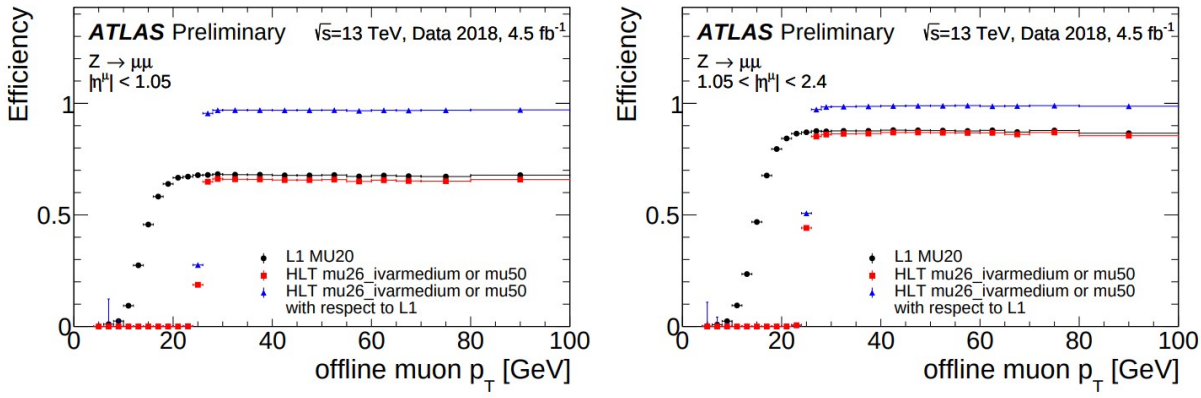

Figure 3.7: Absolute efficiencies for muons with respect to the offline muon p_T in the barrel on the left ($|\eta| < 1.05$) and endcap on the right ($1.05 < |\eta| < 2.4$) regions. Relative efficiency of the HLT with respect to L1 is superimposed in the plots with blue line.

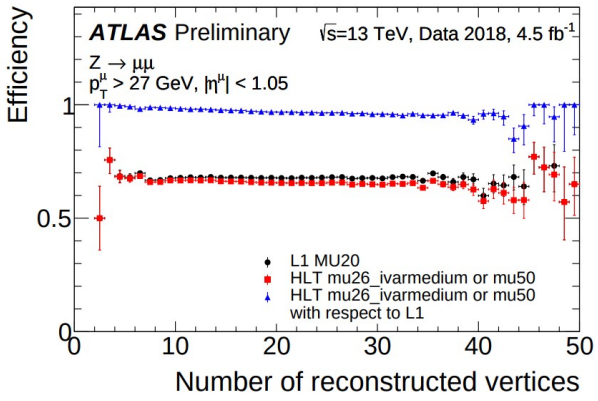

Figure 3.8: Muon trigger efficiency in the barrel region as a function of the number of reconstructed vertices. Efficiencies of L1, HLT and the total efficiency are shown for offline muons reconstructed in the barrel region with $p_T > 27$ GeV.

3.3 Tau reconstruction

Tau leptons decay, most of the time, before reaching the active regions of the ATLAS detector [52]. They decays are either leptonic:

$$\tau_{lep} \to l + \nu_l + \nu_\tau \quad \text{with} \quad l = e, \mu \tag{3.7}$$

or hadronic:

$$\tau_{had} \to \text{had} + \nu_\tau \tag{3.8}$$

the hadronic tau lepton decays represent 65% of all possible decay modes, therefore they are dominant and the decay products contain one (72% of cases) or three charged pions (22% of cases). One neutral pion can also be produced by the decay with a 68% probability. Both charged and neutral hadrons provide the visible part (τ_{vis}) of the hadronic tau decay. The main background to hadronic tau lepton decays arises from jets of energetic hadrons produced by fragmentation of quarks and gluons. Electrons also contribute to the background. To distinguish between signal and background the number of tracks and the shape of the showers inside the calorimeter are used as discriminating variables. Tau candidates are reconstructed starting from jets with $p_T > 10$ GeV and $|\eta| < 2.5$ while vetoing the transition region between the barrel and the forward calorimeters ($1.37 < |\eta| < 1.52$). The tau production vertex (PV) is identified using the *Tau Vertex Association algorithm* where PV corresponds to the track vertex candidate with the largest fraction of momentum among all the tracks within a cone of radius $R < 0.2$ around the seed jet. In order to be associated to the tau, the tracks have to satisfy the following requirements:

- the track candidate must have $p_T > 1$ GeV,

- the shortest track to vertex distances in the transverse plane d_0 and in the longitudinal plane z_0 must fulfil the relation $d_0 < 1$ mm and $|z_0 \sin\theta| < 1.5$ mm with θ the polar angle.

by meeting these conditions, the tracks are associated to the *core* ($0 < \Delta R < 0.2$) or the *isolation* ($0.2 < \Delta R < 0.4$) regions around the tau candidate.

3.3.1 Tau identification and triggers

The tau identification uses Boosted Decision Trees (BDTs) methods separately trained for tau candidates with one or three associated tracks (prongs). Simulated $Z \to \tau\tau$ form the signal sample while dijet events as background. Three working points, corresponding to different tau identification efficiency, values are provided: Loose, Medium and Tight. The L1 triggers for tau take decisions based on EM and HADCAL information. They are defined with granularity of $\Delta\eta \times \Delta\phi = 0.1 \times 0.1$. A core region consists of a set of 2×2 trigger towers and a requirement is placed on the E_T sum of the two most energetic adjacent EM calorimeter towers. At HLT level, clusters of calorimeter cells contained in a $\Delta R = 0.2$ cone around the L1 tau direction are used in the energy recalculation. Also a minimum transverse energy requirement on the online tau candidate is placed. The HLT precision track and calorimeter information is used to calculate a number of pile-up corrected variables which are then input into an online tau BDT.

3.4 Jet reconstruction and triggers

In ATLAS particle *jets* are reconstructed using *topological clusters* energy deposits in the calorimeters [53]. This process is mainly divided into three parts:

- **Jet inputs**: first begins the topocluster reconstruction starting from a seed calorimeter cell whose signal to noise ratio is above $S/N = 4$, where electronic and pile-up noise are also included in N. They are topologically-grouped noise-suppressed clusters of calorimeter cells. All cells adjacent to the seed cell with S/N 2 and $E_T > 1$ GeV are grouped together if their energy is lesser than the energy deposit associated to the seed cell. The topological clusters are then classified either as electromagnetic or hadronic using shower shapes and energy densisties by the local cluster weighting (LCW).

- **Jet algorithms**: one mostly used by ATLAS is the *anti-k_t* algorithm for jet reconstruction. Two distance parameters are defined: the distance d_{ij} between two clusters or pseudo-jets and d_{iB} corresponding to the distance between the particle i and the beam (B). The iterative procedure evaluates the distance d_{ij} for each

pseudo-jet i to the other pseudo-jet j:

$$d_{ij} = \min(p_{Ti}^{2p}, p_{Tj}^{2p}) \frac{\Delta R_{ij}^2}{R^2} \tag{3.9}$$

where $\Delta R^2 = (\eta_i - \eta_j)^2 + (\phi_i - \phi_j)^2$ is the angular distance between i and j being $p_{Ti(j)}$, $\eta_{i(j)}$ and $\phi_{i(j)}$ the transverse momentum, the pseudorapidity and the azimuthal angle. The parameter p is fixed to -1 and is the metrical distance for the anti-k_t algorithm. The distance from the beam is

$$d_{iB} = p_{Ti}^{2p}. \tag{3.10}$$

The quantities (3.9) and (3.10) are compared leading to two cases:

1. if $d_{ij} < d_{iB}$: i and j are combined into a single pseudo-jet and the iteration starts from the beginning,
2. if $d_{ij} > d_{iB}$: the pseudo-jet i is considered as a final state and no further considered into following iterations.

- **Jet grooming**: the *grooming* is a class of filtering algorithms for jets. Their aim is to get rid of certain constituents based on a defined strategy (for example the softer components of pile-up) and rebuilding the final jet from what is left behind. This procedure is necessary when considering large-R jets where an increased sensitivity to pile-up effects is expected.

Particle Flow algorithm

To reconstruct hadronic jets and soft particle activity, in Run1 of the LCH, the majority of analyses employed jets that were build from topological clusters of calorimeter cells (topo-clusters) provided as input to jet clustering algorithms. However, the high luminosity experienced during Run 2 operation represented a complication: multiple interactions, which are mostly softs, contribute to the detector signals associated with a single bunch crossing due to pile-up events and one need to separate them from the hard interactions.
An alternative is the Particle Flow (PFlow) [54] approach according to which the measurements from both the tracker and the calorimeters are combined to form the signals, corresponding to individual particles. Jet reconstruction is then carried out on a set of "particle flow object" consisting of calorimeter energy and tracks matched to the hard interaction. This new procedure, thanks to its integrated usage of tracking and calorimetric systems, gives several advantages such as:

- better pile-up events removal since the interaction vertex associated to the energy deposit is reconstructed and it is possible to keep only the contributions from primary hard-scatter vertex.

- for low-energy charged particles the momentum resolution of the tracker is significantly better than the energy resolution of the calorimeter. Also an extended acceptance of the detector to softer particles is achieved.
- the angular resolution of a charged particle reconstructed using the tracker is much better than that of the calorimeter.
- low p_T charged particles originating within a hadronic jet that are swept out of the jet none by the magnetic field before they reach the calorimeter, are detected by the tracker and clustered into the jet.

On the other hand some complications are implied. The correct identification of particle's signal in the calorimeter is necessary to avoid double-counting of its energy in the reconstruction for every particle whose track measurement ought to be used. If a particle's track measurement has to be used, the corresponding energy must be subtracted from the calorimeter measurement. The ability to accurately subtract all single particle's energy, without removing the energy deposited by any other particle, constitutes the key performance criterion upon which the algorithm is optimised.

Jet triggers

There are four implemented types of trigger for jets in ATLAS:

- *Single-jet triggers*: imposes that the transverse energy of at least one jet has to be above a certain threshold value.
- *Multi-jet triggers*: at least N jets above a certain transverse energy threshold are required.
- H_T *triggers*: jets are selected if the scalar sum of the transverse energy of all jets in the event H_T is above a given threshold.
- *Analysis-specific triggers*: used for specific topologies of interest.

3.5 Missing Transverse Energy reconstruction

The missing transverse energy (MET) E_T^{miss} quantify the momentum imbalance due to *invisible* particles, such as SM neutrinos and exotic BSM particles, which do not interact with the detector system [55]. This causes the sum of all the particles transverse momenta within a collision to be not zero, as otherwise expected from momentum conservation in the transverse plane. In ATLAS the MET is determined both from signals associated to the *hard scattering* event and *soft* events, in which are included the hard-scatter vertex

tracks that do not constitute a reconstructed object. The E_T^{miss} components in the x-y transverse plane are:

$$E_{x(y)}^{miss} = E_{x(y)}^{miss,e} + E_{x(y)}^{miss,\mu} + E_{x(y)}^{miss,\gamma} + E_{x(y)}^{miss,\tau} + E_{x(y)}^{miss,jets} + E_{x(y)}^{miss,soft} \tag{3.11}$$

and each term is defined as:

$$E_{x(y)}^{miss} = -\sum_{i}^{n} p_{x(y)}(i) \tag{3.12}$$

where i are electron, muons, tau leptons, photons, jets or soft objects. One defines also the scalar sum of all the p_T

$$H_T = \sum p_T^e + \sum p_T^\mu + \sum p_T^\tau + \sum p_T^\gamma + \sum p_T^{jets} + \sum p_T^{soft} \tag{3.13}$$

which provides a measure relative to the event activity. The fact that these quantities are reconstructed using signals from different ATLAS subdetectors makes the resulting variable sensitive to a number of uncertainties such momentum mismeauserement, miscalibration and systematic from un-instrumented regions of the detectors. The reconstructed objects used to determine E_T^{miss} and H_T are:

- **electrons**: with a Medium quality reconstruction at least. The selection is based on the shower shape in the calorimeters and the matching between energy deposit and tracks in the ID. They are required to have $p_T > 10$ GeV, $|\eta| < 1.37$ or $1.52 < |\eta| < 2.45$ avoiding the crack region $1.37 < |\eta| < 1.52$.

- **muons**: with a Medium quality reconstruction from signals in the MS and in the ID within $|\eta| < 2.5$ or only from MS track segments within $2.5 < |\eta| < 2.7$ and $p_T > 10$ GeV.

- **hadronically decaying tau**: reconstructed from jets with associated ID tracks of at least a Medium reconstruction quality. They must have $p_T > 20$ GeV and $|\eta| < 1.37$ or $1.52 < |\eta| < 2.47$.

- **photons**: they are reconstructed starting from their electromagnetic showers in the calorimeter with $p_T > 25$ GeV and $|\eta| < 1.37$ or $1.52 < |\eta| < 2.47$.

- **hard-scatter jets**: they are reconstructed from topo-clusters in the calorimeter using anti-k_t algorithm and are further selected through a jet vertex tagger variable (JVT) raging from 0 (pile-up jet) to 1 (hard-scatter jet), the JVT discriminant is built by defining a two-dimensional likelihood based on a k-nearest neighbour algorithm [56]. Jets are required to have $p_T > 20$ GeV within $|\eta| < 2.4$, $p_T > 60$ GeV within $|\eta| < 4.4$ or 20 GeV $< p_T <$ 60 GeV and $JVT > 0.59$ within $|\eta| < 2.4$.

- **soft-term**: this is reconstructed from ID tracks associated to the hard-scatter vertex and are required to have $p_T > 400$ MeV and $|\eta| < 2.5$. The main algorithm used in ATLAS is the Tracks Soft Term (TST), which fully relies on tracks. Further rquirements are set on track to vertex distances in the transverse plane d_0 and on the longitudinal one z_0: $|d_0| < 1.5$ mm and $|z_0 \sin\theta| < 1.5$ mm.

3.5.1 Missing Transverse Energy triggers

In ATLAS different types of trigger are used at the HLT stage for the MET. These triggers are implemented using different algorithms which take as input the energy measurements in the calorimeter:

- **Cell algorithm**: here the signal from calorimeter cell is used. The E_T^{miss} is computed using the measured energy in each calorimeter cell and the position of the cell in the detector. In this way one obtains the components of the cell meaured momentum. The total p_T^{miss} is defined as:

$$p_T^{miss} = -\sum_i (p_{x,i}, p_{y,i}) \tag{3.14}$$

  the MET is calculated from its norm $E_T^{miss} = |p_T^{miss}|$.

- **Jet-based algorithm**: in this case the E_T^{miss} is calculated directly from the negative of the transverse momentum vector sum of all reconstructed jets.

- **Topo-cluster algorithm**: Topological cluster are formed in a multistage process and are used for the E_T^{miss} reconstruction. For each topo-cluster, the momentum components are calculated and the p_T^{miss} is calculate from negative vector sum of the components.

- **Pile-up suppression algorithm**: base on the topo-cluster E_T^{miss} algorithm, here in addition a further pile-up suppression is employed to limit the degradation of the E_T^{miss} resolution at very high pile-up.

- **Pile-up fit algorithm**: similar to the pile-up suppression algorithm, the pile-up fit algorithm corrects for pile-up effects on high-E_T calorimeter signals contributing to E_T^{miss}. It employs a pile-up estimate obtained from a fit to lower-E_T signals. It takes as inputs the topological clusters and combines them into $\eta - \phi$ patches that correspond approximately to the size of a jet with R=0.4. The fit estimates the energy contribution from pile-up. The pile-up subtracted patches are used to determine the E_T^{miss}.

3.6 Overlap Removal

Along with the object reconstruction routine comes the possibility for one physical object to be reconstructed as two different ones. The overlap removal (OR) procedure resolves this ambiguity also in case of two separate object occupying close-by regions in the detector. It follows the common prescription provided by the ATLAS performance group. The OR algorithm resolves the following overlaps using the distance ΔR between the objects in the $\eta - \phi$ plane:

- **electron-muon**: when a muon overlapping with and electron leaves enough high energy (through final state radiation or bremmsstrahlung) in the calorimeter and shares the same ID track with an electron or they are closer than $\Delta R < 0.01$, the muon is removed. This is the case if the muon has no associated MS signal, otherwise the electron is removed.

- **electron-jets**: in this case the algorithm aims to remove either jets coinciding with reconstructed electrons ($\Delta R < 0.2$) or to remove the electron when the spatial separation between them is too small ($0.2 < \Delta R < 0.6$).

- **muon-jets**: bremmsstrahlung or final state radiation produced by muons can lead to a jet very close to a muon track, in this case the ID track is combined with the photon energy deposit in the EM calorimeter and reconstructed both as a muon and a jet. Pile-up can also result in a jet and a muon in the same detector area from different bunch crossing. In this scenario, jets within $\Delta R < 0.2$ of a muon and featuring less than three tracks or with $p_T(\mu)/p_T(\text{jet}) > 0.5$ are removed.

3.7 ATLAS data format

Since a typical high energy physics analysis is very demanding in terms of how many times a data sample is scanned and the different event selection requirements to retrieve specific information, it is convenient to use a data format that contains all the relevant information in a reasonable small dimension. In atlas the data processing and analysis are performed with the *Athena* framework [57]. Typically these formats are obtained directly from the retained output of the reconstruction, the so-called *Analysis Object Data* or AOD with the following features:

- their size is a few percent to a few per mille of the input data;

- they usually contain all of the information useful for the combined performance operations (as selection, calibration and other operations on reconstructed objects);

- they are usually made for a specific use in a group of related analyses.

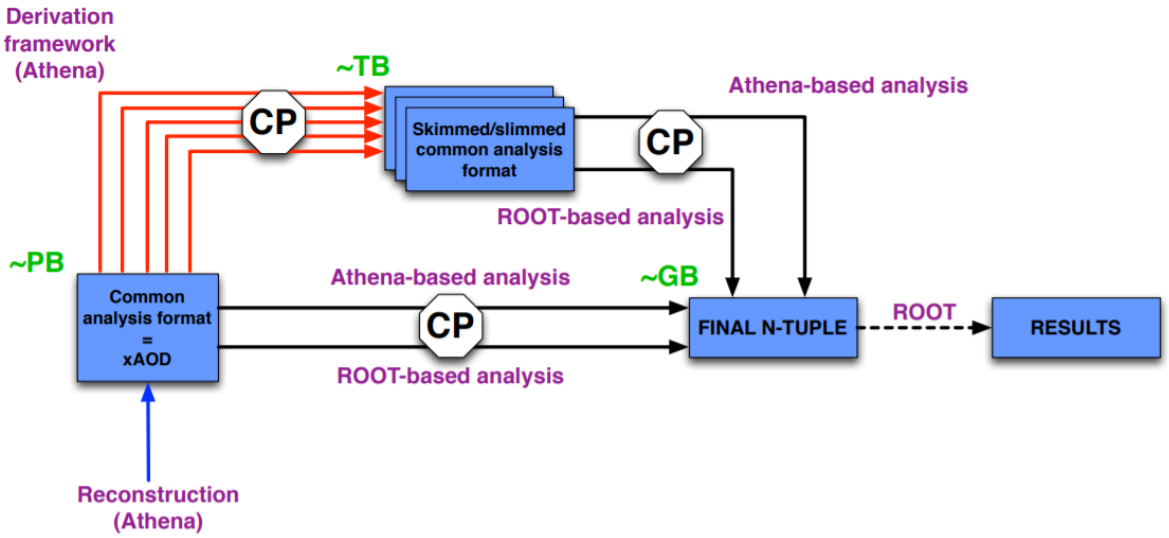

Figure 3.9: The ATLAS analysis model for Run 2.

Figure 3.9 shows the analysis model adopted by ATLAS for Run 2 which is based on three elements. First, the input data format is the ROOT-readable xAOD (replacing the not ROOT-readable AOD) produced directly by the reconstruction. The second element is the *Derivation Framework*, this is an offline tool responsible for the data reduction strategy. It creates the intermediate data format from the xAOD, the Derived-xAOD or DxAOD. The Derivation Framework implements three standard operations for information removal:

- *skimming*: the whole events are removed, based on some criteria related to derivation requests.
- *thinning*: removal of individual objects within an events, base on some derivation requests.
- *slimming*:removal of variables within a given object type, uniformly across all objects of that type and all events.

The third component is the analysis framework, which is used to read the derived data formats and produce the final small n-tuples then used in statistical analyses.

Chapter 4

Search for scalar and vector doubly charged bosons

In this chapter we present the search of scalar and vector doubly charged bosons with Run 2 data collected by the ATLAS experiment at LHC considering multi-lepton final states. The search uses the proton-proton collision data samples at $\sqrt{s} = 13$ TeV corresponding to 139 fb^{-1} of total integrated luminosity recorded from 2015 to 2018. The search targets decays of $Y^{\pm\pm}$, $H^{\pm\pm}$ (both from 3-3-1 Model) and $\Delta^{\pm\pm}$ (from LRSM) into prompt light leptons (electrons and muons) and leptons from tau decay.

4.1 Signals and background description

4.1.1 Analysis final state

The main production mechanism for $Y^{\pm\pm}$, $H^{\pm\pm}$ and $\Delta^{\pm\pm}$ is pair production via Drell-Yan process as presented in Section 1.2.1 and Section 1.2.2, respectively. The analysis assumes the following decay:

$$pp \to Y^{++}Y^{--}(H^{++}H^{--}, \Delta^{++}\Delta^{--}) \to \ell^+\ell^+\ell'^-\ell'^- \tag{4.1}$$

where the final state consists of four charged leptons ($\ell, \ell' = e, \mu$) arranged in two same-sign (SS) and same-flavour lepton pairs for $Y^{\pm\pm}$ and $H^{\pm\pm}$, differently for the $\Delta^{\pm\pm}$ since it can decay also violating the lepton flavour. This is convenient for our research since events from SM processes rarely produce two SS lepton: processes with relatively large cross-section, such as Z/γ^* or $t\bar{t}$ production, lead to two opposite-sign (OS) leptons.
Final states containing two or three light leptons are also considered, as shown in Table 4.1. This inclusion is not in contradiction with assuming the absence of lepton-flavour violating decays for $Y^{\pm\pm}$. Indeed, this is done to increase signal efficiency. These final states are included due to a number of reasons such as the charge mis-reconstruction,

	1P2L	1P3L	2P4L
Electron channel	$e^{\pm}e^{\pm}$	$e^{\pm}e^{\pm}e^{\mp}$	
Mixed channel	$e^{\pm}\mu^{\pm}$	$e^{\pm}\mu^{\pm}\ell^{\mp}$	$\ell^{\pm}\ell^{\pm}\ell^{\mp}\ell^{\mp}$
		$\ell^{\pm}\ell^{\pm}\ell'^{\mp}$	
Muon channel	$\mu^{\pm}\mu^{\pm}$	$\mu^{\pm}\mu^{\pm}\mu^{\mp}$	

Table 4.1: Signal channels used in the analysis. Final states of interest are divided into: one same-sign pair and two leptons (1P2L), one same-sign pair and three leptons (1P3L), two same-sign pair and four leptons (2P4L). Here $\ell = e, \mu$ and in the three lepton final state $\ell^{\pm}\ell^{\pm}\ell'^{\mp}$ indicates that the same-sign leptons have the same flavour, while the opposite sign (OS) leptons may have a different flavour.

particle's interaction with the detector and also selection acceptance. Therefore, according to lepton multiplicity, different *analysis regions* are defined. The two and three lepton categories are fundamental to retrieve events where a fourth lepton is lost due to selection acceptance. For the four lepton signal region, due to the low expected number of events, only the inclusive flavour final state is considered.

m($\Delta^{\pm\pm}$) GeV	$\sigma(\Delta^{\pm\pm})$[fb]	m($Y^{\pm\pm}$) GeV	$\sigma(Y^{\pm\pm})$[fb]	m($H^{\pm\pm}$)) GeV	$\sigma(H^{\pm\pm})$[fb]
300	23.76	-	-	-	-
400	6.98	-	-	-	-
500	2.51	-	-	-	-
600	1.03	-	-	-	-
700	0.46	-	-	700	2.39
800	0.21	-	-	800	2.04
900	0.11	-	-	900	1.71
1000	0.057	1000	13.51	1000	1.39
1100	0.031	1100	7.95	1100	1.09
1200	0.016	1200	4.53	1200	0.80
1300	0.0094	1300	2.45	1300	0.55
-	-	1400	1.21	1400	0.34
-	-	1500	0.52	1500	0.18
-	-	1600	0.19	-	-
-	-	1700	0.037	-	-
-	-	1800	0.016	-	-
-	-	1900	0.011	-	-

Table 4.2: Theoretical cross-sections for the pair-production of doubly charged bosons in pp collisions at $\sqrt{s} = 13$ TeV.

4.1.2 Collision Data and Monte Carlo samples

Collision Data

In this analysis, the experimental data cover the entire duration of LHC Run 2 period from 2015 to 2018. In the left panel of Figure 4.1 the $\langle\mu\rangle$ of pp interaction per bunch crossing (pile-up) is reported. Here $\langle\mu\rangle$ corresponds to the mean of the Poisson distribution of the number of interactions per crossing calculated for each proton bunch. It is calculated from the instantaneous bunch luminosity.

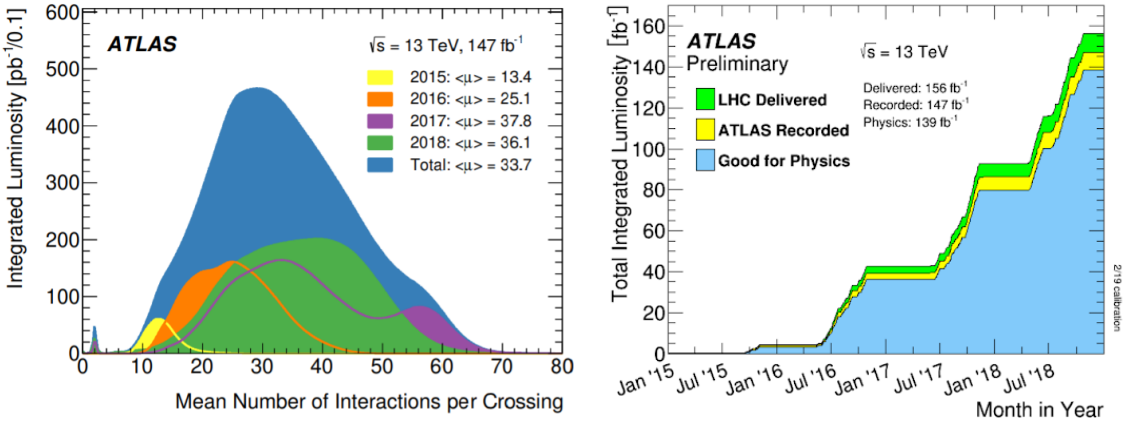

Figure 4.1: Left: luminosity-weighted distribution of the mean number of interactions per bunch crossing, μ, for the full Run 2 pp collision dataset at $\sqrt{s} = 13$ TeV. All data recorded by ATLAS during stable beams are shown. The integrated luminosity and the mean μ value for each year are given also. Right: total integrated luminosity and data quality in 2015-2018. Cumulative luminosity versus time delivered to ATLAS (green), recorded by ATLAS (yellow), and certified to be good quality data (blue) during stable beams for pp collisions at $\sqrt{s} = 13$ TeV in 2015-2018.

In ATLAS each datasets, taken while the experiment is continuously recording, is called *run* which is further divided into *luminosity blocks* (LBs). A LB is defined as the time interval (nominally 60 s) during which instantaneous luminosity, detector, trigger configuration and data quality conditions are constant. For the analysis only the LBs where all the sub-detectors were in good data-taking conditions are selected. The set of these "good" luminosity blocks is *Good Run List* (GRL). The luminosities corresponding to the GRLs used in this analysis are 3.2 fb^{-1}, 33.0 fb^{-}1, 43.6 fb^{-1} and 60.0 fb^{-1} for 2015, 2016, 2017 and 2018 respectively.
The events are collected using different triggers depending on the channel, see Table 4.3. For the electron and muon channels, dielectron and dimuon triggers are used while for the mixed channel combined electron-muon triggers are used. The dilepton trigger

are also used for the three and four lepton channel. Electrons are required to have at least `lhloose` (loose) and `lhvloose` (very loose) offline reconstruction level, as defined in Chapter 3. The trigger selection for muons choose only the ones with `Medium` working point at the trigger level, see Chapter 3. In the mixed channel the events are selected requiring a p_T threshold of 17 GeV for electrons and 14 GeV for muons.

	2015	2016	2017+2018
ee	HLT_2e12_lhloose_L12EM10VH	HLT_2e17_lhvloose_nod0	HLT_2e17_lhvloose_nod0_L12EM15VHI OR HLT_2e24_lhvloose_nod0
$e\mu$	HLT_e17_lhloose_mu14	HLT_e17_lhloose_nod0_mu14	HLT_e17_lhloose_nod0_mu14
$\mu\mu$	HLT_mu18_mu8noL1	HLT_mu22_mu8noL1	HLT_mu22_mu8noL1

Table 4.3: A summary of the used triggers in 2015, 2016, 2017 and 2018 data taking periods.

Monte Carlo samples

Monte Carlo generators are used to simulate both signal and background processes as summarized in Table 4.4. In the analysis we use:

- 21 MC samples for the doubly charged Higgs boson ($\Delta^{\pm\pm}$) from the LRSM, the mass points go from 300 GeV to 1300 GeV with 50 GeV step;
- 10 MC samples for the doubly charged vector boson $Y^{\pm\pm}$ where the mass points starts from 1000 GeV to 1900 GeV separated by 100 GeV each;
- 9 MC samples for the doubly charged Higgs boson ($H^{\pm\pm}$) from the Dilepton model, with the mass points between 700 GeV and 1500 GeV with step of 100 GeV.

The $Y^{\pm\pm}$ MC sample is produced using `MadGraph` event generator interfaced to `Pythia [8.186]` for parton showering. $Y^{\pm\pm}$ signal events are generated at the leading order (LO) and the `NNPDF23LO` PDF set is used to compute the matrix element. Also the $H^{\pm\pm}$ MC sample is simulated using `MadGraph` event generator at LO and `MadGraph` for parton showering. The signal sample for $\Delta^{\pm\pm}$ is generated at LO using `Pythia` implementing the left-right symmetric model production via Drell-Yan pair production only with `NNPDF2.0NLO`. Also for this signal sample the parton shower is reproduced with `Pythia[8.230]`.

SM background composition depends on the analysis region considered. For instance, events containing three leptons tend to be more affected by diboson background, while the two lepton region by Drell-Yan and fakes events. Background sources are divided into three types:

- Prompt SM processes: mainly from diboson (WZ, ZZ, $W^{\pm}W^{\pm}$), Z + jets and $t\bar{t}$ events;

Physics process	Event generator	ME PDF set	Cross-section normalization	Parton shower	Parton shower tune
Signal $\Delta^{\pm\pm}$	Pythia	NNPDF3.0LO	LO	PYTHIA[8.230]	A14
Signal $H^{\pm\pm}$	MADGRAPH	NNPDF2.3NLO	LO	MADGRAPH	A14
Signal $Y^{\pm\pm}$	MADGRAPH	NNPDF2.3LO	LO	PYTHIA[8.186]	A14
Drell-Yan					
$Z/\gamma^* \to ee/\mu\mu$	SHERPA[2.2.1]	NNPDF3.0NNLO	NLO	SHERPA	SHERPA default
Top physics					
ttbar	POWHEGBOX[v2]	NNPDF3.0NNLO	NNLO	PYTHIA[8.230]	A14
Single t	POWHEGBOX[v2]	NNPDF3.0NNLO	NNLO	PYTHIA[8.230]	A14
$3t$, $4t$	MCatNLO	NNPDF2.3LO	LO	PYTHIA[8.230]	A14
ttbar + $W/Z/H$	MCatNLO	MEN30NLO	NNLO	PYTHIA[8.230]	A14
Diboson					
ZZ, WZ	SHERPA[2.2.1] & 2.2.2	NNPDF3.0NNLO	NLO	SHERPA	SHERPA default
Multiboson					
WWW, WWZ, WZZ, ZZZ	SHERPA[2.2.1] & 2.2.2	NNPDF3.0NNLO	NNLO	SHERPA	SHERPA default

Table 4.4: Simulated signal and background event samples: the corresponding event generator, parton shower, cross-section normalization, PDF set used for the matrix element and set of tuned parameters are shown for each sample.

- Non-prompt and fake backgrounds;
- Lepton charge mis-identification.

Prompt background consists of particles originating from or very close to the primary interaction point. On the other hand, non-prompt background is due to semileptonic decays of hadrons containing b or c quarks, as in $t\bar{t}$, Z + jets, W + jets processes. In addition to this, the fake background arises from hadronic jets that are mis-identified as prompt charged leptons. Finally, the last type of background is due to processes like $Z \to (\ell^+\ell^-)$ + jets where one of the charged leptons may have been reconstructed with the wrong charge. The background samples employed in the analysis are:

- **Drell-Yan** is the highest-yield process which enters in the analysis through charge mis-identification $q\bar{q} \to Z/\gamma^* \to \ell^+\ell^-$, followed by $t\bar{t}$ process. It is modelled using `SHERPA[2.2.1]` and `SHERPA` for parton showering. The `NNPDF3.0NNLO` PDF set was used to calculate the hard scattering process.
- **$t\bar{t}$** events are generated with `POWHEGBOX[v2]` using `Pythia[8.230]` for parton showering. The `A14` parameter set is used in combination with the `NNPDF3.0NNLO` PDF set for tuning the shower.
- **Single-top** events are events produced in Wt final states are generated with `POWHEGBOX[v2]` and the `NNPDF3.0NNLO` PDF set. The parton shower, hadronization, and underlying event were simulated with `Pythia[8.230]`.
- **Rare-top** consist of processes where $3t$, $4t$ or $t\bar{t} \to W/Z$ may appear. Both their production is modeled using `MCNLO` event generator. The PDF sets used are `NNPDF2.3LO` for $3t$, $4l$ and `MEN30NLO` for the process $t\bar{t} \to W/Z$. The parton shower in both cases is described with `Pythia[8.230]`.

- **Diboson** where two bosons decay leptonically: $VV \to 4\ell, 3\ell + 1\nu, 2\ell + 2\nu$. It is an irreducible background since its final state is similar to the signal final state for $H^{\pm\pm}$, $Y^{\pm\pm}$ and $\Delta^{\pm\pm}$. Diboson contribution to the same-charge final states is large because of its large cross section: the production cross-section measured by ATLAS are $\sigma(pp \to ZZ) = 17.3 \pm 0.6 \pm 0.8$ pb, and $\sigma(pp \to ZW) = 51 \pm 0.8 \pm 2.3$ pb. The modeling of this background is performed using `Sherpa [2.2.1] & [2.2.2]`. The PDF used is `NNPDF3.0NNLO` while `SHERPA` was used for the parton showering.

- **Multiboson** represents an ensamble of processes involving the presence of WWW, WWZ, WZZ, ZZZ bosons. The background is simulated using `SHERPA [2.2.1] & [2.2.2]` with the `NNPDF3.0NNLO` PDF set for the matrix element calculation and `SHERPA` for the parton showering.

4.2 Objects definition

The way objects are defined and reconstructed in ATLAS was already presented in Chapter 3. Now a separate definition of the objects used in the analysis is given. The definition used for leptons is based on their reconstruction, identification and isolation requirements and correspond to different efficiency and purity levels. Also jets and the MET follow a specific definition for the analysis. Two different sets of requirements are defined in this analysis to select electrons and muons. Leptons satisfying these criteria are referred to as *tight* and *loose* leptons. The former are selected in the signal region, while loose ones are primarily useful for background estimation.

Electrons

The reconstruction of electron objects is based on the information measured by the EM calorimeter and the ID subsystems. The signal electrons used in the analysis are chosen to pass `LHTight` identification level and `FCLoose` isolation requirements in order to further suppress the jet background. All electrons are required to pass at least the `LHLooseBL` identification level, where at least one pixel hit in the B-layer is required in addition to `LHLoose` criteria. This selection does not impact negatively on the signal yield since the electrons from both the $\Delta^{\pm\pm}$, $Y^{\pm\pm}$ and $H^{\pm\pm}$ are expected to have high momenta. The other selection cuts such the ones for d_0 and z_0 (the transverse and longitudinal track parameters) are used to ensure that only isolated, prompt electrons originating from the primary vertex are selected as summarized in Table 4.5.

Requirement	Signal electrons (tight)	Background electrons (loose)
Identification	`LHTight`	`LHLoose` OR
Isolation	`FCLoose`	fail `FCLoose` or fail tight selection
p_T cut	$p_T > 40$ GeV	$p_T > 40$ GeV
η cut	$\|\eta\| < 2.47$ and veto $1.37 < \|\eta\| < 1.52$	$\|\eta\| < 2.47$ and veto $1.37 < \|\eta\| < 1.52$
$\|d_0\|/\sigma_{d_0}$ cut	$\|d_0\|/\sigma_{d_0} < 5.0$	$\|d_0\|/\sigma_{d_0} < 5.0$
$\|z_0 \sin\theta\|$ cut	$\|z_0 \sin\theta\| < 0.5$ mm	$\|z_0 \sin\theta\| < 0.5$ mm
Bad cluster veto	yes	yes

Table 4.5: Summary of the baseline electron definitions in the analysis.

Muons

Muons with $p_T > 40$ GeV and within the acceptance $|\eta| < 2.5$ are used in the analysis. Quality requirements are imposed to the muon reconstruction according to the *Medium* working point, while the *High* p_T working point is used for $p_T > 300$ GeV. Background muons are real muons embedded within a jet and produced by in-flight decays of secondary mesons inside the jet. For this reason, the detector activity surrounding these muons, known as *isolation* is used to discriminate between background and prompt muons. A track-based isolation variable $p_T^{varcone30}$ is used to distinguish between isolated and non-isolated muons. Tight muons are selected by requiring $p_T^{varcone30} < 0.06$ corresponding to the so called `FixedCutTightTrackOnly` working point of the isolation. The requirements on the transverse impact parameter significance $|d_0|/\sigma_{d_0}$ and the longitudinal impact parameter multiplied by the polar angle, $|z_0 \sin\theta|$, are used to distinguish between prompt and background muons. The previous requirements and cuts are summarized in Table 4.6.

Requirement	Signal muons (tight)	Background muons (loose)
Quality	`HighPt` if $p_T > 300$ GeV else `Medium`	`HighPt` if $p_T > 300$ GeV else `Medium`
Bad muon veto	yes	yes
Isolation	`FixedCutTightTrackOnly`	fail `FixedCutTightTrackOnly`
p_T cut	$p_T > 40$ GeV	$p_T > 40$ GeV
η cut	$\|\eta\| < 2.5$	$\|\eta\| < 2.5$
$\|d_0\|/\sigma_{d_0}$ cut	$\|d_0\|/\sigma_{d_0} < 3.0$	$\|d_0\|/\sigma_{d_0} < 3.0$
$\|z_0 \sin\theta\|$ cut	$\|z_0 \sin\theta\| < 0.5$ mm	$\|z_0 \sin\theta\| < 0.5$ mm

Table 4.6: Summary of the baseline muon definition in the analysis.

Jets

As described in Section 3.4, jets are reconstructed by clustering energy deposits in the calorimeter with the anti-k_t algorithm with a radius parameter R = 0.4, where energy

clusters are calibrated at the EM-scale. The *Medium* jet-vertex-tagger (JVT) working point is used. Jets considered in this analysis are required to have $p_T > 20$ GeV and with acceptance $|\eta| < 2.5$. In the analysis the events containing $b-$jets are vetoed in order to reduce the fake background. These jets are identified with a multivariate discriminant (MV2) providing a b-jet efficiency of 77% in simulated $t\bar{t}$ events and a background rejection against jets originated by light quarks of 40% and 20% for those from c-quarks.

Requirement	Signal jets	Baseline jets
Jet type	`AntiKt4EMPFlowJets`	`AntiKt4EMPFlowJets`
JVT working point	`Medium`	`Medium`
fJVT working point	—	—
p_T cut	$p_T > 20$ GeV	$p_T > 20$ GeV
η cut	$\|\eta\| < 2.5$	$\|\eta\| < 4.5$
b-tagging	`MV2c10` with `FixedCutBEff_77`	

Table 4.7: Summary of the baseline jet definitions in the analysis.

MET

The missing transverse energy E_T^{miss} is associated to the undetected energy in the event, this may be caused by neutrinos escaping detection or to other particles outside the acceptance, or badly reconstructed. The E_T^{miss} is computed as the unbalance of the total visible p_T in the event with contribution from all visible objects in the event.

4.3 Analysis strategy

4.3.1 Analysis regions

The main goal for a successful analysis strategy is to improve the signal efficiency and to control and suppress as much as possible background sources. Events are classified in independent categories, called *analysis regions* which are optimized for specific purposes: the *control regions* are region enriched of background events, used to constrain free parameters in the statistical analysis; the background estimation is validated against data in *validation regions*; the *signal regions* are dominated by signal-like events and ideally characterized by a low background contribution. To define analysis regions, the signal significance is used

$$S = \sqrt{2 \cdot [(s+b)\log(1+s/b) - s]} \tag{4.2}$$

where s and b are the number of signal and background events [58].
These regions are mutually orthogonal, this means that the same events must not fall into different regions. Analysis regions, here considered, are also defined on the basis of the lepton multiplicity. This strategy is convenient since the background events previously cited are present in different measure depending on the number of leptons we have in the final state. A further regions separation into *channels* depending on the flavour combination of the same-charge pair ($e^{\pm}e^{\pm}, e^{\pm}\mu^{\pm},$ and $\mu^{\pm}\mu^{\pm}$) is applied to enhance sensitivity. A summary of all used regions is shown in Table 4.8.
There are some general requirements for the events in order to be included in a certain region: events with two or three leptons must have one same-sign lepton pair while events with four leptons are required to have two same-sign pairs with a zero total charge. Among the different variables upon which the regions are defined, the most discriminating is the invariant mass of the same-charge lepton pairs: in the signal region only pairs with invariant mass above 200 GeV are considered and below 200 GeV in the control and validation regions where the most of the background is expected.

Control and validation regions

In this search there are three main backgrounds contributions: fake leptons, Drell-Yan and diboson production. Several control and validation regions are defined:

- The *opposite-charge control region* (OCCR) is designed to constrain the Drell-Yan background requiring the presence of exactly two opposite-sign electrons. The normalization factor obtained is then applied to all the regions where a contribution from Drell-Yan is present.

- The *diboson control region* (DBCR) is defined as a three lepton region to constrain the diboson background yield. In this region the presence of at least one leptonic Z boson is required by applying a cut on the opposite-charge same-flavour pair: 81.2 GeV $< m(l^+l^-) <$ 101.2 GeV.

- The *four-lepton control region* (CR4L) is used to constrain the yield of the diboson background in four-lepton regions. The Z boson veto is not applied in this region in order to increase the available number of simulated diboson events.

- The *same-charge validation region* (SCVR), requiring two same-charge leptons, is used to validate the data-driven fake background estimation in all channels, an the goodness of the charge mis-identification estimate when electrons are involved.

- The *three-lepton validation regions* (VR3L, VR3L_60) are used to validate the SM diboson background and fake events with three reconstructed leptons.

- The *four-lepton validation region* (VR4L) is designed to validate the diboson modelling in the four-lepton region.

As shown in Table 4.8 the lower mass bound of 60 GeV is imposed to discard events from low-mass resonances. This is increased to 90 GeV in the three-lepton regions and to 130 GeV in the two lepton regions. The reason for increasing the lower mass bound in the region containing electron is the data-driven electron charge mis-identification background estimation where the $Z \to e^+e^-$ peak is used for the extraction of the charge-flip rates. Setting this bound to 130 GeV in the two-lepton regions completely removes the Z peak region, while a bound of 90 GeV in the three-lepton regions (due to a lower mis-identification rate) reduces the statistical uncertainty of the sample. Instead, the charge mis-identification background does not affect the muon channel, the lower mass bound stays as loose as 60 GeV.

	control regions				signal regions			validation regions			
	OCCR	DBCR	DBCR_60	CR4L	SR_1P2L	SR_1P3L	SR_2P4L	SCVR	VR3L	VR3L_60	VR4L
Channel	e^+e^-	$\ell^\pm\ell^\pm\ell^\mp$ $e^\pm e^\pm e^\mp$ $e^\pm e^\pm\mu^\mp, e^\pm e^\mp\mu^\pm$ $e^\pm\mu^\pm\mu^\mp, e^\mp\mu^\pm\mu^\pm$	$\mu^\pm\mu^\pm\mu^\mp$	$\ell^\pm\ell^\pm\ell^\mp\ell^\mp$	$\ell^\pm\ell^\pm$	$\ell^\pm\ell^\pm\ell^\mp$	$\ell^\pm\ell^\pm\ell^\mp\ell^\mp$	$e^\pm e^\pm$ $e^\pm\mu^\pm$ $\mu^\pm\mu^\pm$	$\ell^\pm\ell^\pm\ell^\mp$ $e^\pm e^\pm e^\mp$ $e^\pm e^\pm\mu^\mp, e^\pm e^\mp\mu^\pm$ $e^\pm\mu^\pm\mu^\mp, e^\mp\mu^\pm\mu^\pm$	$\mu^\pm\mu^\pm\mu^\mp$ $e^\pm e^\pm\mu^\mp, e^\pm e^\mp\mu^\pm$ $e^\pm\mu^\pm\mu^\mp, e^\mp\mu^\pm\mu^\pm$	$\ell^\pm\ell^\pm\ell^\mp\ell^\mp$
Nr. Leptons	2	3	3	4	2	3	4	2	3	3	4
$m(\ell^\pm\ell^\mp)_{OS}$[GeV]	[130, ∞)	-	-	-	-	-	-	-	-	-	-
$m(\ell^\pm\ell^\pm)_{lead}$[GeV]	-	[90, 200)	[60, 200)	[60, 150)	[200, ∞)	[200, ∞)	[200, ∞)	[130, 200)	[90, 200)	[60, 200)	[150, 200)
$p_T(\ell^\pm,\ell^\pm)_{lead}$[GeV]	-	-	-	-	≥ 300	≥ 300	-	-	-	-	-
$\Delta R(\ell^\pm,\ell^\pm)$	-	-	-	-	< 3.5	-	-	-	-	-	-
$\overline{M}$ [GeV]	-	-	-	-	-	-	≥ 300	-	-	-	
Z-veto	-	inverted	inverted	-	-	✓	✓	-	✓	✓	-
b-jet veto	✓	✓	✓	✓	✓	✓	✓	✓	✓	✓	✓

Table 4.8: Summary of all regions used in the analysis. The table is split into three blocks: the upper block indicates the final states for each region; the middle block indicates the number of leptons counted in the final state; the lower block contains the mass range of the corresponding final state and the event selection criteria for the region. The application of a selection requirement is indicated by a check mark ✓.

Signal regions

As stated at the beginning of this chapter, three signal regions are defined, Table 4.8: *two same-sign leptons* (SR_1P2L), *three-lepton region with one same-sign lepton pair* (SR_1P3L) and *four-lepton region with two same-sign lepton pairs* (SR_2P4L). Although these regions are characterized by an invariant mass of the same-sing lepton pairs above 200 GeV, other cuts are applied in order to maximize the signal sensitivity. These cuts exploit the signal and background kinematic distributions. When pair production happens, the bosons ($\Delta^{\pm\pm}$, $Y^{\pm\pm}$, or $H^{\pm\pm}$) are expected to have the same mass and to be produced almost back-to-back and their decay products are assumed to have high transverse momenta and to produce a narrow high-mass resonance peak, which is not the case for same-charge leptons from SM backgrounds.
For the SR_1P2L and SR_1P3L signal regions the main background depends on the

lepton flavour: electron channels are almost equally affected by Drell-Yan, diboson and fake contamination while for the mixed and muon channels Drell-Yan is not present. By requiring $\Delta R(\ell^{\pm}, \ell^{\pm}) < 3.5$ (distance between the two SS leptons) $p_T(\ell^{\pm}, \ell^{\pm}) \geq 300$ GeV (transverse momentum of the SS pair) a substantial background fraction is rejected. In regions with four leptons the major background arises from diboson events. One way to reduce the ZZ contribution is to apply a Z-veto, removing events where the opposite-sign same-flavour lepton pairs has an invariant mass within 10 GeV of the Z boson mass. In this region the transverse momentum and separation cuts are not included in order to maximize the available statistic. Since the doubly charged bosons and consequently the two same-sign lepton pairs are expected to have the same invariant mass, a cut on the invariant mass difference is applied: $\bar{M} = (m^{++} + m^{--})/2 \geq 300$ GeV. Its value depends on the flavour combinations and especially suppresses the ZZ background. In the following some cut-flow for the signal samples $Y^{\pm\pm}$, $H^{\pm\pm}$ and $\Delta^{\pm\pm}$ are reported for a common mass point of 1000 GeV, Tab 4.9-4.16.

$e^{\pm}e^{\pm}$	$Y^{\pm\pm}$		$H^{\pm\pm}$		$\Delta^{\pm\pm}$	
	Yields	Rel. Yields	Yields	Rel. Yields	Yields	Rel. Yields
Preselection	1.08×10^5	1	9.97×10^4	1	3.89×10^5	1
Number of jets	1.08×10^5	1	9.97×10^4	1	3.89×10^5	1
Two loose leptons	3.75×10^4	0.348356	3.47×10^4	0.347608	9.84×10^4	0.252851
Triggers	3.75×10^4	0.34817	3.46×10^4	0.347508	9.83×10^4	0.252779
Trigger matching	3.6×10^4	0.334677	3.34×10^4	0.334861	9.22×10^4	0.236902
Bad muon veto	3.56×10^4	0.3306	3.3×10^4	0.330579	9.11×10^4	0.234218
Two tight leptons	3.35×10^4	0.311108	3.1×10^4	0.310941	8.63×10^4	0.221767
Analysis channel	1.57×10^4	0.145965	1.47×10^4	0.147422	2.55×10^4	0.0656354
Charge	1.35×10^4	0.125795	1.27×10^4	0.127323	8.75×10^3	0.0224885
Number of b-jets	1.1×10^4	0.101929	1.02×10^4	0.102701	7.47×10^3	0.0192061
$m_{\ell\ell}$ SS lead. pair	1.1×10^4	0.101817	1.02×10^4	0.102581	7.45×10^3	0.0191598
$\Delta R(\ell^{\pm}, \ell^{\pm})_{lead.lep.pair}$	1.09×10^4	0.100842	1.02×10^4	0.101959	7.29×10^3	0.0187357
Di-lepton p_T, SS lead. pair	1.06×10^4	0.0985671	1.01×10^4	0.101437	6.81×10^3	0.0175122

Table 4.9: Cut-flow for the two leptons region in the electron channel. In the first column the selection cuts are listed, *Preselection* means that no cut has been applied yet and then corresponds to the total number of events contained in the sample. The other two columns show the number of events remaining after each cut and the relative number of yields. The samples have a common mass point of 1000 GeV.

$\mu^{\pm}\mu^{\pm}$	$Y^{\pm\pm}$		$H^{\pm\pm}$		$\Delta^{\pm\pm}$	
	Yields	Rel. Yields	Yields	Rel. Yields	Yields	Rel. Yields
Preselection	1.08×10^5	1	9.97×10^4	1	3.89×10^5	1
Number of jets	1.08×10^5	1	9.97×10^4	1	3.89×10^5	1
Two loose leptons	3.75×10^4	0.348356	3.47×10^4	0.347608	9.84×10^4	0.252851
Triggers	3.75×10^4	0.34817	3.46×10^4	0.347508	9.83×10^4	0.252779
Trigger matching	3.6×10^4	0.334677	3.34×10^4	0.334861	9.22×10^4	0.236902
Bad muon veto	3.56×10^4	0.3306	3.3×10^4	0.330579	9.11×10^4	0.234218
Two tight leptons	3.35×10^4	0.311108	3.1×10^4	0.310941	8.63×10^4	0.221767
Analysis channel	1.41×10^4	0.131348	1.31×10^4	0.131746	2.04×10^4	0.0525597
Charge	1.14×10^4	0.105541	1.06×10^4	0.106281	6.57×10^3	0.0168927
Number of b-jets	9.22×10^3	0.0855938	8.53×10^3	0.0855607	5.56×10^3	0.014294
$m_{\ell\ell}$ SS lead. pair	9.21×10^3	0.085501	8.52×10^3	0.0854604	5.56×10^3	0.0142838
$\Delta R(\ell^{\pm},\ell^{\pm})_{lead.lep.pair}$	9.08×10^3	0.0842751	8.45×10^3	0.0847884	5.39×10^3	0.0138648
Di-lepton p_T, SS lead. pair	8.87×10^3	0.0823621	8.41×10^3	0.0843271	5.04×10^3	0.0129574

Table 4.10: Cut-flow for the two leptons region in the muon channel. In the first column the selection cuts are listed, *Preselection* means that no cut has been applied yet and then corresponds to the total number of events contained in the sample. The other two columns show the number of events remaining after each cut and the relative number of yields. The samples have a common mass point of 1000 GeV.

$e^{\pm}\mu^{\pm}$	$Y^{\pm\pm}$		$H^{\pm\pm}$		$\Delta^{\pm\pm}$	
	Yields	Rel. Yields	Yields	Rel. Yields	Yields	Rel. Yields
Preselection	1.08×10^5	1	9.97×10^4	1	3.89×10^5	1
Number of jets	1.08×10^5	1	9.97×10^4	1	3.89×10^5	1
Two loose leptons	3.75×10^4	0.348356	3.47×10^4	0.347608	9.84×10^4	0.252851
Triggers	3.75×10^4	0.34817	3.46×10^4	0.347508	9.83×10^4	0.252779
Trigger matching	3.6×10^4	0.334677	3.34×10^4	0.334861	9.22×10^4	0.236902
Bad muon veto	3.56×10^4	0.3306	3.3×10^4	0.330579	9.11×10^4	0.234218
Two tight leptons	3.35×10^4	0.311108	3.1×10^4	0.310941	8.63×10^4	0.221767
Analysis channel	3.64×10^3	0.0337936	3.17×10^3	0.0317731	4.03×10^4	0.103572
Charge	294	0.00273024	284	0.00284835	1.33×10^4	0.0341685
Number of b-jets	239	0.00221948	231	0.002316	1.13×10^4	0.0290225
$m_{\ell\ell}$ SS lead. pair	225	0.00208947	215	0.00215632	1.13×10^4	0.0289839
$\Delta R(\ell^{\pm},\ell^{\pm})_{lead.lep.pair}$	220	0.00204303	214	0.00214629	1.1×10^4	0.0282874
Di-lepton p_T, SS lead. pair	167	0.00155085	173	0.00173508	1.03×10^4	0.0264238

Table 4.11: Cut-flow for the two leptons region in the mixed channel. In the first column the selection cuts are listed, *Preselection* means that no cut has been applied yet and then corresponds to the total number of events contained in the sample. The other two columns show the number of events remaining after each cut and the relative number of yields. The samples have a common mass point of 1000 GeV.

$e^{\pm}e^{\pm}e^{\mp}$	$Y^{\pm\pm}$		$H^{\pm\pm}$		$\Delta^{\pm\pm}$	
	Yields	Rel. Yields	Yields	Rel. Yields	Yields	Rel. Yields
Preselection	1.08×10^5	1	9.97×10^4	1	3.89×10^5	1
Number of jets	1.08×10^5	1	9.97×10^4	1	3.89×10^5	1
Three loose leptons	3.39×10^4	0.315222	3.08×10^4	0.308815	1.55×10^5	0.397236
Triggers	3.39×10^4	0.315203	3.08×10^4	0.308805	1.55×10^5	0.397229
Trigger matching	3.38×10^4	0.314265	3.07×10^4	0.307852	1.54×10^5	0.395843
Bad muon veto	3.32×10^4	0.308015	3.01×10^4	0.301734	1.51×10^5	0.388512
Three tight leptons	2.9×10^4	0.269309	2.63×10^4	0.264124	1.36×10^5	0.350861
Analysis channel	6.52×10^3	0.0605295	5.95×10^3	0.0596949	1.95×10^4	0.050123
Charge	6.36×10^3	0.0590158	5.8×10^3	0.0582206	1.9×10^4	0.0488918
Number of b-jets	5.73×10^3	0.053221	5.34×10^3	0.0535469	1.73×10^4	0.0445658
m_{ll} SS lead. pair	5.72×10^3	0.0531374	5.32×10^3	0.0534065	1.73×10^4	0.0445144
Di-lepton p_{T}, SS lead. pair	5.48×10^3	0.0508715	5.24×10^3	0.052554	1.62×10^4	0.0416509
Number of Z bosons (leptonic)	5.42×10^3	0.0503608	5.18×10^3	0.0519121	1.6×10^4	0.0411625

Table 4.12: Cut-flow for the three leptons region in the electron channel. In the first column the selection cuts are listed, *Preselection* means that no cut has been applied yet and then corresponds to the total number of events contained in the sample. The other two columns show the number of events remaining after each cut and the relative number of yields. The samples have a common mass point of 1000 GeV.

$\mu^{\pm}\mu^{\pm}\mu^{\mp}$	$Y^{\pm\pm}$		$H^{\pm\pm}$		$\Delta^{\pm\pm}$	
	Yields	Rel. Yields	Yields	Rel. Yields	Yields	Rel. Yields
Preselection	1.08×10^5	1	9.97×10^4	1	3.89×10^5	1
Number of jets	1.08×10^5	1	9.97×10^4	1	3.89×10^5	1
Three loose leptons	3.39×10^4	0.315222	3.08×10^4	0.308815	1.55×10^5	0.397236
Triggers	3.39×10^4	0.315203	3.08×10^4	0.308805	1.55×10^5	0.397229
Trigger matching	3.38×10^4	0.314265	3.07×10^4	0.307852	1.54×10^5	0.395843
Bad muon veto	3.32×10^4	0.308015	3.01×10^4	0.301734	1.51×10^5	0.388512
Three tight leptons	2.9×10^4	0.269309	2.63×10^4	0.264124	1.36×10^5	0.350861
Analysis channel	7.65×10^3	0.0710233	6.94×10^3	0.069624	1.48×10^4	0.0380883
Charge	7.65×10^3	0.0710233	6.94×10^3	0.069624	1.48×10^4	0.0380883
Number of b-jets	7.18×10^3	0.0666493	6.51×10^3	0.0652712	1.36×10^4	0.0350013
m_{ll} SS lead. pair	7.17×10^3	0.0666029	6.5×10^3	0.0652211	1.36×10^4	0.0349396
Di-lepton p_{T}, SS lead. pair	6.95×10^3	0.0645413	6.46×10^3	0.0647698	1.27×10^4	0.0325954
Number of Z bosons (leptonic)	6.88×10^3	0.0638634	6.36×10^3	0.063827	1.25×10^4	0.0322124

Table 4.13: Cut-flow for the three leptons region in the muon channel. In the first column the selection cuts are listed, *Preselection* means that no cut has been applied yet and then corresponds to the total number of events contained in the sample. The other two columns show the number of events remaining after each cut and the relative number of yields. The samples have a common mass point of 1000 GeV.

$e^{\pm}e^{\pm}\mu^{\mp}$	$Y^{\pm\pm}$		$H^{\pm\pm}$		$\Delta^{\pm\pm}$	
	Yields	Rel. Yields	Yields	Rel. Yields	Yields	Rel. Yields
Preselection	1.08×10^5	1	9.97×10^4	1	3.89×10^5	1
Number of jets	1.08×10^5	1	9.97×10^4	1	3.89×10^5	1
Three loose leptons	3.39×10^4	0.315222	3.08×10^4	0.308815	1.55×10^5	0.397236
Triggers	3.39×10^4	0.315203	3.08×10^4	0.308805	1.55×10^5	0.397229
Trigger matching	3.38×10^4	0.314265	3.07×10^4	0.307852	1.54×10^5	0.395843
Bad muon veto	3.32×10^4	0.308015	3.01×10^4	0.301734	1.51×10^5	0.388512
Three tight leptons	2.9×10^4	0.269309	2.63×10^4	0.264124	1.36×10^5	0.350861
Analysis channel	9.39×10^3	0.0872375	8.52×10^3	0.0854203	5.35×10^4	0.137563
Charge	9.38×10^3	0.0871354	8.51×10^3	0.08532	5.26×10^4	0.135255
Number of b-jets	8.78×10^3	0.0815635	7.91×10^3	0.0793224	4.84×10^4	0.124362
m_{ll} SS lead. pair	8.75×10^3	0.0812663	7.88×10^3	0.0790817	4.83×10^4	0.124166
Di-lepton p_{T}, SS lead. pair	8.44×10^3	0.0783596	7.76×10^3	0.0778581	4.52×10^4	0.116157
Number of Z bosons (leptonic)	8.44×10^3	0.0783503	7.76×10^3	0.0778581	4.5×10^4	0.115779

Table 4.14: Cut-flow for the three leptons region in the mixed channel ($e^{\pm}e^{\pm}\mu^{\mp}$). In the first column the selection cuts are listed, *Preselection* means that no cut has been applied yet and then corresponds to the total number of events contained in the sample. The other two columns show the number of events remaining after each cut and the relative number of yields. The samples have a common mass point of 1000 GeV.

$e^{\mp}\mu^{\pm}\mu^{\pm}$	$Y^{\pm\pm}$		$H^{\pm\pm}$		$\Delta^{\pm\pm}$	
	Yields	Rel. Yields	Yields	Rel. Yields	Yields	Rel. Yields
Preselection	1.08×10^5	1	9.97×10^4	1	3.89×10^5	1
Number of jets	1.08×10^5	1	9.97×10^4	1	3.89×10^5	1
Three loose leptons	3.39×10^4	0.315222	3.08×10^4	0.308815	1.55×10^5	0.397236
Triggers	3.39×10^4	0.315203	3.08×10^4	0.308805	1.55×10^5	0.397229
Trigger matching	3.38×10^4	0.314265	3.07×10^4	0.307852	1.54×10^5	0.395843
Bad muon veto	3.32×10^4	0.308015	3.01×10^4	0.301734	1.51×10^5	0.388512
Three tight leptons	2.9×10^4	0.269309	2.63×10^4	0.264124	1.36×10^5	0.350861
Analysis channel	5.44×10^3	0.0505187	4.92×10^3	0.0493847	4.87×10^4	0.125086
Charge	5.31×10^3	0.0492928	4.8×10^3	0.0481009	4.82×10^4	0.123955
Number of b-jets	4.8×10^3	0.0445846	4.34×10^3	0.0435476	4.42×10^4	0.113532
m_{ll} SS lead. pair	4.78×10^3	0.0443896	4.33×10^3	0.0434172	4.41×10^4	0.113391
Di-lepton p_{T}, SS lead. pair	4.59×10^3	0.0426158	4.27×10^3	0.0428556	4.12×10^4	0.105903
Number of Z bosons (leptonic)	4.59×10^3	0.0426158	4.27×10^3	0.0428556	4.1×10^4	0.105359

Table 4.15: Cut-flow for the three leptons region in the mixed channel ($e^{\mp}\mu^{\pm}\mu^{\pm}$). In the first column the selection cuts are listed, *Preselection* means that no cut has been applied yet and then corresponds to the total number of events contained in the sample. The other column shows the number of events remaining after each cut and the relative number of yields. The samples have a common mass point of 1000 GeV.

$\ell^{\pm}\ell^{\pm}\ell^{\mp}\ell^{\mp}$	$Y^{\pm\pm}$		$H^{\pm\pm}$		$\Delta^{\pm\pm}$	
	Yields	Rel. Yields	Yields	Rel. Yields	Yields	Rel. Yields
Preselection	1.08×10^5	1	9.97×10^4	1	3.89×10^5	1
Number of jets	1.08×10^5	1	9.97×10^4	1	3.89×10^5	1
Four loose leptons	2.96×10^4	0.274667	2.85×10^4	0.285456	1.21×10^5	0.310608
Triggers	2.96×10^4	0.274667	2.85×10^4	0.285456	1.21×10^5	0.310608
Trigger matching	2.96×10^4	0.274658	2.85×10^4	0.285446	1.21×10^5	0.310585
Bad muon veto	2.88×10^4	0.266997	2.77×10^4	0.277413	1.18×10^5	0.302586
Four tight leptons	2.53×10^4	0.234596	2.43×10^4	0.244185	1.04×10^5	0.267472
Analysis channel	2.53×10^4	0.234596	2.43×10^4	0.244185	1.04×10^5	0.267472
Charge	2.35×10^4	0.218215	2.26×10^4	0.227095	9.81×10^4	0.252211
Number of b-jets	2.26×10^4	0.209634	2.17×10^4	0.218029	9.45×10^4	0.242783
Average SS m_{ll}	2.26×10^4	0.209597	2.17×10^4	0.218009	9.44×10^4	0.242765
Number of Z bosons (leptonic)	2.24×10^4	0.207582	2.16×10^4	0.216183	9.35×10^4	0.240225

Table 4.16: Cut-flow for the three leptons region in the mixed channel ($\ell^{\pm}\ell^{\pm}\ell^{\mp}\ell^{\mp}$). In the first column the selection cuts are listed, *Preselection* means that no cut has been applied yet and then corresponds to the total number of events contained in the sample. The other column shows the number of events remaining after each cut and the relative number of yields. The samples have a common mass point of 1000 GeV

4.4 Systematic uncertainties

By systematic uncertainties we are referring to both the experimental and theoretical uncertainties sources affecting background and signal predictions. The systematic uncertainties can affect both the distribution shape and the total event yields of all the signal samples used in the fit. In Table 4.17 a list of the systematic uncertainties taken in account in our analysis is reported.

4.4.1 Experimental uncertainties

For the most part, the experimental uncertainties are related to the differences between reconstruction results of data and simulated events. One can classify them into two main types:

- **Calibration uncertainties** change particle momenta to account for uncertainties in momentum scale and track reconstruction.
- **Efficiency uncertainties** are due to different reconstruction, object identification, charge identification, isolation and trigger efficiencies of leptons in data compared with MC simulation. These are quantified by varying the corresponding scale-factors applied to MC events by 1σ up and down.

Both the charge mis-identification probability, which arises from the statistical uncertainty on the $Z/\gamma^* \to ee$ sample in the selected kinematic region, and fake factor measurements carry their systematic uncertainties:

- *charge-flip background*
  - the uncertainty given by the likelihood fit propagates from the rate to the scale factors which are then varied to obtain the final statistical uncertainty on the charge-flip background prediction.
  - the uncertainty due to the mass range selected to identify the Z peak.
- *fake lepton background*
  - the uncertainties are evaluated by varying the nominal fake factor.

The analysis is also affected by the finite number of both simulated and data events, then a significant contribution arises from the statistical uncertainty in the MC samples.

Systematic uncertainty	Effect	Affected MC Samples
Luminosity	norm.	all
Experimental uncertainties	shape + norm.	all
Electron scale and resolution	shape + norm.	all
Electron reconstruction efficiencies	shape + norm.	all
Electron identification efficiencies	shape + norm.	all
Electron charge id. efficiencies	shape + norm.	all
Electron isolation efficiencies	shape + norm.	all
Electron trigger efficiencies	shape + norm.	all
Muon scale and resolution	shape + norm.	all
Muon reconstruction efficiencies	shape + norm.	all
Muon track-to-vertex association efficiencies	shape + norm.	all
Muon trigger efficiencies	shape + norm.	all
Jet energy scale - calibration	shape + norm.	all
Jet energy scale - flavour dependence	shape + norm.	all
Jet energy scale - pile-up dependence	shape + norm.	all
Jet energy scale - calorimeter punch-through	shape + norm.	all
Jet energy scale - MC non-closure	shape + norm.	all
Jet JVT efficiencies	shape + norm.	all
Jet flavour tagging efficiencies	shape + norm.	all
MET uncertainties	shape + norm.	all

Table 4.17: Summary of systematic effects considered in the analysis. The first column corresponds to the source of systematic uncertainty, the second one shows the effect of the systematic uncertainty (normalization/shape), and the last column lists MC samples affected by the systematic effect.

4.5 Statistical Analysis and Results

The statistical interpretation of data relies on two hypotheses: they can be in agreement with the SM background only case or prove to be consistent with the background plus signal hypothesis at a certain confidence level.
To carry out the statistical analysis we used the HistFitter [59] framework, which is extensively employed by the ATLAS Collaboration for statistical interpretation. This package configures and builds parametric model to describe the observed data and the MC simulations to perform an hypothesis test. Thanks to the different fit configurations provided it allows to study eventual data excess and to set upper limit on the production cross-section as function of the mass.
The core of the hypothesis test is the likelihood function (LH) (4.3) in which the probability distributions for the different regions defined in the analysis are encoded. Since the control regions (CRs) and the signal regions (SRs) are statistically independent they can be modeled by separate PDFs and combined into a simultaneous fit. Inside the LH function the parameter considered are divided into *parameters of interest* (POI) and *nuisance parameters* (NPs). The POI is the signal strength μ, which one wants to extract, the value $\mu = 0$ corresponds to the background only hypothesis while $\mu = 1$ represents the signal plus background hypothesis. The uncertainties enter the likelihood function as nuisance parameters. Both the POI and NPs true values are unknown and are estimated by maximizing the LH in the fit, returning their most likely values.

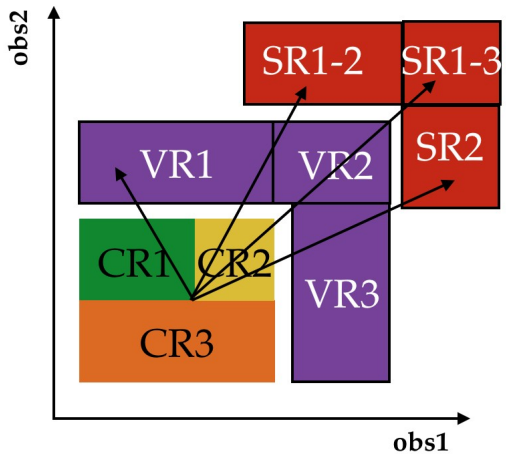

Figure 4.2: Schematic view of an analysis strategy with multiple control, validation and signal regions. The extrapolation from the control to the signal regions is verified in the validation regions that lie in the extrapolation phase space

The analysis strategy is based on two different type of fit. The first one to be considered is the *background only fit* which is only performed in the CRs. The output of this

first step are the *normalization factors* computed for the dominant background processes and are then applied to the VRs and SRs, see Subsection 4.6.1. In a second time the *model-dependent signal fit* is carried out. In this case both the CRs and the SRs are used to set exclusion limits on the signal model. In Figure 4.2 a schematic representation of how the fitting strategy operates over the analysis region is provided. The discriminant variables used throughout the analysis are:

- `mass2lOS1`: the invariant mass or the opposite-sign leading lepton pairs, it is used as discriminating variable in the OCCR;
- `mass2lSS1`: the invariant mass of the same-sign leading lepton pair in the two- and three-lepton regions;
- `mass4lAvg`: the mean invariant mass defined as $\bar{M} = (m^{--} + m^{++})/2$ where $m^{\pm\pm}$ are the invariant masses of the same-sign pairs.

The Likelihood Function

The likelihood function computed by HistFitter is defined as:

$$\begin{aligned}\mathcal{L}(\boldsymbol{n}, \boldsymbol{\theta_0}|\mu_{sig}; \boldsymbol{\mu_b}, \boldsymbol{\theta}) &= P_{SR} \times P_{CR} \times G_{NP} \\ &= P\left(n_{SR}|\mu_{sig} \cdot S(\boldsymbol{\theta}) + \sum_{b}^{bkgs} \mu_b B(\boldsymbol{\theta})\right) \\ &\times \prod_{i \in CR} P\left(n_{CR}|\sum_{b}^{bkgs} \mu_b B(\boldsymbol{\theta})\right) \\ &\times G_{NPs}(\boldsymbol{\theta_0}|\boldsymbol{\theta}).\end{aligned} \tag{4.3}$$

The first term, P_{SR}, corresponds to the poissonian probability to observe n events given the signal plus background hypothesis

$$n_{expected} = \mu_{sig} \cdot S(\boldsymbol{\theta}) + \mu_b \cdot B(\boldsymbol{\theta}), \tag{4.4}$$

where $S(\theta)$ and $B(\theta)$ are, respectively, the pdf for signal and background as functions of the NPs θ; n_{SR} is the number of events observed in the signal region while μ_b and μ_{sig} are the normalization factors for background and signal. The second term in (4.3) is related to the CR and it is a product over the number of CRs used to describe the variable entering the fit. The third term describes the parametrization for the nuisance parameters and constrains the *auxiliary measurements* θ_0 to its real measured value θ. The functions G_{NPs} can be of gaussian or poisson type. Systematic uncertainties are nominally described by gaussian auxiliary measurements, such as luminosity or experimental systematic uncertainties while poissonian functions are preferred to describe statistical uncertainties.

Hypothesis Test

The hypothesis test use the frequentist *profile likelihood ratio* q_μ as test statistic to obtain the expected 95% *confidence level* (CL) limit on the considered mass hypothesis for signal events and it is defined as:

$$q_\mu = -2 \cdot \ln \frac{\mathcal{L}(\mu, \hat{\theta}_\mu)}{\mathcal{L}(\hat{\mu}, \hat{\theta})} \tag{4.5}$$

where $\hat{\mu}$ and $\hat{\theta}$ maximize the likelihood function and $\hat{\theta}_\mu$ maximize the likelihood function for the specific value of the signal strength μ. A q_μ close to zero suggests a signal-like data distributions while a larger q_μ a background-like data distributions.
The *p-value*, assigned to a hypothesis test, is evaluated using a distribution of the test statistic $f(q_\mu|\text{hypothesis})$. The p-values corresponding to a background only hypothesis, p_B, and corresponding to a signal plus background hypothesis, p_{S+B}, for an observed value of the test-statistic $q_{\mu.obs}$, are defined as:

$$p_B = \int_{-\inf}^{q_{\mu,obs}} f(q_\mu|B)\, dq_\mu \tag{4.6}$$

$$p_{S+B} = \int_{q_{\mu,obs}}^{\inf} f(q_\mu|S+B)\, dq_\mu \tag{4.7}$$

The final confidence level CLs is computed as the ratio:

$$CLs = \frac{p_{S+B}}{1 - p_B} \tag{4.8}$$

where p_{S+B} and p_B are computed with the same $q_{\mu,obs}$. If the ratio is below 5% it allows to exclude a hypothesis at 95%.

4.5.1 Background normalization

As previously stated, the main background processes are estimated with MC simulations. The agreement between observed data and the MC simulation is expressed by the ratio $data/MC$ which we would like to be equal to 1. For this reason the *background only fit* is performed leading to the scaling of the initial MC prediction to the observed value in the CRs through the normalization factors. In Table 4.18 the normalization factors for the Drell-Yan and diboson background are listed.
After a normalized background has been obtained, an extrapolation procedure is carried out. For each normalized background process in SR and in CR a *transfer factor* defined as the ratio of expected event counts is used to convert the observations in the CRs into estimates in the SRs:

$$N_p(SR, \text{est.}) = N_p(CR, \text{obs.}) \times \left[\frac{MC_p(SR, \text{raw})}{MC_p(CR, \text{raw})}\right] = \mu_p \times MC_p(SR, \text{raw}), \tag{4.9}$$

where $N_p(SR, \text{est.})$ is the background estimate for the process p in the SR, $N_p(CR, \text{obs.})$ corresponds to the observed number of data events in the CR for the process p, then the unnormalized contributions for the process p in SR and CR from the MC simulation are $MC_p(SR, \text{raw})$ and $MC_p(CR, \text{raw})$: their ratio is the transfer factor. The normalization factor actually resulting from the fit to data is μ_p.

Background	Normalization Region	Normalization Factor
Drell-Yan	OCCR	1.0331 ± 0.0018
Diboson ($e^{\pm}e^{\pm}e^{\mp}$)	DBCR	0.85 ± 0.04
Diboson ($e^{\pm}e^{\pm}\mu^{\mp}$)	DBCR	0.80 ± 0.03
Diboson ($e^{\mp}\mu^{\pm}\mu^{\mp}$)	DBCR	0.90 ± 0.04
Diboson ($\mu^{\pm}\mu^{\pm}\mu^{\mp}$)	DBCR_60	0.95 ± 0.03
Diboson ($l^{\pm}l^{\pm}l^{\mp}l^{\mp}$)	CR4L	1.18 ± 0.03

Table 4.18: Background only fit results for the main backgrounds. The middle column shows the normalization region employed.

Another important aspect of the background only fit is that it gives a way to assess the effect of systematic uncertainties, cited in Section 4.4, through the *pull plot* in Figure 4.3. This plot shows the result of the fit where the systematic uncertainties in Tab 4.17 are constrained using data in control region. The systematic uncertainties are treated as a $\pm 1\sigma$ variation from the nominal value, their values after the fit should still be contained in the $\pm\sigma$ band if they do not impact much on the fit results. The plot in Figure 4.3 has been obtained using a background only fit where all the control regions are considered: all the systematic uncertainties show a minimal variation with respect to the dashed line, meaning the pre- and post-fit values are in agreement and the error bars lay inside $\pm 1\sigma$ interval.

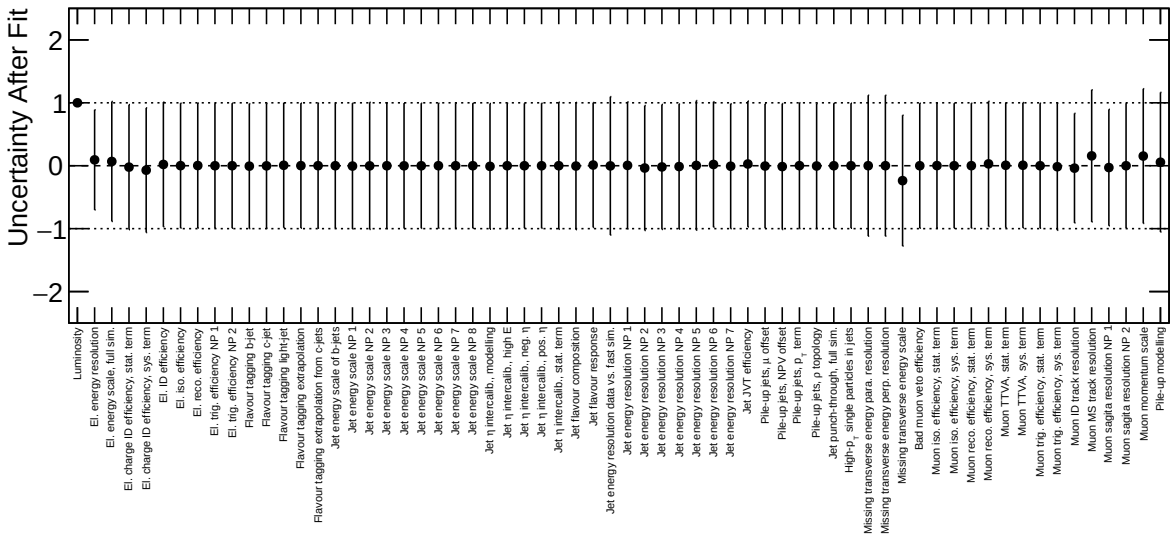

Figure 4.3: Systematic pulls in the fit showing the relative difference compared to the nominal prediction. Values between -1 and 1 indicate the one standard deviation band of the uncertainty. The systematic uncertainty related to the Luminosity is automatically set to 1 because the background are normalized to its value.

Figure 4.4-4.17 show the resulting plots before and after the background only fit. The normalization effect on the background is clearly evident in both control and signal regions.

OCCR

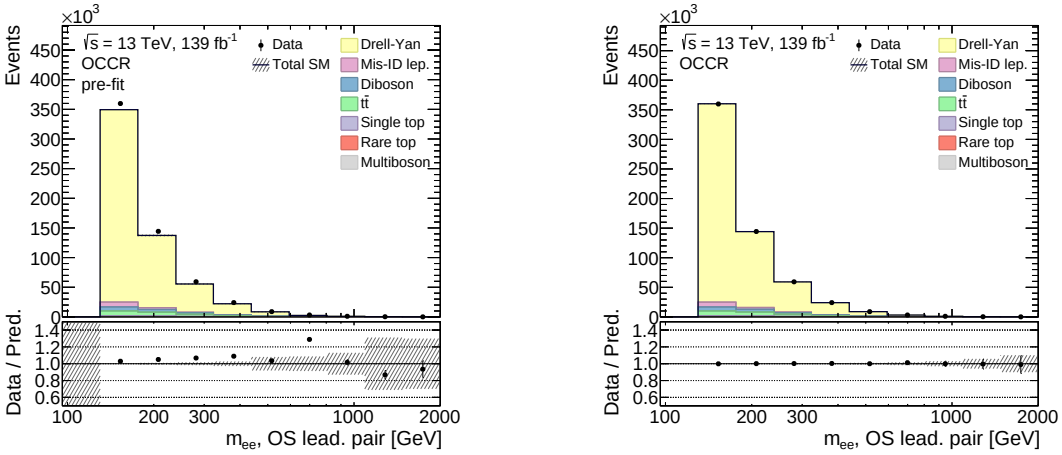

(a) (b)

Figure 4.4: Opposite-charge control region (a) before and (b) after the fit normalization, the variable plotted is the invariant mass of the opposite charge electron leading pair.

DBCR

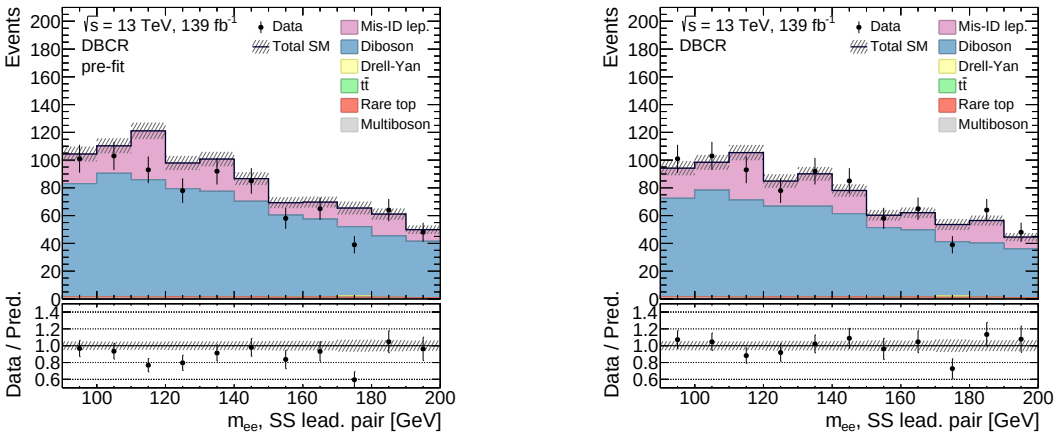

(a) (b)

Figure 4.5: Diboson control region (a) before and (b) after the fit normalization for the $e^{\pm}e^{\pm}e^{\mp}$ channel, the variable plotted is the invariant mass of the same charge electron leading pair.

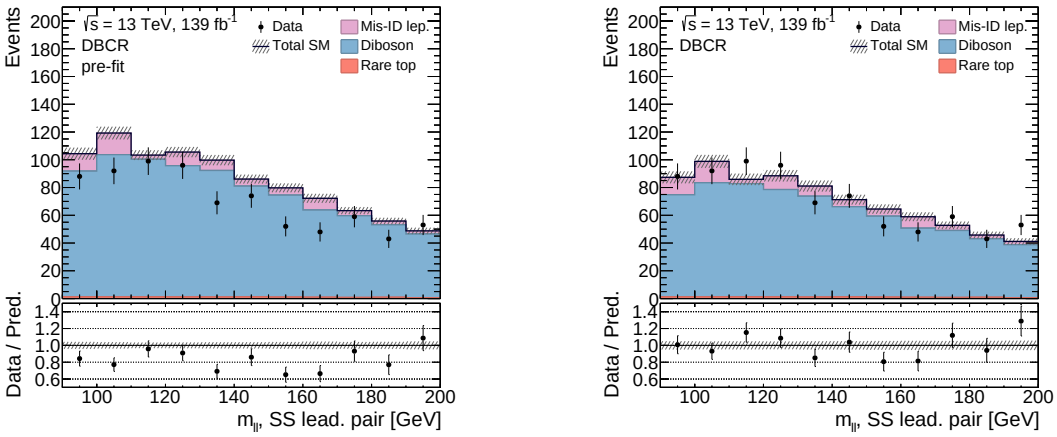

(a) (b)

Figure 4.6: Diboson control region (a) before and (b) after the fit normalization for the $e^{\pm}e^{\pm}\mu^{\mp}$ channel, the variable plotted is the invariant mass of the same charge lepton leading pair.

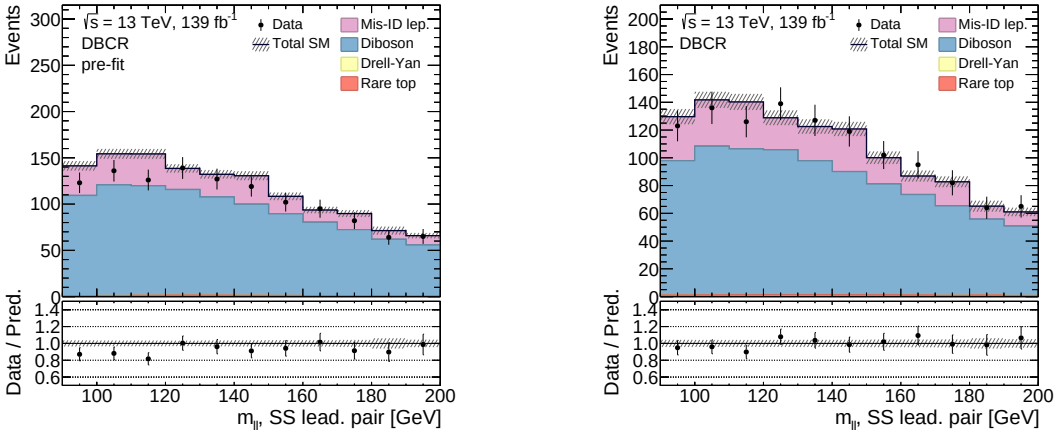

(a) (b)

Figure 4.7: Diboson control region (a) before and (b) after the fit normalization for the $e^{\pm}\mu^{\mp}\mu^{\mp}$ channel, the variable plotted is the invariant mass of the same charge lepton leading pair.

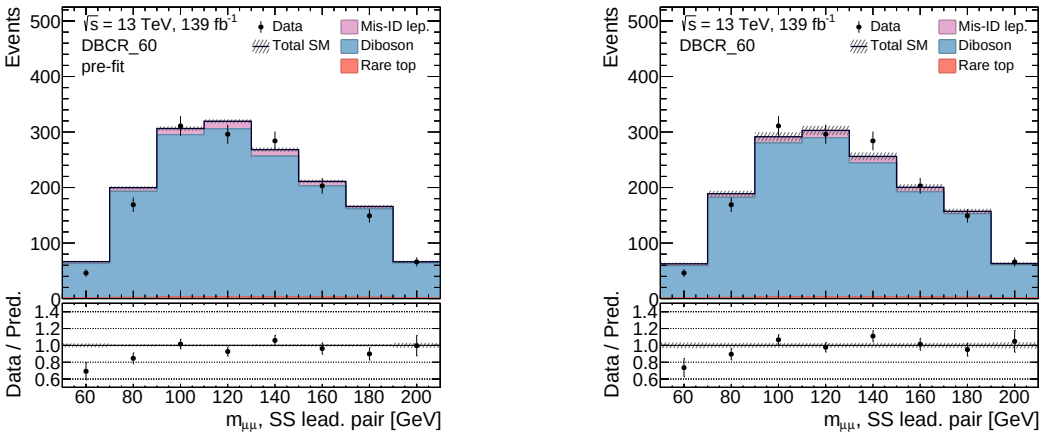

(a) (b)

Figure 4.8: Diboson control region (a) before and (b) after the fit normalization for the $\mu^{\pm}\mu^{\pm}\mu^{\mp}$ channel, the variable plotted is the invariant mass of the same charge muon leading pair.

4LCR

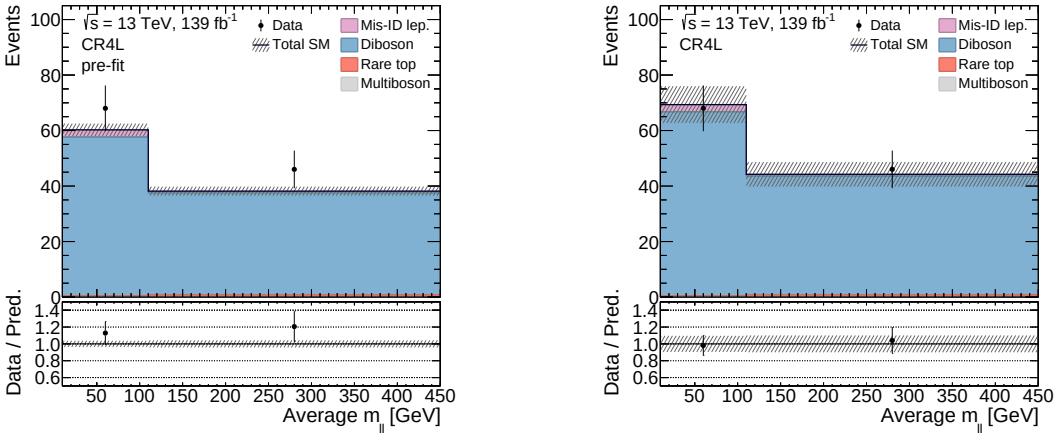

(a) (b)

Figure 4.9: Four-lepton control region (a) before and (b) after the normalization, the variable plotted is the mean of the invariant mass of the same charge lepton pairs: $\bar{M} = \frac{m^{++}+m^{--}}{2}$.

SR 1P2L

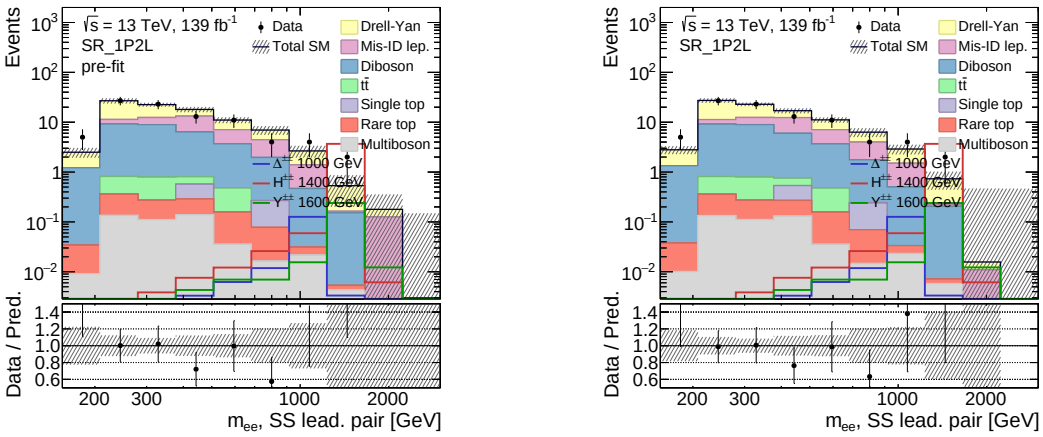

(a) (b)

Figure 4.10: Two leptons Signal Region (a) before and (b) after the fit normalization, channel $e^{\pm}e^{\pm}$, the variable plotted is the invariant mass of the same charge electron leading pair.

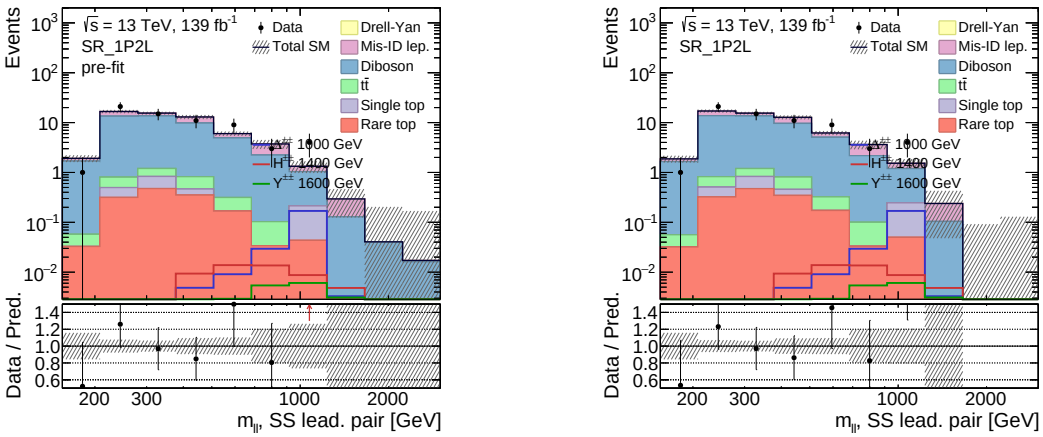

(a) (b)

Figure 4.11: Two leptons Signal Region (a) before and (b) after the fit normalization, channel $e^{\pm}\mu^{\pm}$, the variable plotted is the invariant mass of the same charge lepton leading pair.

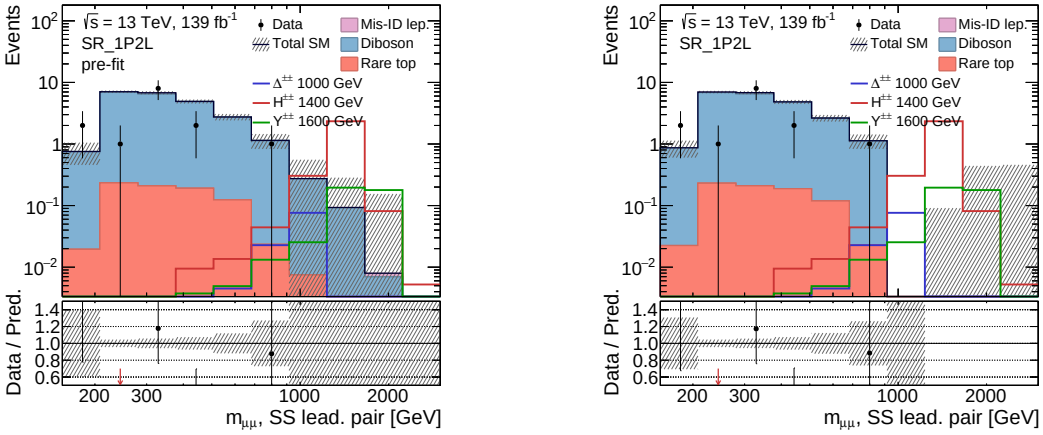

Figure 4.12: Two leptons Signal Region (a) before and (b) after the fit normalization, channel $\mu^{\pm}\mu^{\pm}$, the variable plotted is the invariant mass of the same charge muon leading pair.

SR 1P3L

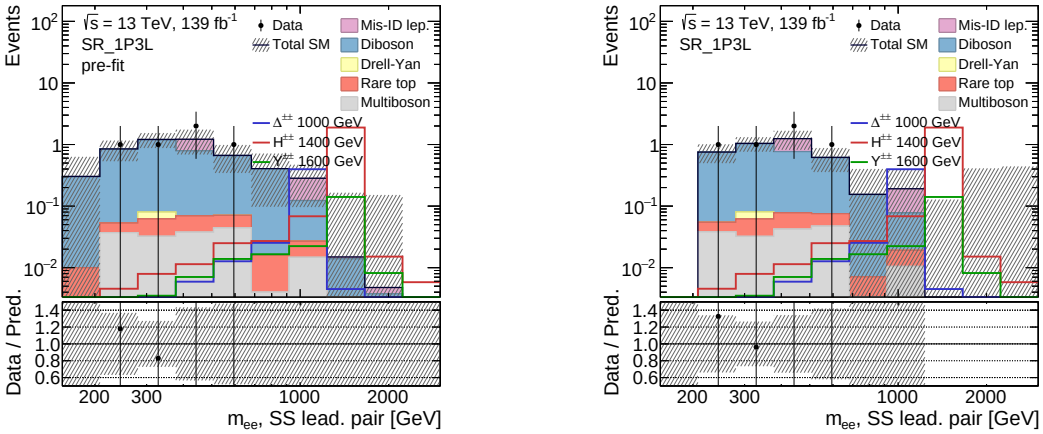

Figure 4.13: Three leptons Signal Region (a) before and (b) after the fit normalization, channel $e^{\pm}e^{\pm}e^{\mp}$, the variable plotted is the invariant mass of the same charge electron leading pair.

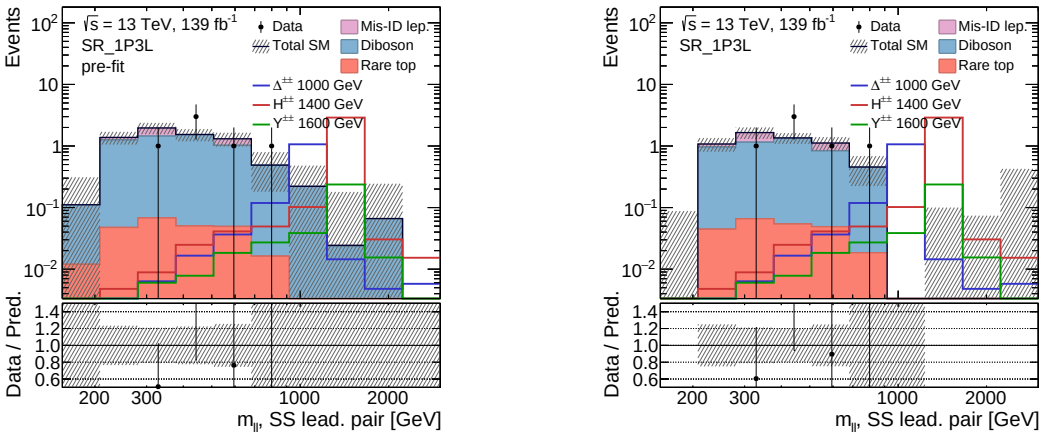

(a) (b)

Figure 4.14: Three leptons Signal Region (a) before and (b) after the fit normalization, channel $e^{\pm}e^{\pm}\mu^{\mp}$, the variable plotted is the invariant mass of the same charge lepton leading pair.

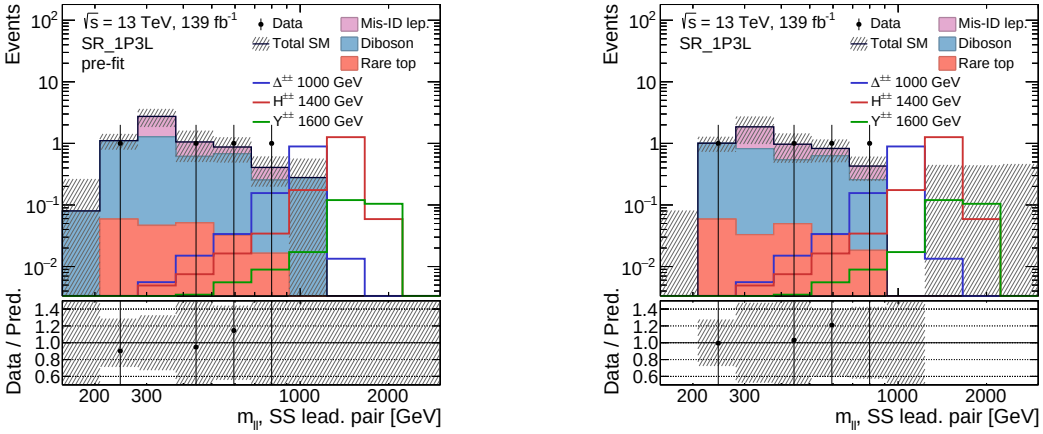

(a) (b)

Figure 4.15: Three leptons Signal Region (a) before and (b) after the fit normalization, channel $e^{\mp}\mu^{\pm}\mu^{\pm}$, the variable plotted is the invariant mass of the same charge lepton leading pair.

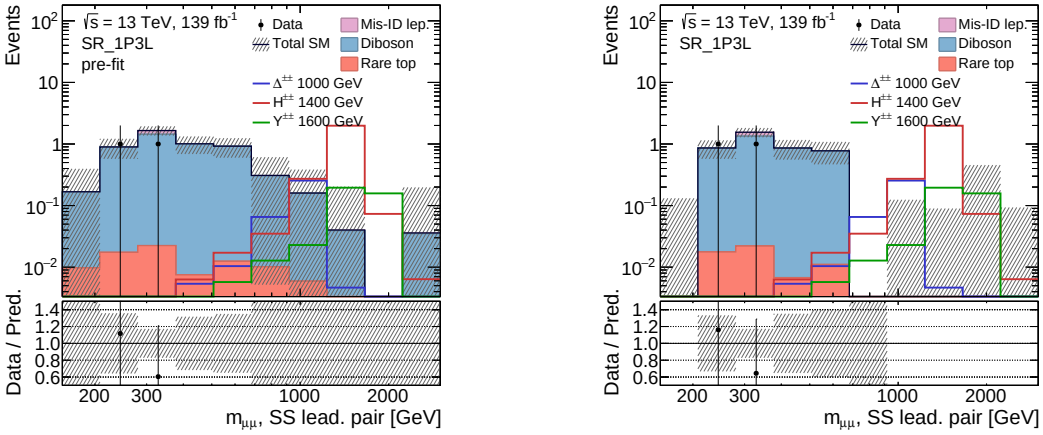

(a) (b)

Figure 4.16: Three leptons Signal Region (a) before and (b) after the fit normalization, channel $\mu^{\pm}\mu^{\pm}\mu^{\mp}$, the variable plotted is the the invariant mass of the same charge lepton leading pair.

SR 2P4L

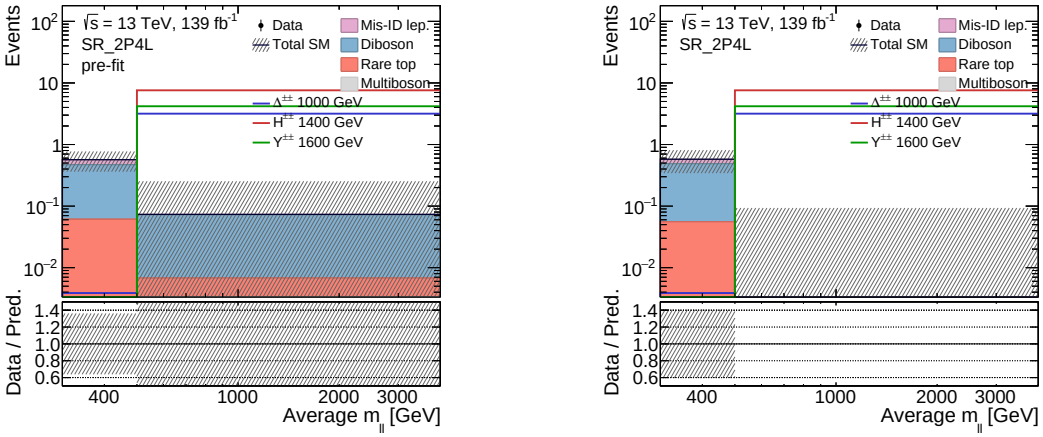

(a) (b)

Figure 4.17: Four leptons Signal Region (a) before and (b) after the fit normalization, inclusive channel $\ell^{\pm}\ell^{\pm}\ell^{\mp}\ell^{\mp}$, the variable plotted is the mean of the invariant mass of the same charge lepton pairs: $\bar{M} = \frac{m^{++}+m^{--}}{2}$.

4.5.2 Exclusion Fit

No significant excesses of experimental data over SM background have been observed and therefore a lower limit on the particle mass and an upper limit on the production cross section are set. To do so, an exclusion fit is performed using the signal regions under the hypothesis of a signal strength parameter μ. In Figure 4.18 the exclusion limit at 95% of CL for the $Y^{\pm\pm}$ is shown: the red line corresponds to the theoretical cross with the section for the $Y^{\pm\pm}$ to be produced with a certain mass; the dotted line is the expected cross section with the $\pm 1\sigma$ (green) and $\pm 2\sigma$ (yellow) error bands; the continuous black line is the observed cross section limit obtained when the data are included in the signal region. To produce the plot in Figure 4.18, the signal regions were split into separate channels and then fitted simultaneously to improve the signal and background discrimination. The point in which the theoretical cross-section crosses the expected (observed) limit sets the expected (observer) lower mass limit on the $Y^{\pm\pm}$ and the corresponding cross-section limit:

$$\text{expected: } m_{Y^{\pm\pm}} < 1642 \text{ GeV are excluded at 95\% CL.} \tag{4.10}$$

$$\text{observed: } m_{Y^{\pm\pm}} < 1637 \text{ GeV are excluded at 95\% CL.} \tag{4.11}$$

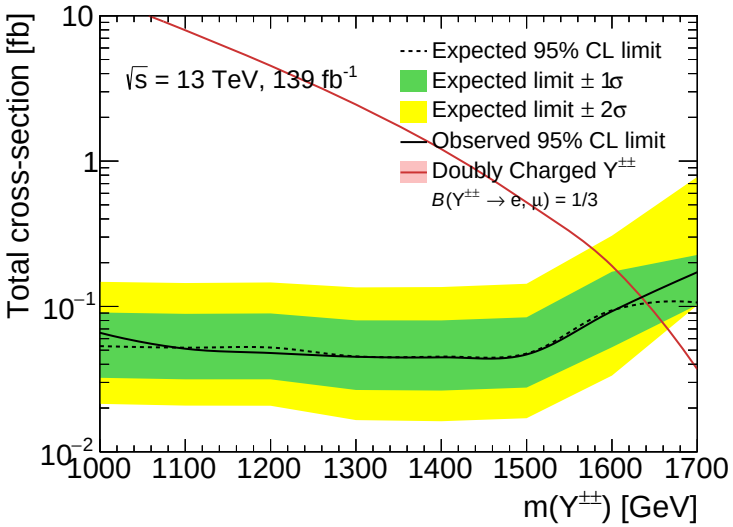

Figure 4.18: Exclusion limit at 95% CL for doubly charged vector bosons $Y^{\pm\pm}$.

Likewise the procedure followed to extract the exclusion limit for the $Y^{\pm\pm}$, each channel in the SRs was considered separately and then combined in the same fit to produce the plot in Figure 4.19 for the $\Delta^{\pm\pm}$ boson. The result obtained is an exclusion

limit at 95% of CL for masses

$$\text{expected: } m_{\Delta^{\pm\pm}} < 1060 \text{ GeV are excluded with 95\% of CL.} \tag{4.12}$$

$$\text{observed: } m_{\Delta^{\pm\pm}} < 1080 \text{ GeV are excluded with 95\% of CL.} \tag{4.13}$$

which is compatible with the previous exclusion limit around 1 TeV obtained by [26].

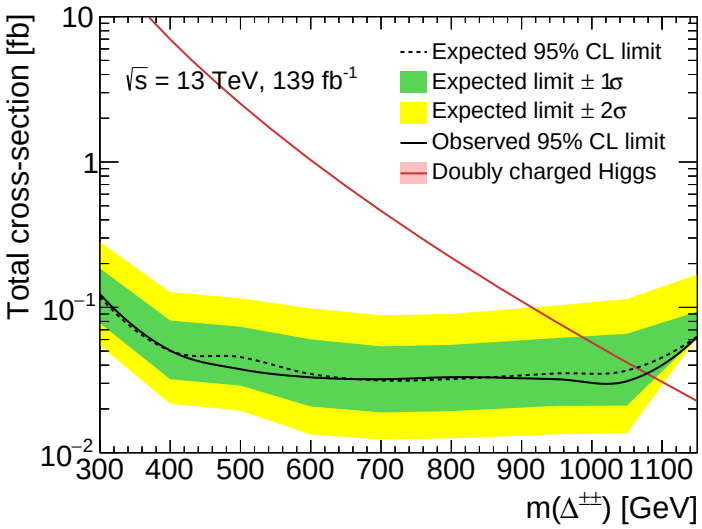

Figure 4.19: Exclusion limit at 95% CL for doubly charged Higgs boson $\Delta^{\pm\pm}$.

We also report in Figure 4.20 the upperlimit on the cross section for $H^{\pm\pm}$ bosons. Here, however, the lack of large mass MC samples prevent us to set a lower limit on the mass, which lays beyond 1500 GeV.

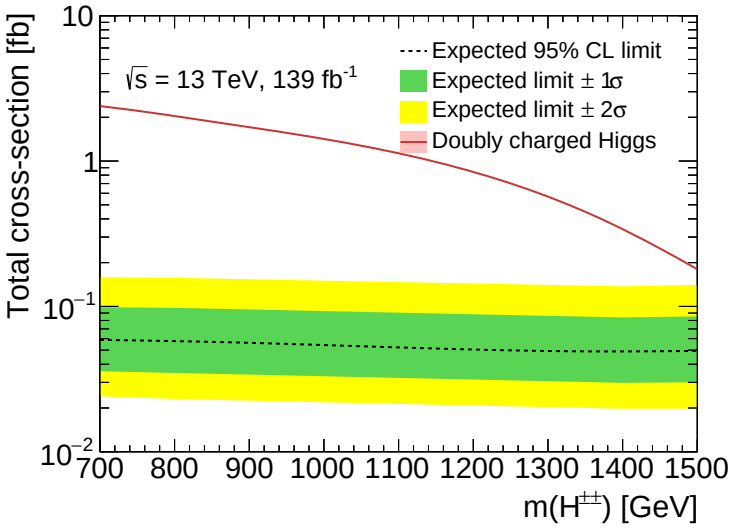

Figure 4.20: Exclusion limit at 95% CL for doubly charged scalar bosons $H^{\pm\pm}$.

4.6 Conclusions

This work is based on the study of doubly charged bosons predicted by the 3-3-1 model and the LRSM. The analysis is performed with the data collected during the Run 2 period by the ATLAS experiment at a centre-of-mass energy of 13 TeV corresponding to 139 fb^{-1} of integrated luminosity. The considered process is

$$pp \to H^{++}H^{--}(Y^{++}Y^{--}, \Delta^{++}\Delta^{--}) \to \ell^+\ell^+\ell'^-\ell'^-$$

where the bosons promptly decay into highly energetic light leptons ($\ell, \ell' = e, \mu$), the final state being composed by two same-sign same-flavour lepton pairs since lepton flavour violation is not allowed within the 3-3-1 model. This study enlarges and complements the already existing analysis by ATLAS of doubly charged Higgs bosons from LRSM. This is the first time a dedicate experimental analysis excludes doubly charge vector bosons in the TeV region. The signals associated to each particle were searched in three analysis regions defined on the basis of the lepton multiplicity in the final state and optimized by cutting on some kinematic variables, such as the p_T and the invariant mass of the same-sign lepton leading pair. The exclusion limit was performed considering many channel/analysis regions configurations, the results presented were obtained using all the analysis regions where the channel were split by lepton flavour since it showed a better sensitivity to the signal events. We set the lower limits:

expected: $m_{Y^{\pm\pm}} < 1642$ GeV are excluded at 95% CL.

observed: $m_{Y^{\pm\pm}} < 1637$ GeV are excluded at 95% CL.

for the $Y^{\pm\pm}$ vector doubly charged boson predicted by the Bilepton model. This is the first experimental limit set on doubly charged vector bosons so far.

expected: $m_{\Delta^{\pm\pm}} < 1060$ GeV are excluded at 95% CL.

observed: $m_{\Delta^{\pm\pm}} < 1080$ GeV are excluded at 95% CL.

for the $\Delta^{\pm\pm}$ doubly charged Higgs boson of the LRSM, the limit resulted in agreement with the previous exclusion limit around 1 TeV.

Appendix A

Validation plots and kinematic variables

In this section we present a first set of histograms obtained throughout the analysis. To validate the cuts on variables, listed in the previous section (see Tab. 4.8), the histograms below are shown. Each histogram contains all three signals: $\Delta^{\pm\pm}$, $Y^{\pm\pm}$ and $H^{\pm\pm}$, plotted respectively for the mass points 1000 GeV 1400 GeV and 1600 GeV. This choice to use different mass points depending on the particle is due to the different magnitude of the crosse section. For each region, also the cuts effect on the specific channel is reported, except the four-lepton signal region where only the inclusive flavour has been used in the analysis.

A.0.1 Validation plots for $\Delta^{\pm\pm}$, $Y^{\pm\pm}$ and $H^{\pm\pm}$ signals

Two and Three-lepton signal regions

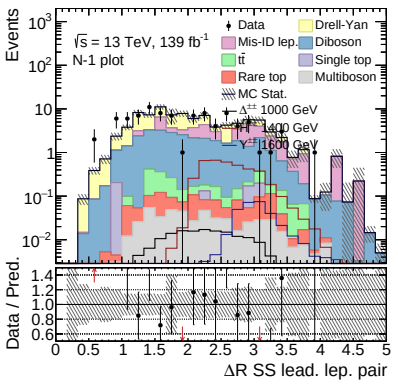

(a)

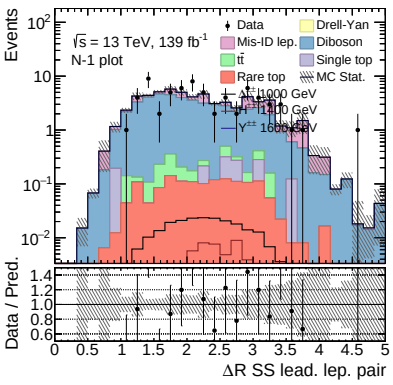

(b)

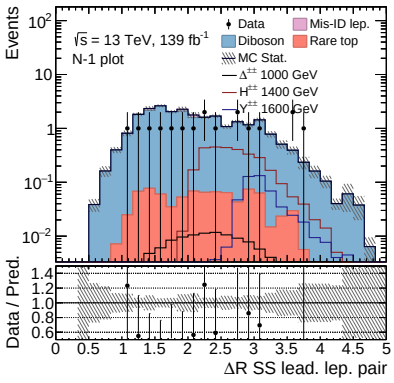

(c)

Figure A.1: SR_1P2L validation plots for the cut $\Delta R(l^{\pm}, l^{\pm}) < 3.5$ where the signals for $\Delta^{\pm\pm}$ (1000 Gev), $Y^{\pm\pm}$ (1600 GeV) and $H^{\pm\pm}$ (1400 GeV) are shown. The distribution (a) refers to the electron channel ($e^{\pm}e^{\pm}$); (b) refers to the mixed channel ($e^{\pm}\mu^{\pm}$); (c) refers to the muon channel ($\mu^{\pm}\mu^{\pm}$).

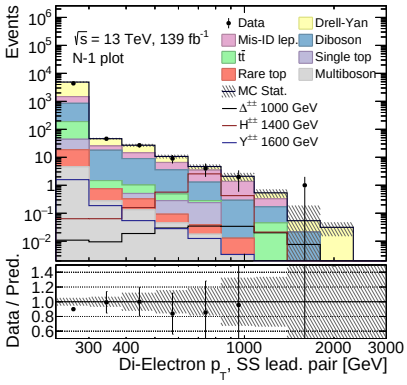

(a)

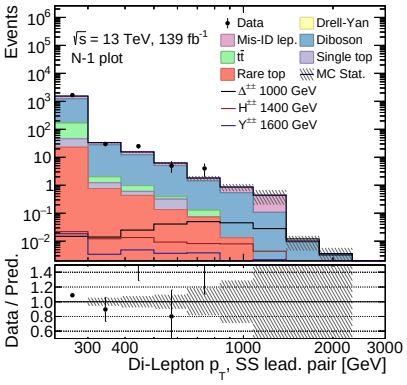

(b)

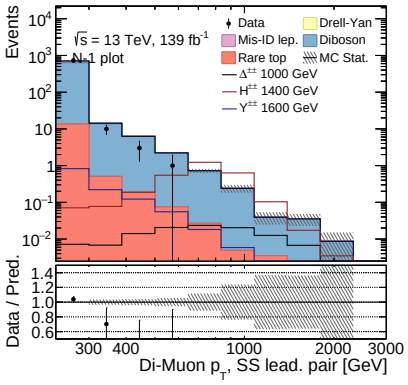

(c)

Figure A.2: SR_1P2L validation plots for the cut $p_T(l^{\pm}, l^{\pm})$ SS lead. > 300 GeV where the signals for $\Delta^{\pm\pm}$ (1000 Gev), $Y^{\pm\pm}$ (1600 GeV) and $H^{\pm\pm}$ (1400 GeV) are shown. The distribution (a) refers to the electron channel ($e^{\pm}e^{\pm}$); (b) refers to the mixed channel ($e^{\pm}\mu^{\pm}$); (c) refers to the muon channel ($\mu^{\pm}\mu^{\pm}$).

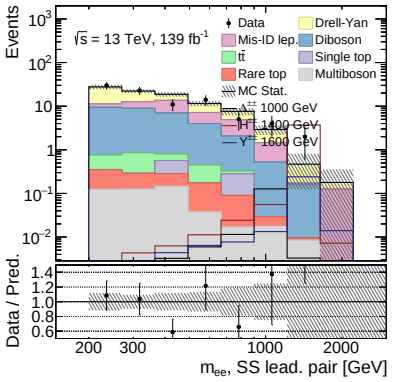

(a)

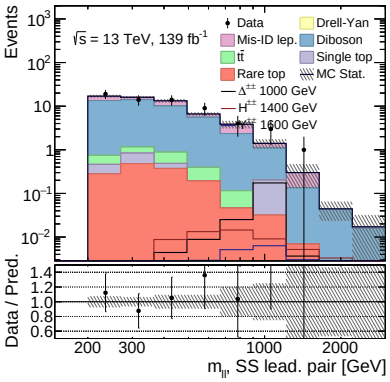

(b)

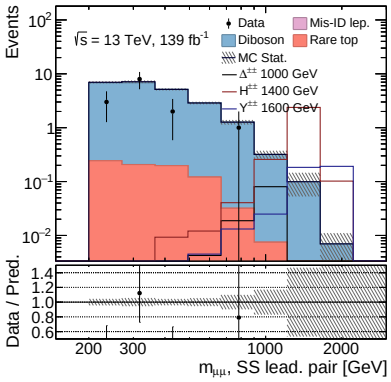

(c)

Figure A.3: SR_1P2L validation plots for the cut $m(l^{\pm}, l^{\pm})$ SS lead. $>$ 200 GeV where the signals for $\Delta^{\pm\pm}$ (1000 GeV), $Y^{\pm\pm}$ (1600 GeV) and $H^{\pm\pm}$ (1400 GeV) are shown. The distribution (a) refers to the electron channel ($e^{\pm}e^{\pm}$); (b) refers to the mixed channel ($e^{\pm}\mu^{\pm}$);(c) refers to the muon channel ($\mu^{\pm}\mu^{\pm}$).

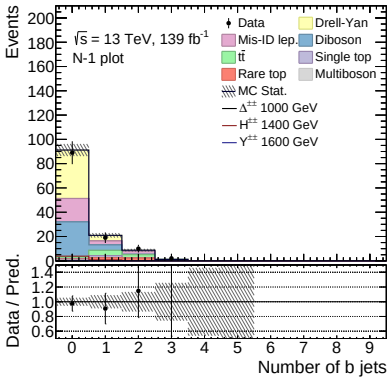

(a)

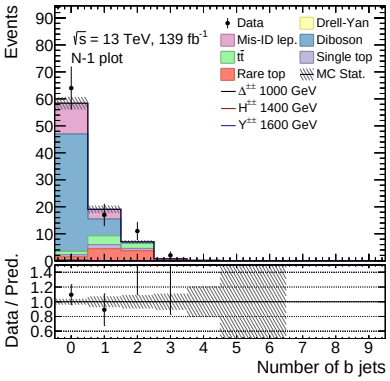

(b)

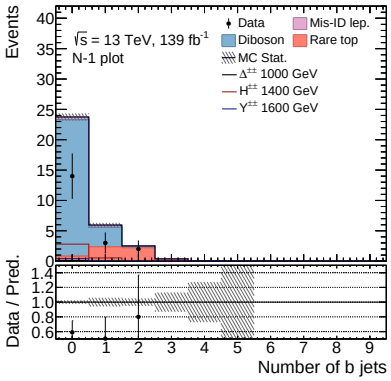

(c)

Figure A.4: SR_1P2L validation plots for the cut *number of b-jets*= 0 where the signals for $\Delta^{\pm\pm}$ (1000 Gev), $Y^{\pm\pm}$ (1600 GeV) and $H^{\pm\pm}$ (1400 GeV) are shown. The distribution in (a) refers to the electron channel ($e^{\pm}e^{\pm}$); (b) refers to the mixed channel ($e^{\pm}\mu^{\pm}$); (c) refers to the muon channel ($\mu^{\pm}\mu^{\pm}$).

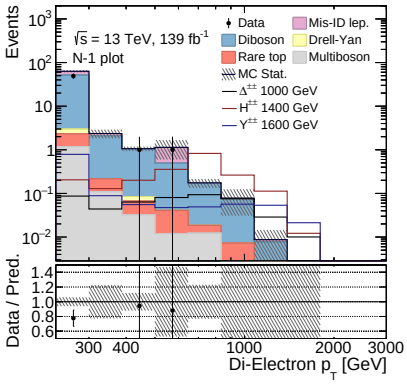

(a)

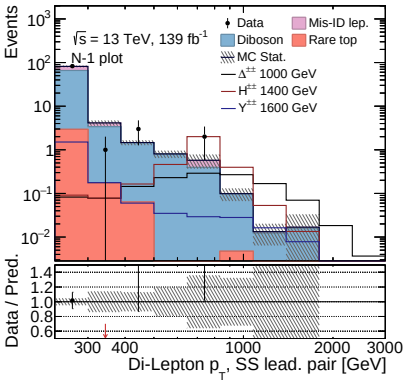

(b)

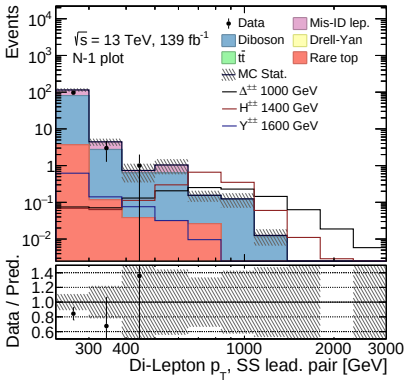

(c)

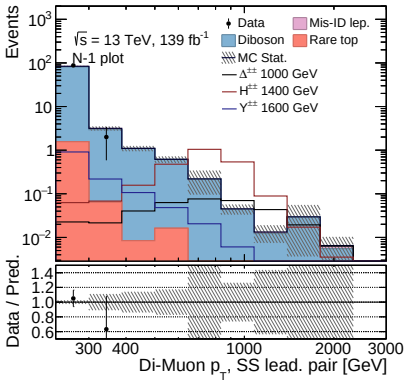

(d)

Figure A.5: SR_1P3L validation plots for the cut $p_T(l^{\pm}, l^{\pm})$ SS lead. > 300 GeV where the signals for $\Delta^{\pm\pm}$ (1000 Gev), $Y^{\pm\pm}$ (1600 GeV) and $H^{\pm\pm}$ (1400 GeV) are shown. The distribution (a) refers to the electron channel ($e^{\pm}e^{\pm}e^{\mp}$); (b) refers to the mixed channel ($e^{\pm}e^{\pm}\mu^{\mp}$); (c) refers to the mixed channel ($\mu^{\pm}\mu^{\pm}e^{\mp}$); (d) refers to the muon channel ($\mu^{\pm}\mu^{\pm}\mu^{\mp}$).

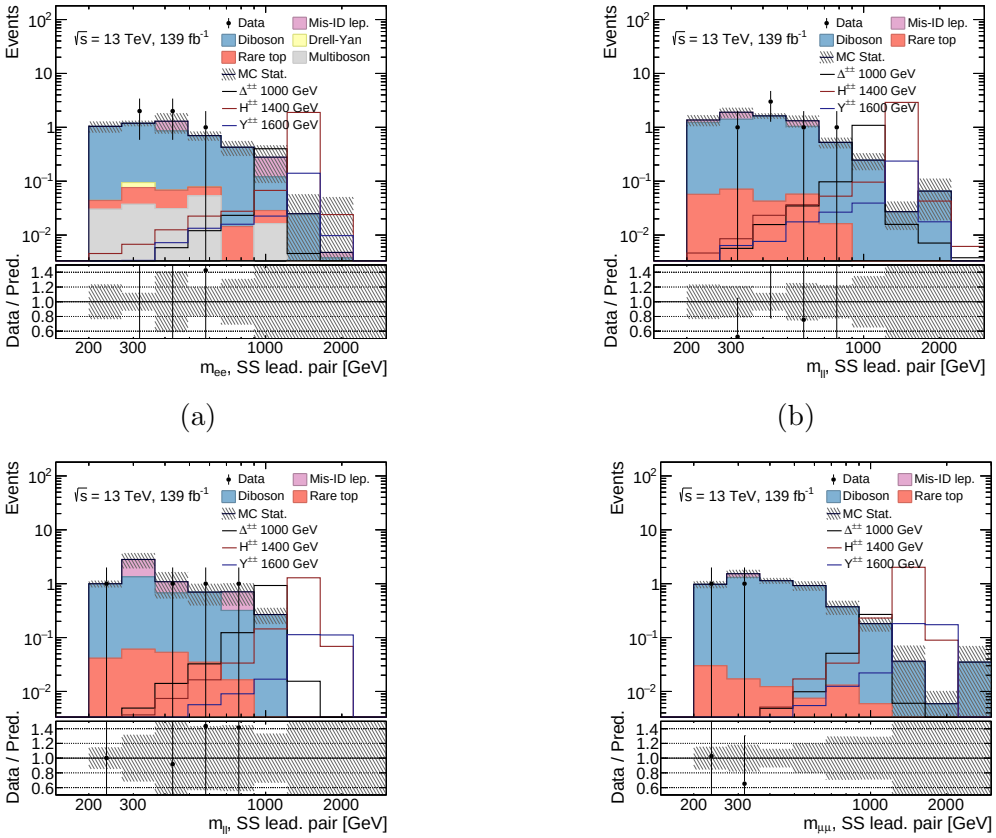

Figure A.6: SR_1P3L validation plots for the cut $\Delta m(l^{\pm}, l^{\pm})$ SS lead. > 200 GeV where the signals for $\Delta^{\pm\pm}$ (1000 Gev), $Y^{\pm\pm}$ (1600 GeV) and $H^{\pm\pm}$ (1400 GeV) are shown. The distribution (a) refers to the electron channel ($e^{\pm}e^{\pm}e^{\mp}$); (b) refers to the mixed channel ($e^{\pm}e^{\pm}\mu^{\mp}$); (c) refers to the mixed channel ($\mu^{\pm}\mu^{\pm}e^{\mp}$); (d) refers to the muon channel ($\mu^{\pm}\mu^{\pm}\mu^{\mp}$)

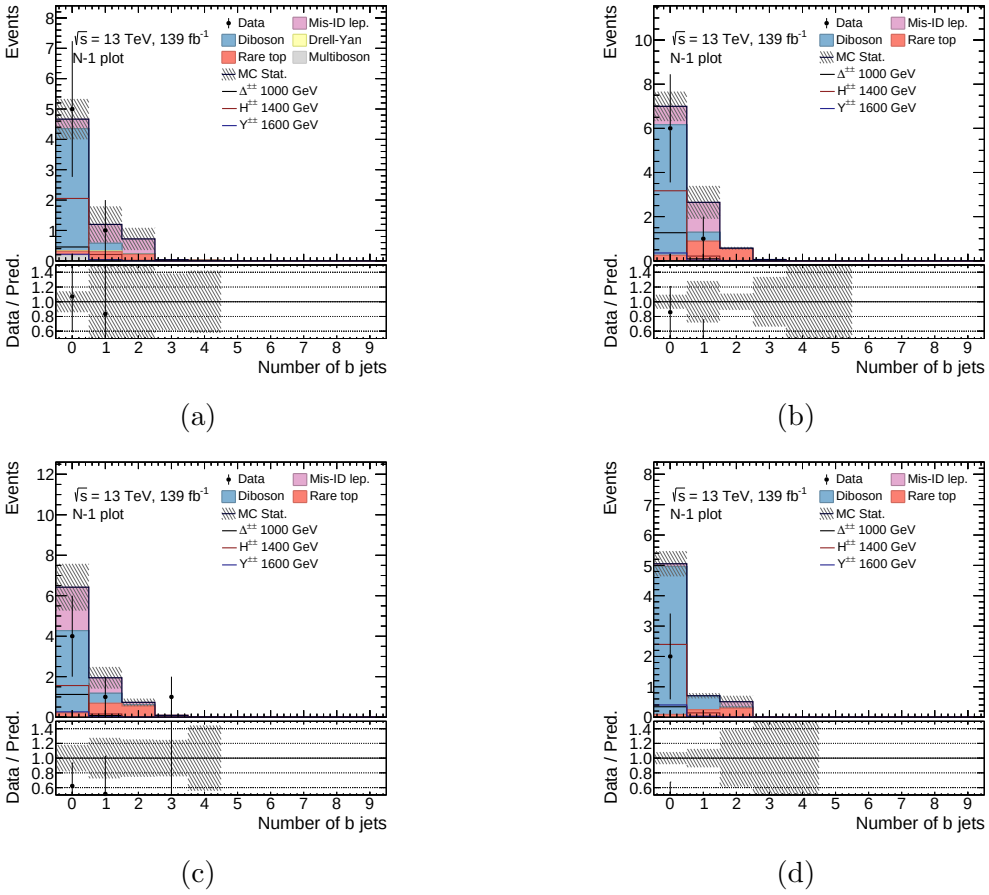

Figure A.7: SR_1P3L validation plots for the cut *number of b-jets*= 0 where the signals for $\Delta^{\pm\pm}$ (1000 Gev), $Y^{\pm\pm}$ (1600 GeV) and $H^{\pm\pm}$ (1400 GeV) are shown. The distribution (a) refers to the electron channel ($e^{\pm}e^{\pm}e^{\mp}$); (b) refers to the mixed channel ($e^{\pm}e^{\pm}\mu^{\mp}$); (c) refers to the mixed channel ($\mu^{\pm}\mu^{\pm}e^{\mp}$); (d) refers to the muon channel ($\mu^{\pm}\mu^{\pm}\mu^{\mp}$)

Four-lepton signal region

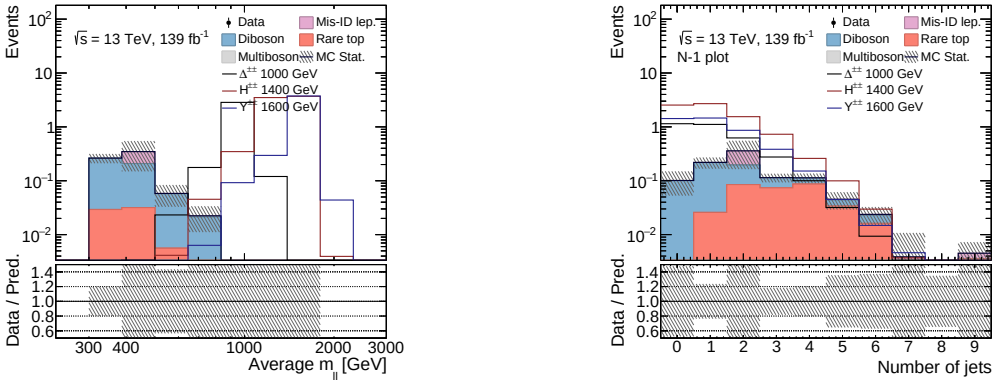

(a) (b)

Figure A.8: SR_2P4L validation plots for the cut $\bar{M} = \frac{m^{++}+m^{--}}{2} > 300$ GeV (a) and for the cut *number of b-jets*= 0 (b) where the signals for $\Delta^{\pm\pm}$ (1000 Gev), $Y^{\pm\pm}$ (1600 GeV) and $H^{\pm\pm}$ (1400 GeV) are shown for the inclusive flavour.

A.0.2 Final state leptons kinematic variables

Two-leptons signal region

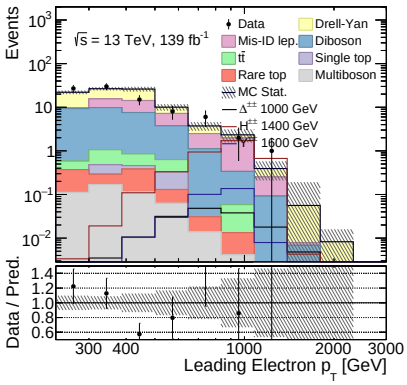

(a)

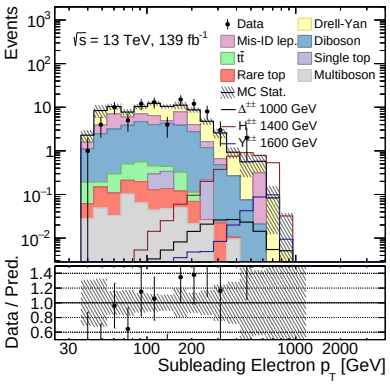

(b)

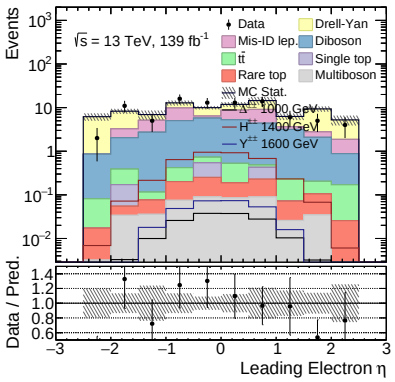

(c)

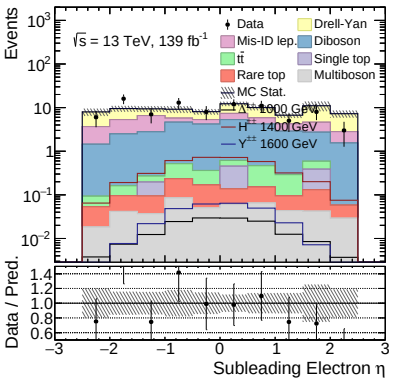

(d)

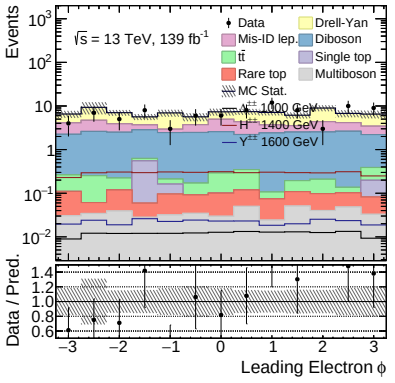

(e)

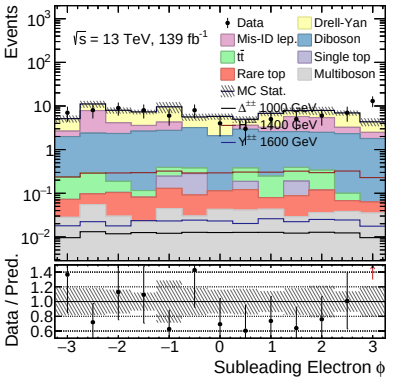

(f)

Figure A.9: SR_1P2L: p_T, η and ϕ distributions for *leading* (a)(c)(e) and *subleading* (b)(d)(f) electron.

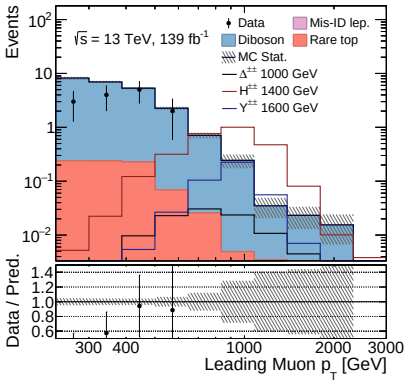

(a)

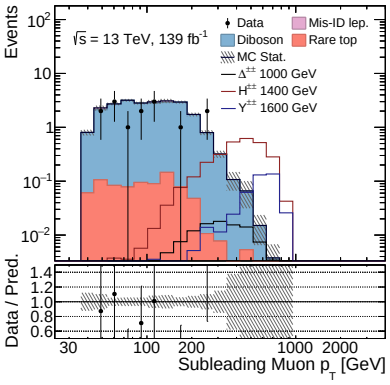

(b)

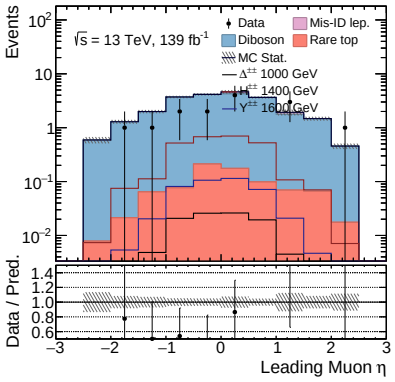

(c)

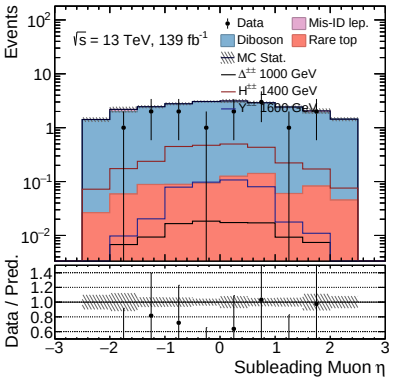

(d)

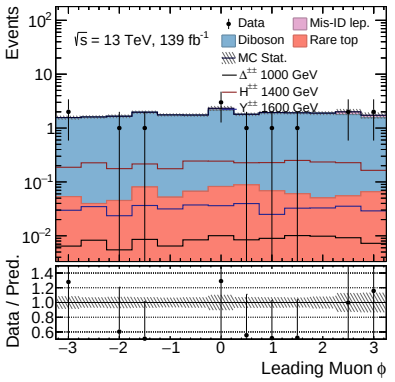

(e)

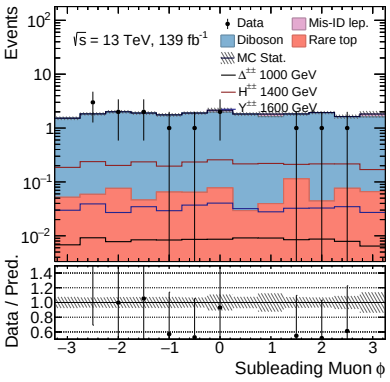

(f)

Figure A.10: SR_1P2L: p_T, η and ϕ distributions for *leading* (a)(c)(e) and *subleading* (b)(d)(f) muon.

Three-leptons signal region

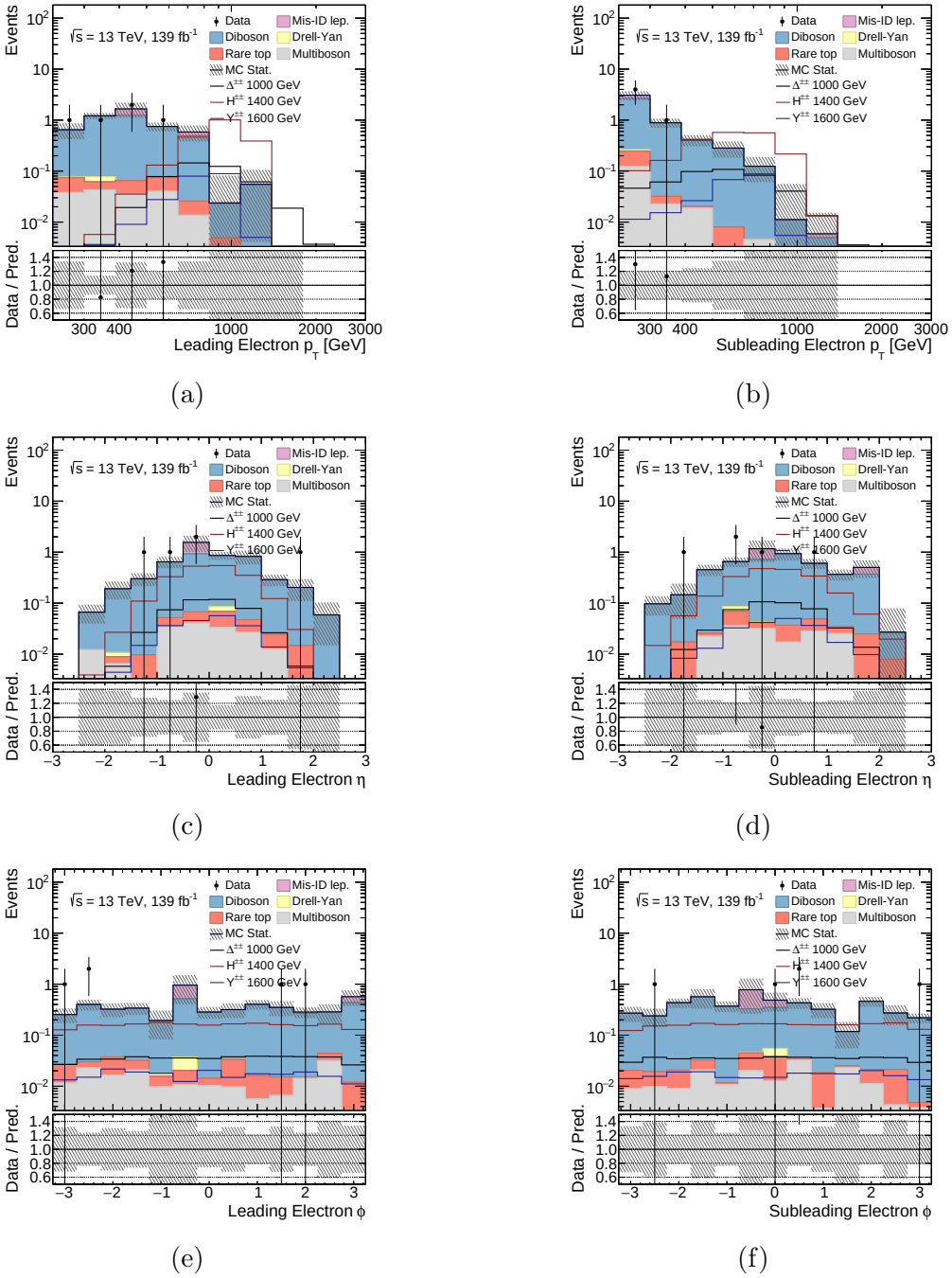

Figure A.11: SR_1P3L: p_T, η and ϕ distributions for *leading* (a), (c), (e) and *subleading* (b), (d), (f) electron.

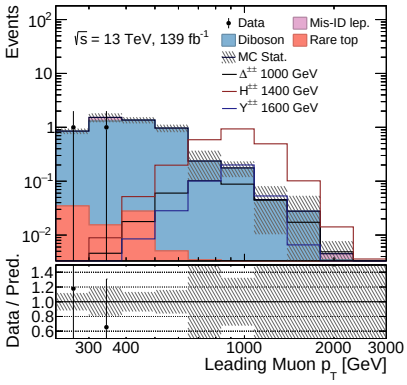

(a)

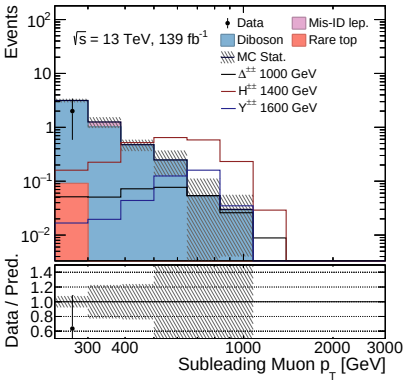

(b)

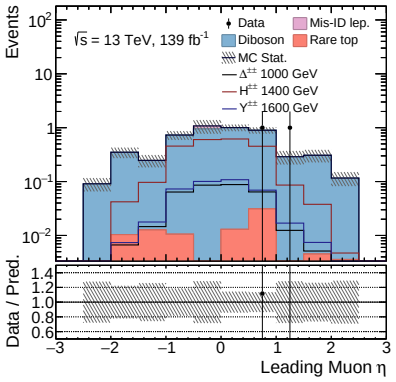

(c)

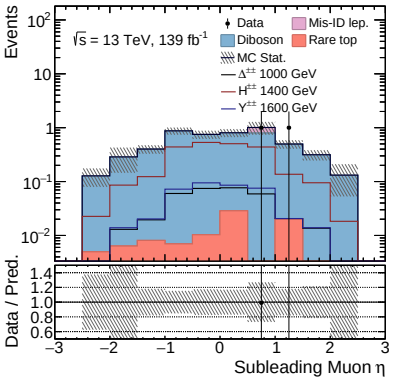

(d)

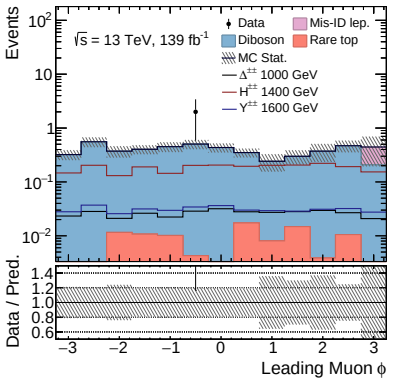

(e)

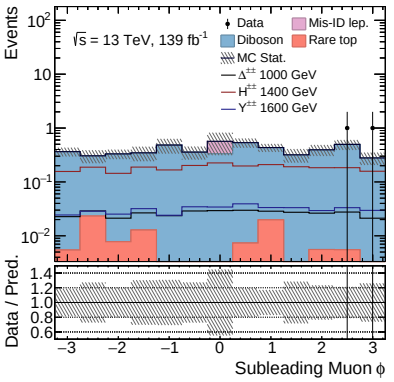

(f)

Figure A.12: SR_1P3L: p_T, η and ϕ distributions for *leading* (a), (c), (e) and *subleading* (b), (d), (f) muon.

Four-leptons signal region

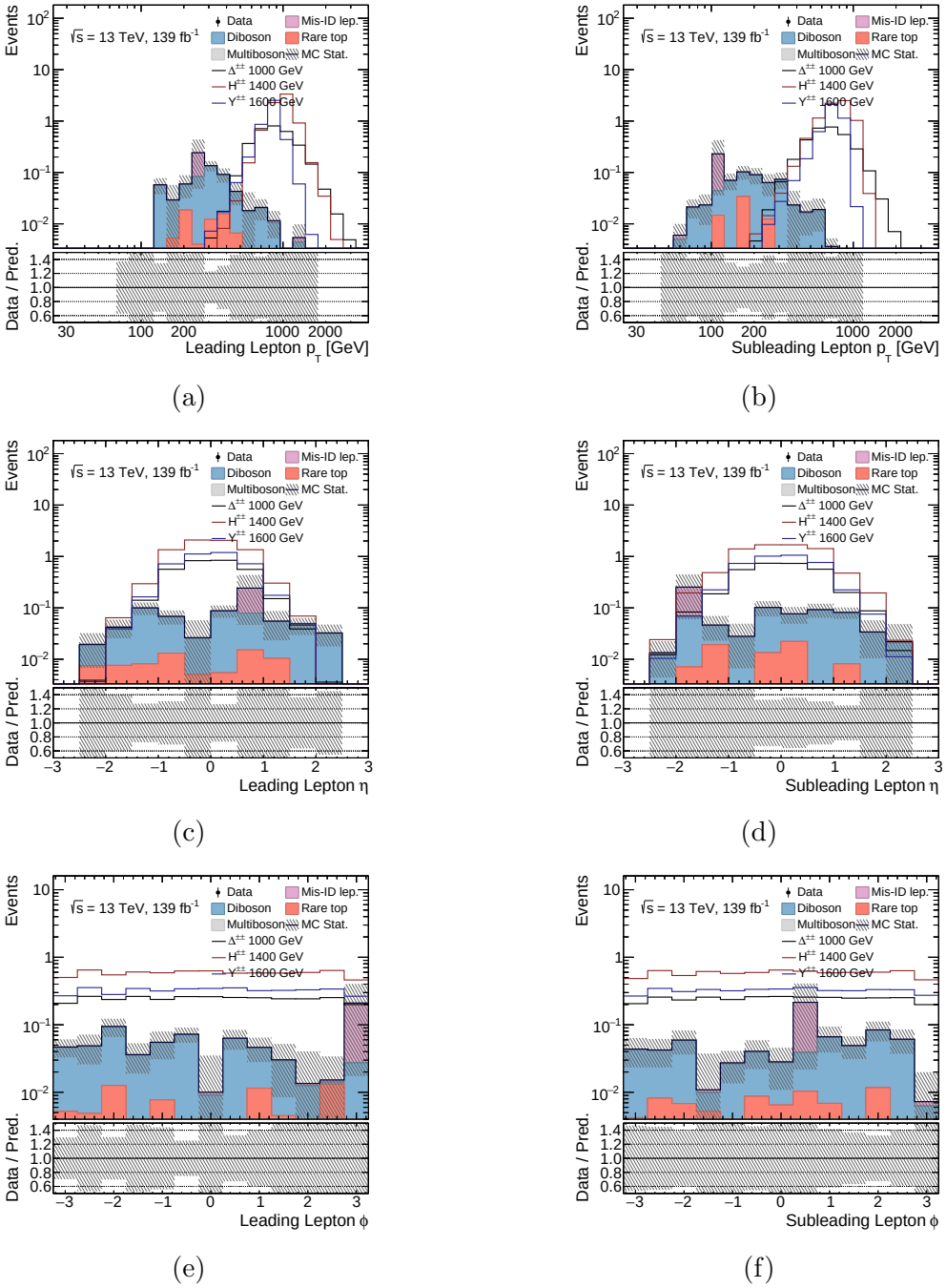

(a) (b) (c) (d) (e) (f)

Figure A.13: SR_2P4L: p_T, η and ϕ distributions for *leading* (a), (c), (e) and *subleading* (b), (d), (f) lepton.

A.0.3 Distributions of $\Delta^{\pm\pm}$, $Y^{\pm\pm}$ and $H^{\pm\pm}$ kinematic variables

Two-leptons signal region

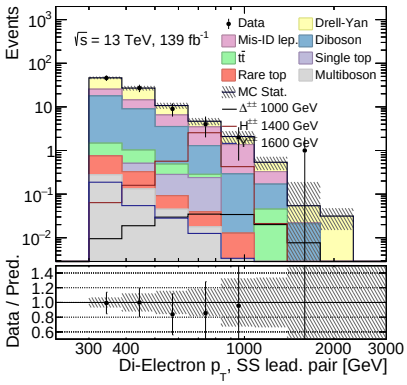

(a)

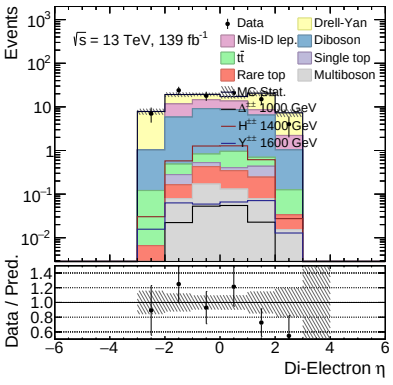

(b)

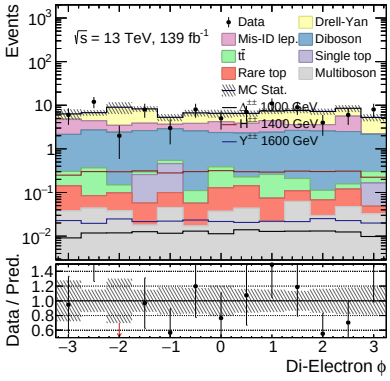

(c)

Figure A.14: SR_1P2L: p_T, η and ϕ distributions of $\Delta^{\pm\pm}$ (1000 Gev), $Y^{\pm\pm}$ (1600 GeV) and $H^{\pm\pm}$ (1400 GeV) signals for the electron channel ($e^{\pm}e^{\pm}$).

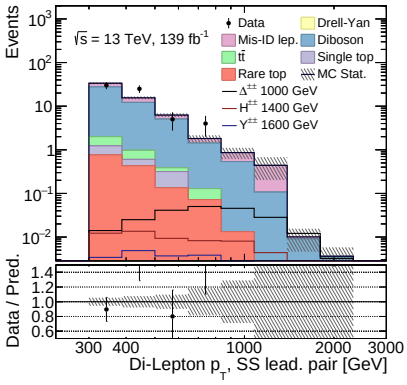

(a)

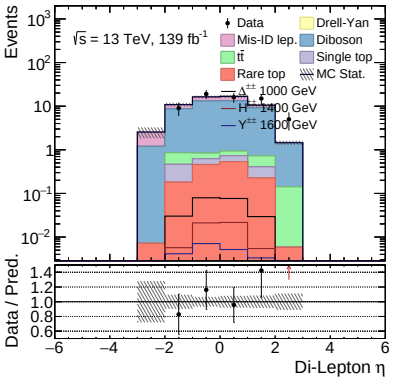

(b)

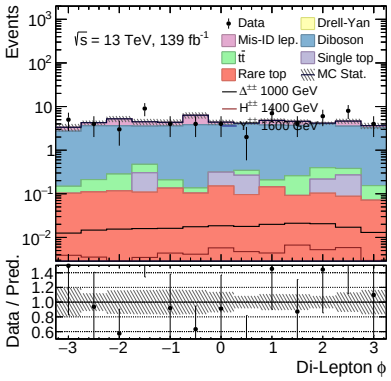

(c)

Figure A.15: SR_1P2L: p_T, η and ϕ distributions of $\Delta^{\pm\pm}$ (1000 Gev), $Y^{\pm\pm}$ (1600 GeV) and $H^{\pm\pm}$ (1400 GeV) signals for the mixed channel ($e^{\pm}\mu^{\pm}$).

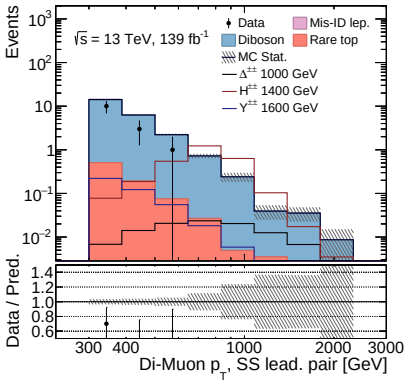

(a)

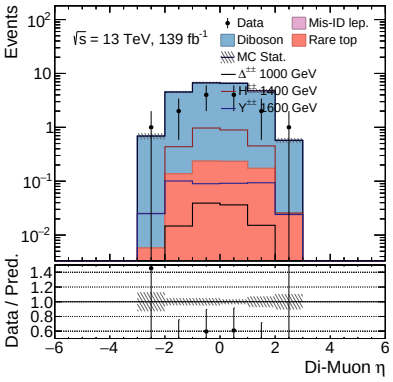

(b)

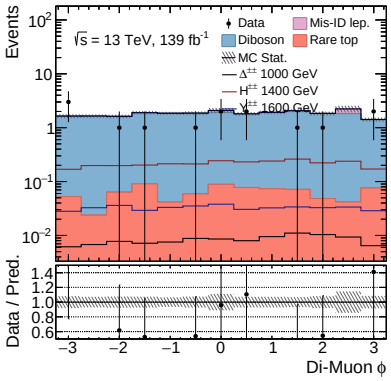

(c)

Figure A.16: SR_1P2L: p_T, η and ϕ distributions of $\Delta^{\pm\pm}$ (1000 Gev), $Y^{\pm\pm}$ (1600 GeV) and $H^{\pm\pm}$ (1400 GeV) signals for the muon channel ($\mu^{\pm}\mu^{\pm}$).

Three-leptons signal region

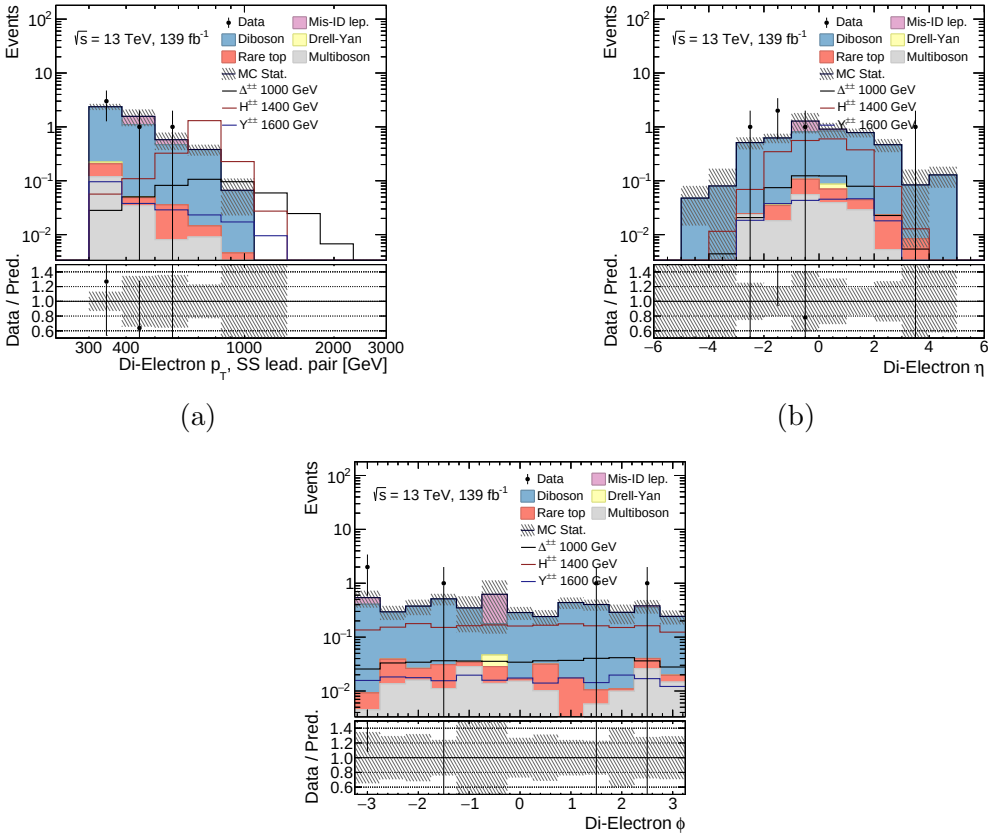

(a) (b)

(c)

Figure A.17: SR_1P3L: p_T, η and ϕ distributions of $\Delta^{\pm\pm}$ (1000 Gev), $Y^{\pm\pm}$ (1600 GeV) and $H^{\pm\pm}$ (1400 GeV) signals for the electron channel ($e^{\pm}e^{\pm}e^{\mp}$).

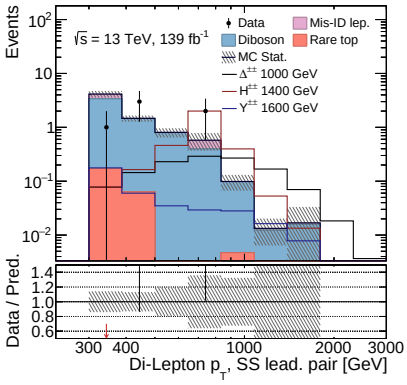

(a)

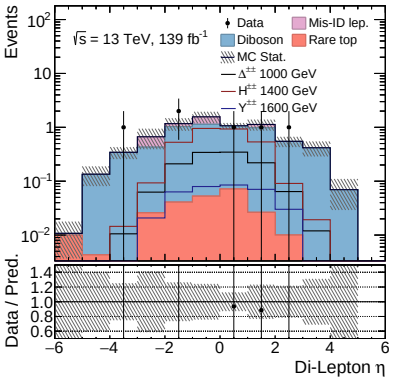

(b)

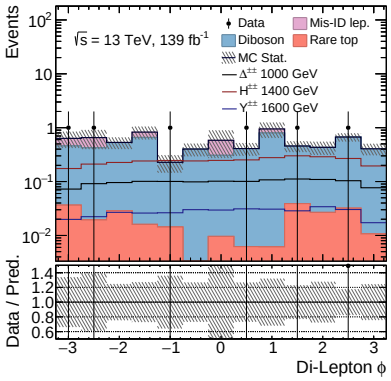

(c)

Figure A.18: SR_1P3L: p_T, η and ϕ distributions of $\Delta^{\pm\pm}$ (1000 Gev), $Y^{\pm\pm}$ (1600 GeV) and $H^{\pm\pm}$ (1400 GeV) signals for the mixed channel ($e^{\pm}e^{\pm}\mu^{\mp}$).

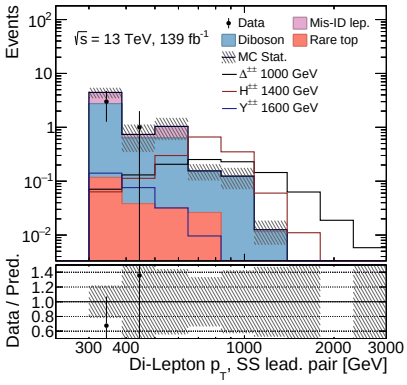

(a)

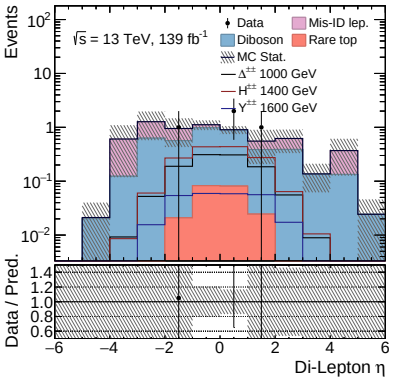

(b)

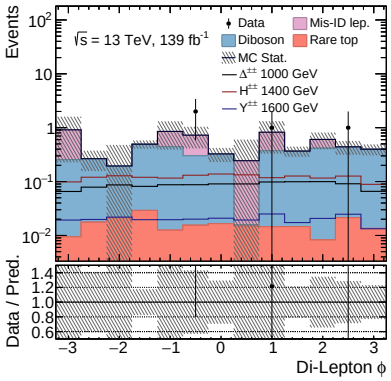

(c)

Figure A.19: SR_1P3L: p_T, η and ϕ distributionsof $\Delta^{\pm\pm}$ (1000 Gev), $Y^{\pm\pm}$ (1600 GeV) and $H^{\pm\pm}$ (1400 GeV) signals for the electron channel ($e^{\mp}\mu^{\pm}\mu^{\pm}$).

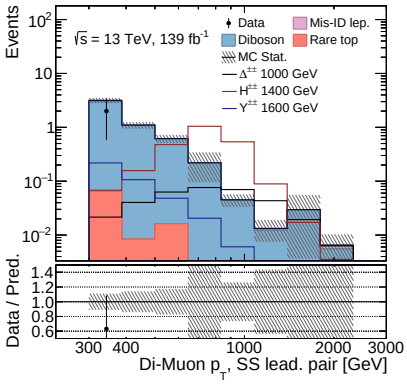

(a)

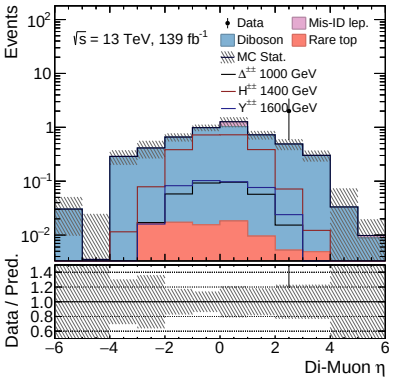

(b)

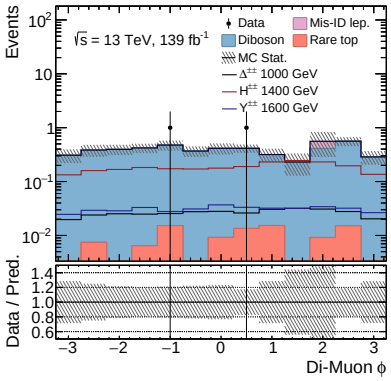

(c)

Figure A.20: SR_1P3L: p_T, η and ϕ distributions of $\Delta^{\pm\pm}$ (1000 Gev), $Y^{\pm\pm}$ (1600 GeV) and $H^{\pm\pm}$ (1400 GeV) signals for the electron channel ($\mu^{\pm}\mu^{\pm}\mu^{\mp}$).

Four-leptons signal region

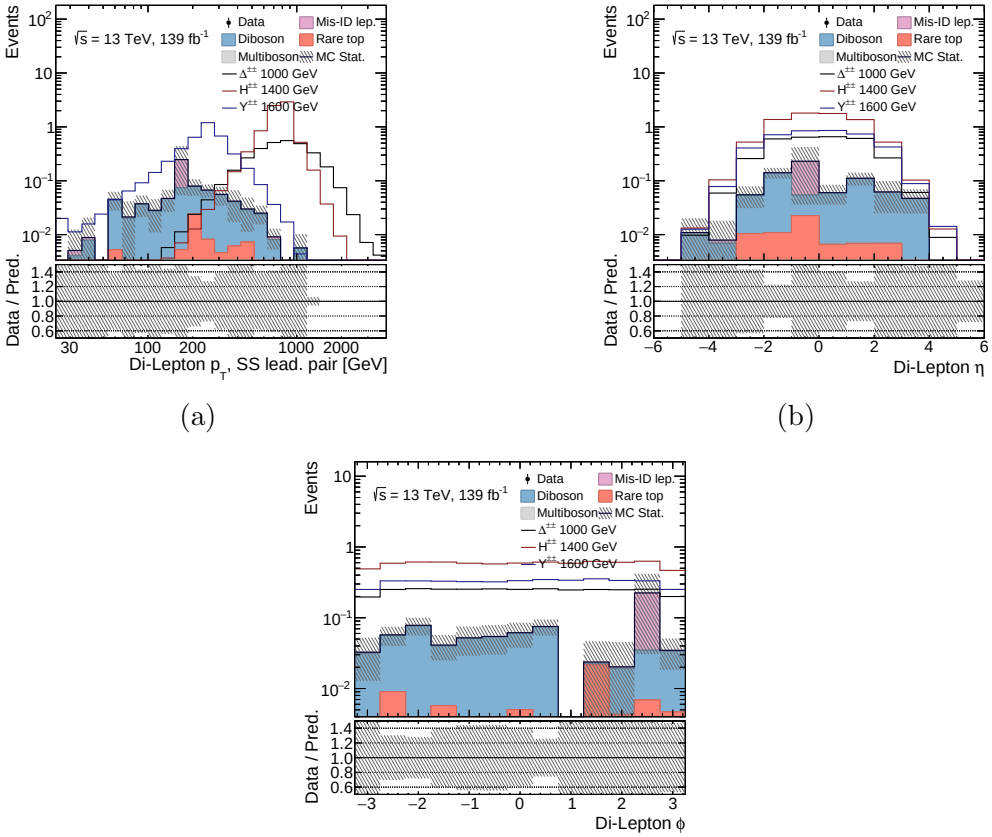

(a) (b)

(c)

Figure A.21: SR_2P4L: p_T, η and ϕ distributions of $\Delta^{\pm\pm}$ (1000 Gev), $Y^{\pm\pm}$ (1600 GeV) and $H^{\pm\pm}$ (1400 GeV) signals for the inclusive flavour.

Appendix B

Background Estimation

As already mentioned in Section 4.1 there are two types of mis-reconstruction: *fake leptons* originated from non-prompt objects, and *charge-flipped leptons* which are events where an electron is reconstructed with the wrong charge. To estimate the fakes background a data-driven approach is used, while the charge-flip background is MC based with a data-driven technique.

Fake leptons

The decays of both heavy flavour hadrons and hadrons originating from light quarks inside a jet may lead to non-prompt leptons, say there is a non-null probability that such leptons gets reconstructed as originating from the interaction point as shown in Figure B.1. Then, one calls non-prompt those real leptons faking their actual origin. For the electron case another background arises from jets produced in the IP, *mis-identified jets*. This mis-identification happens when some of the jet track information from the ID related to its electrically charged component gets lost. In this case a jet can be identified as an electron and called *fake*.
Differently from the previous backgrounds which are constrained from MC simulated sample, now due to the low probability for a jet to fake a lepton and the high statistic needed by the MC to predict these events, an alternative method is used. The choice fall on the data-driven techniques, in particular the *Fake Factor Method*.

Fake Factor Method
Following this data-driven procedure one can model the background from particle mis-identification. To do so, two regions are defined: a *control region* populated by events enriched with the considered background and a *signal region* rich of signal events. The idea is to relate the events in the control region to the background events in the signal region through an extrapolation procedure. For the events containing fake leptons a weight (called *fake factor*) is calculated using the mis-identification probability for a fake lepton to satisfy the selection requirements of

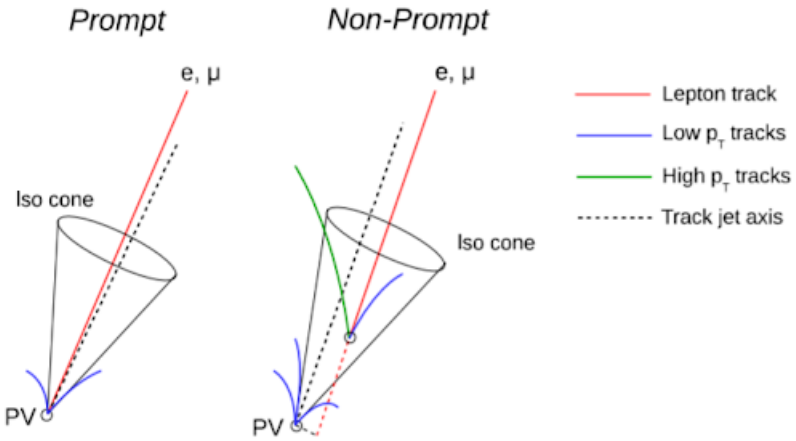

Figure B.1: Graphic representation of a prompt (left) and non-prompt (right) event. As shown, the fake lepton is the one originating from the secondary vertex inside the jet cone.

a prompt one. This probability is defined as the *fake rate*

$$f = \frac{N_{pass}}{N_{pass} + N_{fail}}, \tag{B.1}$$

where N_{pass} and N_{fail} are the number of fake leptons which satisfy and fail the identification requirements, respectively. Then, the fake factor is defined as

$$F = \frac{f}{1-f} = \frac{N_{pass}}{N_{fail}}. \tag{B.2}$$

F is measured as function of some kinematic variables and it is applied to fakes taken from data in control regions with different combinations of lepton definitions: *Tight* (T) refers to those leptons passing the identification criteria and *Loose* (L) those failing them. The fake factor formula used in the analysis is

$$N_{TT}^{\text{fakes}} = \left[\sum_{TL} F_2 + \sum_{LT} F_1 - \sum_{LL} F_1 F_2\right]_{\text{data}} - \left[\sum_{TL} F_2 + \sum_{LT} F_1 - \sum_{LL} F_1 F_2\right]_{\text{promptMC}} \tag{B.3}$$

where the sum runs over all events in regions where the leading or subleading lepton is loose and the fake factor F_i is applied to the event according to the kinematic properties of such lepton. The prompt contribution is evaluated with MC simulations and subtracted.

Charge Electrons Mis-identification

Channels involving two SS electrons (and the mixed-falour $e^{\pm}\mu^{\pm}$) are mostly affected from contamination by OS events where one of the electron charge is mis-reconstructed. Such *charge-flip* (CF) event is illustrated in Figure B.2. The electron interactions with the detector material through different physics processes can bring to CF events, these fall into two possible categories:

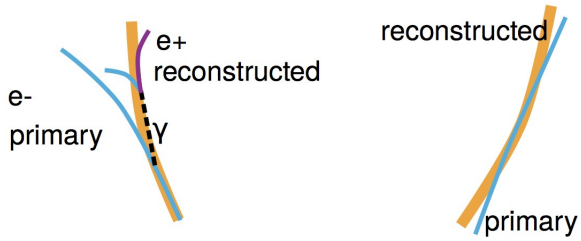

Figure B.2: Illustration of the electron charge mis-identification process due to electron interaction with the detector material.

- bremmstrahlung followed by photon conversion, *trident*: $(e^{\pm} \to e^{\pm}\gamma^{*} \to e^{\pm}e^{+}e^{-})$. The mis-reconstruction can happen according two ways: the information form the EM calorimeter can be associated to the wrong electron track, or also the bremmstrahlung process can originate an electromagnetic shower inside the ID causing a loss of information about the initial track.

- *stiff tracks* associated to a very high-p_T electrons for which charge reconstruction may be affected by measurement errors due to the fact that these electrons leave few hits for the track and momenta reconstruction.

The charge mis-identification for muons can only be of the second type since it is less likely for them to undergo bremmstrahlung. To model the muons contribution to charge mis-identification background we rely on MC simulation. To measure the charge-flip probability a (ideally clean) sample of events with $Z \to e^{+}e^{-}$ decays is constructed with a further check on the pair invariant mass. The method relies on a likelihood-fit however the actual charge-flip probabilities measurements and consequent application is analysis dependent. The information about the electron origin can be obtained by using a truth matching and, for all electrons which are classified as *charge-flips,* a *correction factor* is applied to simulation.
Given an initial number of true OS events, reconstructed events divided by charge are:

$$N^{OS} = (1 - 2\epsilon + 2\epsilon^{2})N \simeq (1 - 2\epsilon)N \tag{B.4}$$

$$N^{SS} = 2\epsilon(1-\epsilon) \simeq 2\epsilon N \tag{B.5}$$

where ϵ is the probability for one electron to be reconstructed with incorrect charge. Allowing the probabilities for the two electrons i and j to be different, the number of SS events is:

$$N^{ij}_{SS} = N^{ij}(\epsilon_i + \epsilon_j). \tag{B.6}$$

Charge mis-identification probabilities are extracted using events originating from the leptonic decay of the Z boson. If SS events in the Z peak are produced by charge-flip, N^{ij}_{SS} follows a poissonian probability:

$$f(N^{ij}_{SS};\lambda) = \frac{\lambda^{N^{ij}_{SS}e^{-\lambda}}}{N^{ij}_{SS}!} \tag{B.7}$$

where $\lambda = (\epsilon_i + \epsilon_j)N^{ij}$ is the expected number of SS pairs in bin (i,j). The probability for one electron to produce a charge-flip is expressed by:

$$P(\epsilon_i, \epsilon_j | N^{ij}_{SS}, N^{ij}) = \frac{[N^{ij}(\epsilon_i + \epsilon_j)]^{N^{ij}_{SS}} e^{-N^{ij}(\epsilon_i+\epsilon_j)}}{N^{ij}_{SS}!}. \tag{B.8}$$

The likelihood function for all the events can be expressed as:

$$\mathcal{L}(\epsilon | N_{SS}, N) = \prod_{i,j} \frac{[N^{ij}(\epsilon_i + \epsilon_j)]^{N^{ij}_{SS}} e^{-N^{ij}(\epsilon_i+\epsilon_j)}}{N^{ij}_{SS}!} \tag{B.9}$$

and the ϵ_i and ϵ_j parameter can be obtained by the minimization of $-\ln\mathcal{L}$, defined as:

$$-\ln\mathcal{L}(\epsilon | N_{SS}, N) \sim \sum_{i,j} \ln[N^{ij}(\epsilon_i + \epsilon_j)]^{N^{ij}_{SS}} e^{-N^{ij}(\epsilon_i+\epsilon_j)}. \tag{B.10}$$

In Figure B.3 the comparison between final distributions (b)(d)(f) (after the scale factors being applied) and initial distributions (a)(c)(e) is shown. Same-sign pairs are selected from the data and compared to the charge-flip prediction by applying the charge-flip scale factors to the same-sign MC events. The final distributions exhibit a better agreement compared to the one without scale factors of the same-sign $Z \to ee$ region.

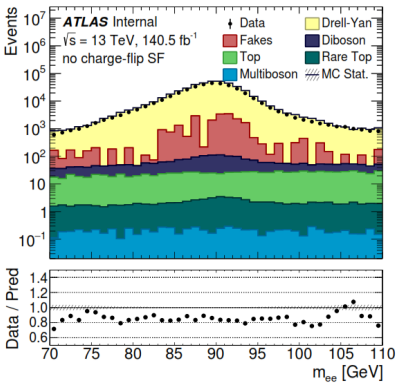

(a)

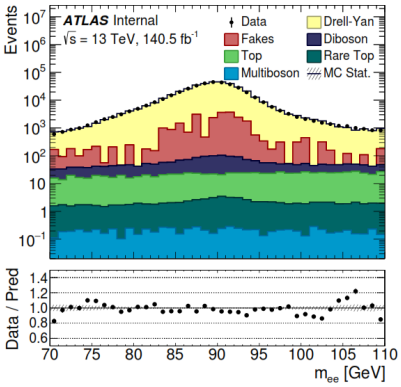

(b)

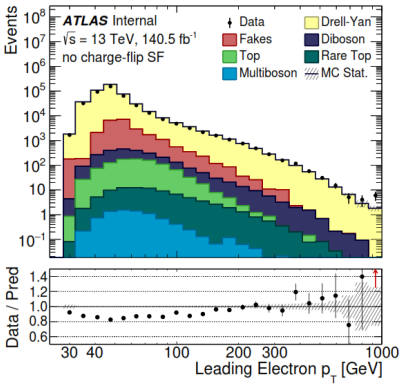

(c)

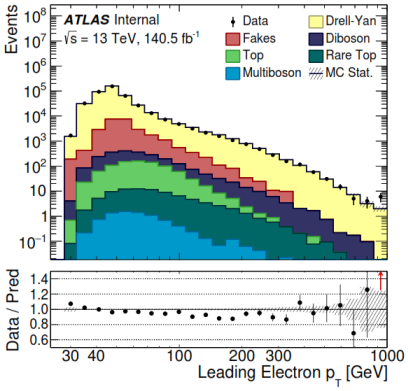

(d)

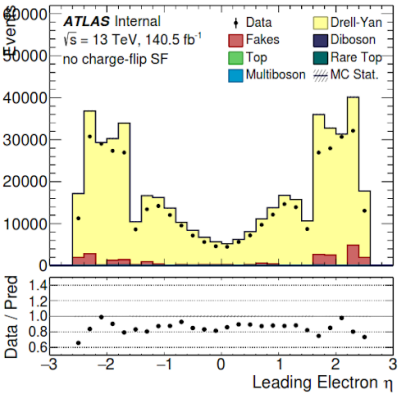

(e)

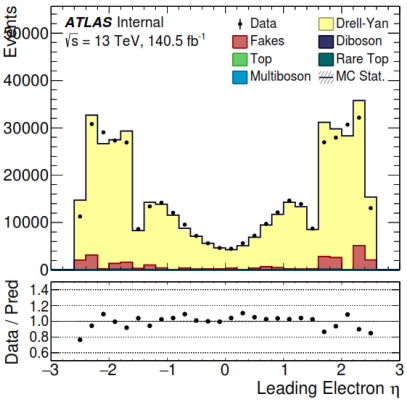

(f)

Figure B.3: On the left: initial distributions of the same-sign $Z \to ee$ region. On the right: the charge-flip closure test. Charge-flip scale factors are applied to the same-sign $Z \to ee$ region to improve the agreement. Only charge-flip systematics are applied. (a)(b) invariant mass distribution of the same-sign electron pair, (c)(d) p_T distribution of electrons, (e)(f) η distribution of electrons.

Bibliography

[1] C. Quigg, *Gauge Thories of the Strong, Weak, and Electromagnetic Interactions,* USA: Princeton University Press, 2013. ISBN:978-0-691-13548-9.

[2] M. Thomson, *Moder particle physics,* New York: Cambridge University Press, 2013. ISBN: 978-1-107-03426-6.

[3] P.A. Zyla et al. (Particle Data Group), Prog. Theor. Exp. Phys. 2020, 083C01 (2020).

[4] ATLAS Collaboration, & Collaboration, G. (2012). Aad et al. *Observation of a new particle in the search for the Standard Model Higgs boson with the ATLAS detector at the LHC*, Phys. Lett. B, 716, 1-29.

[5] Chatrchyan, S., Khachatryan, V., Sirunyan, A. M., Tumasyan, A., Adam, W., Aguilo, E., ... & Junior, W. A. (2012). *Observation of a new boson at a mass of 125 GeV with the CMS experiment at the LHC.* Physics Letters B, 716(1), 30-61.

[6] F. Halzen, A. S. Martin, *Quark & Leptons: An Introductory Course in Modern Particle Physics,* John Wiley & Sons, 2008.

[7] S. Braibant, G. Giacomelli, M. Spurio, *Particelle e interazioni fondamentali: Il mondo delle particelle,* UNITEXT, Springer Milan, 2010. ISB:9788847011618.

[8] C. S. Wu, E. Ambler, R. W. Hayward, D. D. Hoppes, R. P. Hudson, *Experimental Test of Parity Conservation in Beta Decay,* Phys. Rev. 105, 1413, 15 February 1957.

[9] S. L. Glashow, *Partial Symmetries of Weak Interactions,* In: Nucl. Phys. 22 (1961), pp.579-588.

[10] S. Weinberg, *A Model of Leptons,* In: Phys. Rev. Lett. 19 (1967), pp.1264-1266.

[11] A. Salam, *Weak and Electromagnetic Interactions,* In: Conf. Proc. C680519 (1968), pp.367-377.

[12] P. W. Higgs, *Broken Symmetries and the Masses of Gauge Bosons,* Phys. Rev. Lett. 13 (1964), pp. 508-509.

[13] F. Englert, R. Brout, *Broken Symmetry and the Mass of Gauge Vector Mesons,* In: Phys. Rev. Lett 13 (1964), pp. 321-323.

[14] A. T. Porter, R. P. Johnson, P. W. Graham, *Dark matter searches with astroparticle data,* Annual Review of Astronomy and Astrophysiscs 49 (2011), pp.155-194; arXiv:1104.2836v1 [astro-ph.HE].

[15] J. H. Christenson et al, *Evidence for the* 2π *Decay of the* K_2^0 *Meson,* Phys. Rev. Lett. 13, pp. 138-140.

[16] R. D. Peccei, *QCD, strong CP and axions,* In: J. Korean Phys. Soc. 29 (1996), S199-S208. arXiv:hep-ph/9606475.

[17] G. 't Hooft, *Naturalness, chiral symmetry, and spontaneous chiral symmetry breaking,* NATO Sci. Ser. B 59 (1980), pp. 135-157.

[18] Super-Kamiokande Collaboration, *Evidence for oscillation of atmospheric neutrinos,* Phys. Rev. Lett. 81 (1998), pp.1526-1567.

[19] ALEPH, DELPHI, L3, OPAL and SLD Collaboration, LEP Electroweak Working Group, SDL Electroweak Group and SLD Heavy Flavour Group, Phys. Rep. 427 (2006) 257, arXiv:hep-ex/0509008.

[20] P.H. Frampton, *Chiral Dilepton Model and the Flavor Question.* Phys. ReV. Lett. **69**, 2889 (1992).

[21] Gennaro Corcella, Claudio Corianó, Antonio Costantini, Paul H. Frampton, *Bilepton Signatures at the LHC,* arXiv:1707.01381v2 [hep-ph] 9 Sep 2017.

[22] E. Ramirez Barreto, Y.A. Coutinho, J. Sá Borges, *Vector- and Scalar-Bilepton Pair Production in Hadron Colliders,* arXiv:1103.1267v1 [hep-ph] 7 Mar 2011.

[23] A.A. Nepomuceno, F.L. Eccard, B. Meirose, *First results on bilepton production based on LHC collision data and predictions for run II,* Phys. Rev. D 94, 055020 (2016), arXiv:1604.07471v2 [hep-ph].

[24] The ATLAS Collaboration, *Search for doubly-charged Higgs bosons in like-sign dilepton final states at* $\sqrt{s} = 7$ TeV *with the ATLAS detector*, Eur. Phys. J. C72 (2012) 2244.

[25] Gennaro Corcella, Claudio Corianó, Antonio Costantini, Paul H. Frampton, *Exploring Scalar and Vector Bilepton at the LHC in a 331 Model,* arXiv:1806.04536v3 [hep-ph] 12 Aug 2018.

[26] The ATLAS Collaboration, *Search for doubly charged Higgs boson production in multi-lepton final states with the ATLAS detector using proton proton collisions at* $\sqrt{s} = 13\ TeV$, Eur. Phys. J. C78 (2018) 199.

[27] The CMS Collaboration, *A search for doubly-charged Higgs boson production in three and four lepton final states at* $\sqrt{s} = 13\ TeV$, CMS-PAS-HIG-16-036.

[28] N. Cavalli, *Study of heavy bosons production in 3-3-1 models with the ATLAS detector at LHC,* 2019, University of Bologna, `https://amslaurea.unibo.it/19300/`.

[29] J.C. Pati and A. Salam, *Lepton number as the fourth "color",* Phys. Rev. D 10 (1 July 1974), pp. 275-289, doi: 10.1103/PhysRevD.10.275.

[30] R.N. Mohapatra and J.C. Pati, *"Natural" left-right symmetry,* Phys. Rev. D 11, 2558-2561.

[31] G. Senjanović and R.N Mohapatra, *Exact left-right symmetry and spontaneous violation of parity,* Phys. Rev. D 12, 1502-1505.

[32] Azuelos G., Benslama K., Feland J. (2005). *Prospects for the search for a doubly charged Higgs in the left-right symmetryc model with ATLAS.* Journal of Physics G: Nuclear and Particle Physics, 32(2), 73.

[33] Ucchielli, Giulia. *Study of multi-lepton final states with the ATLAS experiment: from Standard Model to Beyond Standard Model Higgs,* University of Bologna, `http://amsdottorato.unibo.it/8594/`.

[34] CERN (The History of CERN). `https://timeline.web.cern.ch/timeline-header/89`

[35] E. Lyndon, P. Bryant, *LHC machine*, Jurnal of instrumentation 3.08 (2008): S08001.

[36] ATLAS Collaboration, *Luminosity determination in pp collisions at* $\sqrt{s} = 13TeV$ *using the ATLAS detector at the LHC*, ATLAS-CONF-2019-021, 03 June 2019.

[37] K. Schindl, *The injector chain for the LHC.* In: *LEP performance. Proceedings, 9th Workshop, Chamonix, France, January 26-29, 1999. Mar. 1999, pp.47-52.*

[38] ATLAS Collaboration, *The ATLAS experiment at the CERN Large Hadron Collider. JINST* **3** S08003 (2008)

[39] ATLAS Collaboration. *ATLAS magnet system: Technical Design Report, 1.* Technical Design Report ATLAS. Geneva: CERN, 1997. `https://cds.cern.ch/record/338080`.

[40] Stanecka, Ewa. *The ATLAS Inner Detector operation data quality and tracking performance.* arXiv:1303.3630 (2013).

[41] ATLAS Collaboration, *ATLAS muon spectrometer: Technical Design Report.* Technical Design Report ATLAS. Geneva: CERN, 1997.

[42] ATLAS Collaboration. *The Run-2 ATLAS Trigger System,* ATL-DAQ-PROC-2016-003 (2016).

[43] ATLAS Collaboration, *Electron reconstruction and identification in the ATLAS experiment using the 2015 and 2016 LHC proton-proton collision data at* $\sqrt{s} = 13$ TeV, Eur. Phys. J. C 79 (2019) 639, 12th August 2019.

[44] W. Lampl et al., *Calorimeter Clustering Algorithms: Description and Performance*, ATL-LARG-PUB-2008-002, 2008, `https://cds.cern.ch/record/1099735`.

[45] ATLAS Collaboration, *Performance of the ATLAS track reconstruction algorithms in dense environments in LHC Run 2*, Eur. Phys. J. C 77 (2017) 673, arXiv: 1704.07983 [hep-ex].

[46] ATLAS Collaboration, *Performance of the ATLAS trigger system in 2015*, Eur. Phys. J. C (2017) 77:317.

[47] ATLAS Collaboration, *Performance of electron and photon triggers in ATLAS during LHC Run 2*, In: Eur. Phys. J. C 80.arXiv:1909.00761. 1 (Sept. 2019), 47. 56 p. doi: 10.1140/epjc/s10052-019-7500-2. `https://cds.cern.ch/record/2688248`.

[48] ATLAS Collaboration, *Muon reconstruction performance of the ATLAS detector in proton-proton collision data at* $\sqrt{s} = 13$ TeV, Eur. Phys. J. C (2016) 76:292.

[49] J. Illingworth, J. Kittler, A survey of the Hough transform. Comput. Vis. Graph. Image Process. 44, 87-116 (1988). ISSN: 0734-189X. `http://www.sciencedirect.com/science/article/pii/S0734189X88800331`.

[50] Andrea Ventura and ATLAS Collaboration. *ATLAS Muon Trigger Performance.*In: (Sept. 2019). `https://cds.cern.ch/record/2688754`.

[51] The ATLAS Collaboration, *Muon identification and reconstruction efficiencies in full Run-2 dataset*, `https://atlas.web.cern.ch/Atlas/GROUPS/PHYSICS/PLOTS/MUON-2019-03/`.

[52] ATLAS Collaboration, *Measurement of the tau lepton reconstruction and identification performance in the ATLAS experiment using pp collisions at* $\sqrt{s} = 13$ TeV, ATLAS-CONF-2017-029 1st May 2017.

[53] Steven Schramm. *ATLAS Jet Reconstruction, Calibration, and Tagging of Lorentz-boosted Objects*. Tech. rep. ATL-PHYS-PROC-2017-236. Geneva: CERN, Nov. 2017. https://cds.cern.ch/record/2291608.

[54] The ATLAS Collaboration, *Jet reconstruction and performance using particle flow with the ATLAS Detector*, Eur. Phys. J. C 77 (2017) 466.

[55] Aliaksei Hrynevich. *ATLAS jet and missing energy reconstruction, calibration and performance in LHC Run-2*. Tech. rep. ATL-PHYS-PROC-2017-045. 06. Geneva: CERN, May 2017. doi: 10.1088/1748-0221/12/06/C06038. https://cds.cern.ch/record/2263777.

[56] Alconada Verzini, M. J., Alonso, F., Arduh, F. A., Dova, M. T., Hoya, J., Monticelli, F. G., & Wahlberg, H. P. (2017). Identification and rejection of pile-up jets at high pseudorapidity with the ATLAS detector. The European Physical Journal C, 77.

[57] ATLAS Software Documentation, https://atlassoftwaredocs.web.cern.ch/athena/athena-intro/.

[58] G. Cowan, E. Gross "Discovery signicance with statistical uncertainty in the background estimate", in ATLAS Statistics Forum (2008). https://www.pp.rhul.ac.uk/cowan/stat/notes/SigCalcNote.pdf

[59] Baak, M., et al. *HistFitter software framework for statistical data analysis*. Eur. Phys. J. C 75.4 (2015): 1-20.